THE UNIVERSITY *of* EDINBURGH

Deep Neural-Network Laser Absorption Spectroscopy Tomography for Combustion Diagnosis

Yalei Fu

Doctor of Philosophy

THE UNIVERSITY OF EDINBURGH

2024

Abstract

Reactive flows are present in many industrial applications, particularly in energy-generation systems, where they directly impact combustion efficiency and environmental pollution. Therefore, effective diagnosis of reactive flows is crucial, involving the monitoring of physical and chemical parameters such as flow velocity, temperature, and species concentration. Specifically, measuring temperature and species concentration can greatly reduce harmful emissions and improve fuel efficiency. Given the highly dynamic and complex nature of reactive flows, measurement techniques are required to be accurate, robust, and have a fast response.

In most industrial applications, probe-based sensing methods, such as thermocouples and gas samplers, have gained significant attention due to their simplicity in setup and measurement. However, these point-wise detection methods suffer from limited spatial and temporal resolutions. The advent of Laser Absorption Spectroscopy (LAS) provides a superior approach for diagnosing reactive flows. Due to its non-intrusive nature, fast response and robustness, LAS has become increasingly popular in industrial settings. Utilizing an emitter-receiver configuration, LAS measures the Line-of-Sight (LoS) laser intensity, which is partially absorbed by the target gas, and infers temperature and species concentration from it. This technique exhibits a temporal resolution of Kilo Hertz and above, benefiting from the quick scanning ability of tunable diode lasers for specific absorption spectra. Despite the above advantages, achieving rapid and accurate measurements remains challenging due to the time-consuming laser signal post-processing. Therefore, accelerating this process is essential.

In addition, LAS can produce spatially resolved images of gas properties when combined with tomography. This is achieved by employing multiple LoS measurements from different projection angles, known as LAS tomography. However, physical constraints of optical access in industrial combustors often result in insufficient laser beams for LAS tomography, leading to rank deficiency in tomographic inverse problems and thus inaccurate diagnostic results. Recent advancements in deep learning techniques demonstrate great potential for addressing these complex tasks.

Previous studies have shown that applying deep learning techniques to LAS and LAS tomography can enhance both the measurement speed and accuracy. Therefore, the objective of this thesis is to design applicable and effective deep learning algorithms for LAS signal post-processing and tomography in reactive flow diagnosis.

In this thesis, a novel deep learning-based hybrid neural network model has been developed for signal post-processing to predict path-average temperature of a Gas Turbine Engine (GTE). This model integrates Wavelength Modulation Spectroscopy (WMS) with fundamental physical absorption principles. By effectively extracting both temporal and spatial features from the spectral lineshape, the model provides reliable temperature predictions and ensures high industrial applicability.

For LAS tomography, two training sets are established to simulate the reactive flows of an annular combustor with ten injectors using customized multiple Gaussian profiles and a modeled circular burner simulated by the Fire Dynamics Simulator (FDS), respectively, rather than the typical Gaussian-shaped phantoms. Based on the comprehensive training sets, a Convolutional Neural Network (CNN)-based algorithm has been designed to reconstruct temperature distributions. This newly introduced method has been validated through numerical simulations, demonstrating good accuracy and sensitivity in monitoring the dynamic combustion process.

Although the simulation can mimic the dynamics of reactive flows to some extent, the reconstruction results may be suboptimal due to unpredictable discrepancies between real-world data and simulations. To address this challenge, this thesis proposes an innovative untrained neural network for LAS tomography called the Model-Informed Double Image Prior (MI-DIP). For the first time, this network introduces a dual-path architecture for dataset-free, joint reconstruction of two-dimensional temperature and species concentration. The developed network closely imitates the problem formulation of LAS tomography and regularizes the inverse problem using its physical model and inherent priors, thereby stabilizing the image reconstruction process. This approach has been validated through both numerical simulations and lab-scale experiments, demonstrating its ability to reconstruct the temperature and water vapor concentration profiles of the flames. The results highlight improved imaging accuracy and enhanced resistance to noise, showcasing the potential of the MI-DIP to provide reliable diagnostics in complex, dynamic environments.

Lay Summary

Effective monitoring of the combustion process is crucial because it significantly impacts combustion efficiency and can contribute to greenhouse gas emissions. Accurate detection of emission gas parameters, such as temperature and species concentration, is essential for evaluating combustion efficiency and gas emissions. Due to the dynamic and complex nature of reactive flows, monitoring these gas parameters necessitates measurement techniques that are accurate, robust, and fast-responding.

Traditional probe-based sensing methods, such as thermocouples and gas samplers, are popular due to their simplicity. However, these methods only provide point-specific data, which means they are not capable of capturing detailed information about the combustion dynamics over space and time. Fortunately, Laser Absorption Spectroscopy (LAS) offers a better solution. LAS is non-contact, quick, and reliable, making it increasingly popular for industrial applications. Using a setup with a laser source and a detector, LAS measures how much light is absorbed by the target gas along a straight path and infers temperature and gas concentration.

However, achieving rapid and accurate measurements with LAS can be challenging because the post-processing of laser signals to obtain gas property parameters is time-consuming. An effective algorithm for accelerating this post-processing is essential. Additionally, LAS can create high-resolution images of gas properties by integrating tomography techniques. This method, known as LAS tomography, involves multiple measurements from different projection angles. However, the physical limitations of optical access in industrial combustors often result in insufficient laser beams, leading to inaccuracies in the tomographic images.

Recent advances in deep learning offer promising solutions to these challenges. Previous studies have shown that deep learning can greatly improve the speed and accuracy of LAS and tomography. This thesis aims to design effective deep learning algorithms for both signal post-processing and imaging tasks in reactive flow diagnosis.

Acknowledgements

Time flies indeed. Suddenly, it is nearly the end of my PhD journey. Throughout this remarkable endeavor, I have been so lucky to meet a group of kind, friendly, and supportive people. They gave me invaluable support and energy, helping me navigate the challenges in both research and life.

Firstly, I wish to express my deepest gratitude to my supervisor Dr. Chang Liu. His dedication, expertise, rigorous academic spirit and kindness have shaped my academic and research trajectory. Dr. Liu has been more than just a guide in my research. He has inspired me and profoundly influenced my attitude toward life and career development.

Secondly, I would like to express my heartfelt thanks to Professor Hugh McCann, who has been a guiding light for my research endeavors. His support, thoughtful gestures such as sending Christmas cards, and concern during challenging times have been invaluable. Additionally, I also want to send my special thanks to Dr. Yunjie Yang and Prof. Manuchehr Soleimani for their time and effort in reviewing my thesis and attending my viva. Their insightful feedback has been crucial in refining my work and enhancing its quality.

During my PhD study, I am very lucky to join the LITECS project and collaborate with outstanding researchers from all over the world. I feel honored to work with Dr. Michael Lengden, Dr. Ian Armstrong, Stuart Clark and Andrew Gough from the University of Strathclyde, as well as Ihab Aham from the University of Sheffield. I would like to extend special thanks to Dr. Abhishek Upadhyay from the University of Strathclyde and Prof. Krikor Ozanyan from the University of Manchester for providing me with numerous creative ideas and invaluable feedback for my research. This project has greatly enhanced my skills in team collaboration, presentation, and problem-solving. Additionally, it has broadened my perspective on global research practices and enriched my academic experience.

I also would like to express my deepest gratitude to my excellent colleagues, Dr. Godwin Enemali, Dr. Yuan Chen, Dr. Rui Zhang, Dr. Jiangnan Xia, Minqiu Zhou and Yikai Xia for their encouragement and help. The joyful moments, lively discussions in AGB 1.08 are the cherished memories that will always remain in my mind. In addition,

my thanks also go to my friends in the Agile Tomography group, including Dr. Zhou Chen, Dr. Zhe Liu, Hao Yu, Wei Han, Dr. Delin Hu, Dr. Zhixi Zhang and Huazhi Dong, for their company and happiness fulfilled in my life. Furthermore, I want to say thanks to my dearest friend Androniki K. Papathanasi. Her mental support and constant encouragement have enpowered me whenever I faced obstacles. Thank you!

Lastly, but most importantly, I want to send my love and heart to my parents Bo Fu and Guoying Yang, my lovely grandpa Changchun Fu, my sweet grandma Xianzhen Meng and my cute brother Xueqi Fu. It is they that make me being loved and supported all the time, giving me power and energy. Words cannot express my gratitude and thanks to them.

Declaration

I declare that this thesis was composed by myself, that the work contained herein is my own except where explicitly stated otherwise in the text, and that this work has not been submitted for any other degree or professional qualification except as specified.

Yalei Fu

Publication list

Journal Papers

1. **Y. Fu**, R. Zhang, J. Xia, A. Gough, S. Clark, A. Upadhyay, G. Enemali, I. Armstrong, I. Ahmed, M. Pourkashanian, P. Wright, K. Ozanyan, M. Lengden, W. Johnstone, N. Polydorides, H. McCann, C. Liu, "Hybrid model-driven spectroscopic network for rapid retrieval of turbine exhaust temperature," *IEEE Transactions on Instrumentation and Measurement*, doi: 10.1109/TIM.2023.3328086.
2. **Y. Fu**, Z. Liu, R. Zhang, J. Xia, X. Liu, and C. Liu, "Model-informed double image prior for flow-field imaging using chemical species tomography," (submitted to *IEEE Transactions on Neural Networks and Learning Systems*).
3. J. Xia, G. Enemali, R. Zhang, **Y. Fu**, H. McCann, B. Zhou, and C. Liu, "FPGA-Accelerated Distributed Sensing System for Real-Time Industrial Laser Absorption Spectroscopy Tomography at Kilo-Hertz," *IEEE Transactions on Industrial Informatics*, doi: 10.1109/TII.2023.3292971.
4. J. Si, G. Fu, X. Liu, Y. Cheng, R. Zhang, J. Xia, **Y. Fu**, G. Enemali, and C. Liu, "A Spatially Progressive Neural Network for Locally/Globally Prioritized TDLAS Tomography," *IEEE Transactions on Industrial Informatics*, doi: 10.1109/TII.2023.3240733.
5. R. Zhang, J. Xia, I. Ahmed, A. Gough, I. Armstrong, A. Upadhyay, **Y. Fu**, G. Enemali, M. Lengden, W. Johnstone, P. Wright, K. Ozanyan, M Pourkashanian, H. McCann, and C. Liu, “A fast sensor for non-intrusive measurement of concentration and temperature in turbine exhaust,” *Sensors and Actuators B: Chemical*, doi: 10.1016/j.snb.2023.134500.

Conference Papers

1. **Y. Fu**, R. Zhang, G. Enemali, A. Upadhyay, M. Lengden, C. Liu, "Convolutional neural network aided chemical species tomography for dynamic temperature imaging," *2022 IEEE International Instrumentation and Measurement Technology Conference (I2MTC)*, Ottawa, Canada, 2022.
2. **Y. Fu**, C. Liu, R. Zhang, G. Enemali, J. Xia, H. McCann, A. Upadhyay, I. Armstrong, A. Gough, M. Lengden, and W. Johnsone, " Deep learning-aided wavelength modulation spectroscopy for rapid temperature measurement,"*7th Field Laser Applications in Industry and Research (FLAIR)*, Aix-les-Bains, France, 2022.
3. R. Yi, **Y. Fu**, C. Liu, "Gaussian Mixture Model-Based Temperature Modelling for Data-Driven Laser Absorption Spectroscopy Tomography," *2024 IEEE International Instrumentation and Measurement Technology Conference (I2MTC)*, Glasgow, UK, 2024.
4. R. Zhang, G. Enemali, **Y. Fu**, H. McCann, I. Armstrong, A. Upadhyay, A. Gough, M. Lengden, and W. Johnstone, M. Pourkashanian, C. Liu, " Non-intrusive optical sensor design for chemical species tomography with millimetre-level spatial resolution,"*7th Field Laser Applications in Industry and Research (FLAIR)*, Aix-les-Bains, France, 2022.

Contents

Figures and Tables

Figures

Tables

Nomenclature

Acronyms

1D-CNN	One-Dimensional Convolutional Neural Network
2D	Two-Dimensional
3D	Three-Dimensional
ACE	Absolute Curve Error
AD-CNN	Attentioned Dual-branch Convolutional Neural Network
AE	Autoencoder
AOGAM	Adaptively Optimized Gas Analysis Model
APU	Auxiliary Power Unit
ART	Algebraic Reconstruction Technique
BN	Batch Normalization
CARS	Coherent Anti-stokes Raman Spectrocopy
CC	Correlation Coefficient
CE	Curve Error
CF-WMS	Calibration-Free WMS
CFD	Computational Fluid Dynamics
CIC	Cascaded Integrator-Comb
CNN	Convolutional Neural Network
CO	Carbon Oxides
DAQ	Data Acquisition
DAS	Direct Absorption Spectroscopy
DIP	Deep Image Prior
DNN	Deep Neural Network
DW-CNN	Depth-Wise CNN
EGT	Exhaust Gas Temperature
ERM	Empirical Risk Minimization
FC	Fully-Connected
FDM	Frequency Division Multiplexing
FDS	Fire Dynamics Simulator

FNN	Feedforward Neural Network
FSR	Free Spectral Range
FTIR	Fourier-Transform Infrared Spectroscopy
FWHM	Full Width at Half Maximum
GMM	Gaussian Mixture Model
GTE	Gas Turbine Engine
H_2O	Water Vapor
IE	Image Error
IT	Infrared Thermography
LAS	Laser Absorption Spectrocopy
LeakyReLU	Leaky Rectified Linear Unit
LIF	Laser Induced Fluorescence
LoS	Line-of-Sight
LPF	Low-Pass Filter
MHSA	Multi-Head Self-Attention
MI-DIP	Model-Informed Double Image Prior
MLP	Multi-Layer Perceptron
MSE	Mean Square Error
NIST	National Institute of Standards and Technology
NO	Nitrogen Oxides
PINN	Physics-Informed Neural Network
PV	Peak Value
RCE	Relative Curve Error
RMSE	Root Mean Squared Error
RNN	Recurrent Neural Network
RoI	Region of Interest
RoS	Region of Sensing
SAM	Spatial-Attentioned Mechanism
SE	Standard Error
SNR	Signal-to-Noise Ratio
SO	Sulphur Oxides
SRM	Structual Risk Minimization

SRS	Spontanous Raman Spectroscopy
SSIM	Structural Similarity index
STD	Standard Deviation
TC	ThermoCouple
TDL	Tunable Diode Laser
UNN	Untrained Neural Network
VDF	Velocity-Distribution Function
WMS	Wavelength Modulation Spectroscopy

Chapter 1

Introduction

1.1 Background and Motivation

The combustion process involves a series of exothermic chemical reactions with extensive energy releases [1]. The outcome of the combustion process, in terms of its energy generation and power conversion, has contributed to various industrial applications, such as electricity generation, the operation of gas turbines. However, as fossil fuels are still the vast majority of the combustion resources, their pollutant emissions, mainly in the form of Nitrogen Oxides (NO_x), Carbon Monoxide (CO) and Sulphur Oxide (SO_x), are of great concern due to their detrimental impact on the environment and human health [1; 2]. To reduce harmful emissions and meantime maintain a stable and safe combustion power system, it is widely suggested to either optimize the design of the efficient, low-emission combustion process or spread the usage of cleaner fuel resources. Consequently, the accurate and efficient diagnosis of the reactive flow during the combustion process is highly demanded. Specifically, temperature and species concentration are two important combustion parameters required to be measured. Both can indicate the combustion efficiency and influence the generation of incomplete combustion products. However, it is challenging to develop a robust, accurate, and fast-response measurement system in *in situ* environment due to the dynamic combustion process and the unpredictable noise.

Most conventional gas sensors are intrusive, where their probes will be inserted into the *in situ* environment to obtain the measurements. For example, the ThermoCouple (TC) is required to position in the combustor for collecting the point-wised temperature. Similarly, other gas analytical techniques, such as Fourier-Transform Infrared Spectroscopy (FTIR) [3] and gas chromatography [4] will measure the species concentration from their extractive gas sampling probes. These techniques have been widely used due to their easy implementation and reasonable accuracy. Nonetheless, they have notable limitations. Firstly, their intrusive nature could disrupt the original

condition, thus inducing uncertainties. Secondly, the slow response in time would reduce temporal resolution, hindering the rapid capture of reactive flow dynamics. Lastly, their point-wise measurement restricts their application on Two-Dimensional (2D) gas parameter retrieval.

Recently, optical sensing techniques have been widely adopted in combustion diagnosis because of their non-intrusive and fast-response nature [5; 6]. Depending on the light sources, it can be further categorized into the passive optical sensing and the active optical sensing. Typically, passive optical sensing relies on capturing the naturally occurring light or radiation emitted/reflected by the objects themselves for detection and diagnosis. Infrared Thermography (IT) is a typical passive optical sensing method [7]. It captures the thermal radiation emitted by objects to reconstruct the 'thermal' image. However, this type of technique attempts to be strongly influenced by the surrounding environment and external light sources and requires the black body for calibration [8], thus their measurement accuracy is sensitive and unstable.

In contrast, active optical sensing requires external light sources, offering greater control and precision under various measurement conditions. Representative techniques in this category mainly include Laser Induced Fluorescence (LIF) [9; 10], Coherent Anti-stokes Raman Spectrocopy (CARS) [11; 12] and Spontaneous Raman Spectroscopy (SRS) [13]. However, most of the aforementioned techniques require complicated, high-power laser sources and precise alignment of the laser beams with an elaborate optical layout. Consequently, they are less suitable for *in situ* and real-time monitoring of harsh industrial environments, which are often characterized by unpredictable mechanical vibrations and dust contamination.

Another widely recognized optical technique is Laser Absorption Spectroscopy (LAS), which has developed as an accurate, robust, and fast-response optical modality for combustion diagnosis [14; 15]. Specifically, LAS is implemented by measuring the absorbance of the laser intensity when the partially-absorbed laser signals are detected by the receiver after passing through the targeted medium. These absorption characteristics are valuable for both qualitative and quantitative gas analysis and identification [16], enabling the reconstruction of multiple combustion parameters, such as species concentrations, temperature, pressure, etc. Since the LAS technique focuses on the spectral absorbance of targeted gas species, fluctuations in laser intensity caused by mechanical vibrations and dust contamination have a negligible effect on the measurements, which enhances the application of LAS in harsh industrial environments. Compared to the above-mentioned high-power and expensive laser

techniques, LAS utilizes compact and cost-effective laser beams that are compatible with optical fiber transmission. This compatibility facilitates a simpler configuration system consisting of laser signal generation and acquisition, thus enabling real-time diagnosis of the dynamic combustion process. The implementation of LAS typically employs an emitter-receiver configuration, where a laser beam is emitted along a Line-of-Sight (LoS) through the medium of interest. This approach, known as LoS-LAS, primarily measures the average gas parameters along the optical path, making it well-suited for environments characterized by uniform combustion. However, the dynamics and the complexity of the reactive flow fields, which are inherently non-uniform, pose great challenges for capturing spatial characteristics of the combustion process using a single LoS-LAS configuration. Consequently, to accurately assess the gas properties, multiple LoS-LAS measurements from different projection angles are required. These measurements facilitate the reconstruction of cross-sectional distributions within non-uniform and complex combustion fields, referred to as LAS tomography. After combining with advanced image reconstruction algorithms, LAS tomography has demonstrated feasibility and robustness in various industrial applications, e.g., the exhaust of the Gas Turbine Engine (GTE) [17; 18; 19].

Although LAS and LAS tomography offer advantages over other optical sensing techniques for reactive flow diagnosis, several challenges remain when deploying them in real industrial settings. For instance, the signal post-processing of single LoS-LAS can be time-consuming due to suboptimal calculation methods and limited computational resources. Rapid and precise determination of gas properties is crucial in kinetic industrial scenarios for effective combustion detection. In the context of LAS tomography, numerous emitting and receiving sensors need to be deployed around the targeted region to achieve simultaneous and spatially-resolved retrieval of gas parameters. Although fiber optics allow for relatively small and discontinuous optical windows, the physical dimensions of the sensor system and the available space within the combustion zone limit the total number of laser beams that can be used for detection. This results in insufficient sampling, creating an under-determined inverse problem when reconstructing 2D gas parameters.

Various techniques and algorithms have been developed to mitigate the effects of the inverse problem in LAS tomography. These can be categorized into three main groups: algebraic techniques based on linear back projection, such as the Landweber algorithm [20] and Algebraic Reconstruction Technique (ART) [21]; regularization methods, e.g., Tikhonov regularization [22]; and dimension reduction techniques, such as

surrogate function methods [23]. These algorithms either impose empirically determined penalizations, including non-negativity and smoothness of the reconstructions or use iterative computations to reduce artifacts caused by the inverse problem in LAS tomography. However, most implicit penalization priors fail to capture the physical features of reactive flows, and the complex mathematical operations involved result in high computational costs. These issues hinder the deployment of LAS tomography for real-time gas image reconstruction and robust performance.

The accelerated development of hardware in the last decade has spurred the rapid growth of data-driven methods. These methods leverage large volumes of data within hierarchical networks, enabling models to learn and discern underlying patterns for implementation effectively. Various neural network architectures, such as the Feed-forward Neural Network (FNN) [24], the Convolutional Neural Network (CNN) [25], and the Recurrent Neural Network (RNN) [26], have been developed for various applications and tasks. However, these methods heavily rely on well-labeled datasets, which are impractical in dynamic industrial conditions characterized by unpredictable signal distortion and noise contamination. Additionally, these algorithms do not yield physical information in the reconstruction results, limiting their capability to enhance spatial resolution. Consequently, there is an increasing demand for rapid, robust, and accurate signal processing and gas property reconstruction techniques for LoS-LAS and LAS tomography in industrial combustion diagnostics.

1.2 Aims and Objectives

The primary aim of this PhD project is to address the aforementioned issues and challenges to meet the requirement for rapid, high-fidelity and accurate measurement of gas properties in combustion diagnosis. The proposed solutions should be capable of handling the inherent noise in industrial environments by incorporating innovative signal processing techniques and leveraging cutting-edge deep learning-based methods to achieve a comprehensive understanding and reconstruction of gas dynamics within the combustion process. Specifically, this project consists of three main objectives:

(1) Develop an advanced spectroscopic calculation method for signal post-processing of single LoS-LAS measurement that achieves both high accuracy and speed. Although the current calibration-free spectral analysis algorithm facilitates the implementation of the LAS technique into vibrant and harsh environments, its

inherent curve-fitting scheme hinders real-time diagnosis capability. The required method should not only effectively capture absorption information with strong noise resistance, but also reconstruct the gas properties at a fast response.

(2) Develop an efficient data-driven algorithm for LAS tomography that is tailored for quasi-static and dynamic reactive flows, achieving high accuracy and low computational complexity. By establishing two different datasets targeting corresponding exhaust situations, with the integration of the Computational Fluid Dynamics (CFD) model into the generation of reactive flow fields, the datasets are expected to preserve the intrinsic characteristics of the gas-property distributions. Subsequently, this model should be incorporated with an appropriately configured neural network to effectively capture the dynamics of the combustion process. This algorithm is required to demonstrate the enhanced spatial solution in the reconstructions with fewer artifacts, as well as accelerate the inverse reconstruction process.

(3) Create a novel training-free image reconstruction algorithm in LAS tomography to facilitate simultaneous retrieval of temperature and species concentration during the combustion process. Traditional deep learning approaches often suffer from heavy reliance on extensive datasets and a lack of embedded physical knowledge, which can compromise their applicability and generalizability in real-world applications. The developed algorithm aims to overcome the limitations by eliminating dependence on the dataset and incorporating physical principles inherent to LAS tomography, thereby enhancing both the robustness and reliability of the reconstruction process in multiple scenarios.

1.3 Main Contribution

The main contributions of this thesis are summarized as follows:

(1) A novel hybrid model-driven neural network, named HMD-WMS, is developed to reveal the path-average temperature for GTE diagnosis. This model leverages Wavelength Modulation Spectroscopy (WMS), a foundational technique in LAS, by integrating the core physical absorption principles with the exper-

imental model of WMS. HMD-WMS enables strong industrial generalizability and stability on temperature retrieval. This algorithm is tailored to preserve both the temporal and spatial information of the spectral curve while minimizing the noise effects, thus leading to a more accurate temperature value.

(2) To reconstruct temperature distributions in dynamic combustion flow fields, a supervised CNN-based algorithm has been developed. This method utilizes two distinct training sets: one simulating the reactive flows of a ten-injector annular combustor using customized multiple Gaussian profiles, and the other modeling a circular burner's combustion process generated by Fire DynamicS Simulator (FDS). These training sets provide a comprehensive foundation for the Convolutional Neural Network (CNN) to accurately retrieve temperature distributions within the sensing region. Without considering the artifacts in the training set, this algorithm reliably predicts the combustion status with higher spatial resolution, offering a significant improvement in both accuracy and utility for practical combustion analysis. Numerical simulations have validated this new approach, demonstrating its accuracy and sensitivity in monitoring dynamic flames.

(3) A novel dataset-free and training-free image reconstruction algorithm, named Model-informed Double Image Prior (MI-DIP), is proposed for high-fidelity and effective reconstruction of both temperature and gas species concentration. This algorithm is fully independent of training datasets, thus eliminating simulation-introduced errors and further enhancing its generalization in real scenarios.

1.4 Thesis Outline

This thesis consists of six main chapters. The remaining parts are structured as follows.

Chapter 2 builds upon the comprehensive introduction provided in the preceding chapter, focusing on the literature review of LoS-LAS for gas-parameter measurement and LAS tomography for gas imaging. ThIS chapter begins by explaining the principles of LAS measurement techniques, including the Beer-Lambert law and the mathematical models of three classical lineshape functions in LAS. Next, it introduces two fundamental schemes of LAS: Direct Absorption Spectroscopy (DAS) and

WMS. Following this, the chapter delves into the mathematical formulation of LAS tomography and its inherent inverse problem. A review of traditional reconstruction methods is provided, alongside a discussion of the latest advancements in deep learning-based imaging algorithms.

In Chapter 3, a model-driven spectroscopic network, named HMD-WMS is introduced for capturing the path-averaged exhaust gas temperature. Here, the architecture of HMD-WMS with the combination of the knowledge of WMS will be first demonstrated, followed by a detailed description of dataset construction and the experiment setup. Then, the proof-of-concept experiment conducted on a gas turbine is presented to validate the proposed signal processing algorithms for LoS-LAS.

The focus of Chapter 4 is LAS tomography, where a CNN-aided temperature imaging algorithm is presented. This chapter will first introduce the construction of two different datasets targeting an annular combustor with ten injectors and a circular burner simulated by FDS, respectively. Then more details about the setup of the simulation are put forward, which is followed by the introduction of the architecture of CNN when applying it to LAS tomography. Finally, the simulation results after obtaining the optimal trained model will be showcased.

Chapter 5 solves the potential issue when the simulated dataset is not capable of representing the characteristics of the combustion process in real scenarios, where a dataset-free Untrained Neural Network (UNN)-based algorithm is introduced for joint reconstruction of temperature and species concentration. It will provide a detailed illustration of the whole algorithm, including the architecture of the involved neural network, named AD-CNN, its optimization process, and the innovative soft-threshold scheme for regularization.

Ultimately, Chapter 6 will provide a comprehensive summary of the scientific contribution of this PhD project and explore ideas for further enhancements, with a focus on the mitigation of the ill-posedness of the LAS tomography and the improvement of both temporal and spatial resolution in deep learning-based gas imaging algorithms.

Chapter 2

Literature Review

2.1 Introduction

Following the development of direct current injection semiconductor lasers in the late 1960s, the practical and potential utility of the Tunable Diode Laser (TDL) based on absorption spectroscopic measurement was acknowledged [15]. Shortly thereafter, Hanson *et al* [27] first applied the diode laser to the *in situ* measurement of combustion gases in the 1970s. Moving to the 1990s, diode laser absorption spectroscopy became one of the most powerful techniques for gas sensing [28; 29; 30], where it provides significant advantages in the measurements of multiple flow-field parameters such as temperature, pressure, velocity, and density. The exploration of LAS in a short period receives the credit for its high sensitivity, high spectral resolution, fast time response, robustness and non-intrusive [31], as well as the cost-effectiveness, compactness, and high detection sensitivity of TDL sensors. Followed by the invention of advanced signal processing methods, LAS has demonstrated its applicability and reliability in harsh industrial scenarios. In addition, compared to the single-beam LAS for obtaining the path-average gas parameters, LAS tomography, a technique combined with tomography to reconstruct the 2D distributions in the region of detection, can provide a more effective diagnosis of complicated combustion phenomena [32]. However, due to the inherent ill-posedness of the inverse problem in LAS tomography, the reconstructions suffer from poor spatial resolution and severe artifacts. Advanced algorithms can be developed to enhance the performance of gas imaging in LAS tomography.

In this chapter, the physical principle of the LAS technique, Beer-Lambert absorption law, will be primarily introduced. Afterward, based on different broadening mechanisms, three main absorption lineshape functions, i.e., the Gaussian lineshape function, the Lorentzian lineshape function, and the Voigt lineshape function, are explained, with their corresponding features and applications. A comprehensive over-

view of two widely used LAS implementations, Direct Absorption Spectroscopy (DAS) and Wavelength Modulation Spectroscopy (WMS), will be provided. The attention will then be directed toward the LoS-LAS measurement configuration, with an in-depth discussion on signal post-processing techniques utilizing both traditional and data-driven methods. Finally, the focus will shift to LAS tomography, discussing the inherent challenges of its ill-posed nature and exploring various methods employed to address these issues.

2.2 LAS Fundamentals

2.2.1 Beer-Lambert Law

Beer-Lambert law is the fundamental principle of LAS technique [33; 14]. It reveals the absorption of light passing through a uniform absorbing medium by giving the mathematical relationship between the incident and transmitted laser signal intensities. In the case of LAS, as shown in Figure 2.1, when an incident laser beam at the wavenumber ν [cm^{-1}], noted as $I_0(\nu)$, penetrates the targeted gaseous medium with a length of L_{abs}. Its intensity will be partially absorbed, where it is noted as $I_t(\nu)$. This process can be expressed as:

$$I_t(\nu) = I_0(\nu) \times e^{-\alpha(\nu)} \tag{2.1}$$

where $\alpha(\nu)$ is defined as the absorbance at the specific wavenumber. Its formulation is:

$$\alpha(\nu) = P \int_0^{L_{\text{abs}}} X_{\text{abs}}(l_{\text{abs}}) S(T(l_{\text{abs}})) \phi \, dl_{\text{abs}}, \tag{2.2}$$

where P [atm] is the local pressure, $X_{\text{abs}}(l)$ and $T(l_{\text{abs}})$ [K] the local species concentration and temperature at the location of l_{abs}. $S(T)$ [cm^{-2}atm^{-1}] is the temperature-dependent line strength, and ϕ [cm] is the lineshape function of the species-specific transition. It is defined to satisfy the unity normalization as:

$$\int_{-\infty}^{+\infty} \phi \, d\nu \equiv 1 \tag{2.3}$$

Therefore, the path-integrated absorbance noted as A [cm^{-1}], is defined as the integration over the selected wavelength v, which can be expressed as:

$$A = \int_{-\infty}^{+\infty} \alpha(v)dv = P\int_{0}^{L_{\text{abs}}} X_{\text{abs}}(l_{\text{abs}})S_v(T(l_{\text{abs}}))dl_{\text{abs}} \tag{2.4}$$

Assuming the gas in the sensing region is uniformly distributed, the integrated absorbance A in Eq.(2.4) can be calculated as:

$$A = PX_{\text{abs}}S(T)L_{\text{abs}} \tag{2.5}$$

2.2.2 Lineshape Function

Ideally, the change in a molecule's total internal energy corresponds to a transition between the discrete energy levels at specific frequencies, resulting in the narrow frequency range in spectral transition lines. In practice, thermal and collisional processes will cause the broadening phenomenon on the spectral lines [15], leading to both uniform and non-uniform broadening. This broadening affects the measured spectral lines, which typically exhibit a specific lineshape function ϕ and a certain broadening width. The lineshape function ϕ is influenced by various parameters, such as temperature, pressure and gas concentration. The maximum value of the lineshape function, noted as $\phi(v_0)$, is located at the center of the absorption line, while the spectral linewidth is defined as the Full Width at Half Maximum (FWHM) of the lineshape function's maximum value. Lineshape functions are primarily divided into three categories: Gaussian lineshape, Lorentzain lineshape, and Voigt lineshape. The following will provide a detailed explanation of each lineshape function and the corresponding broadening mechanisms.

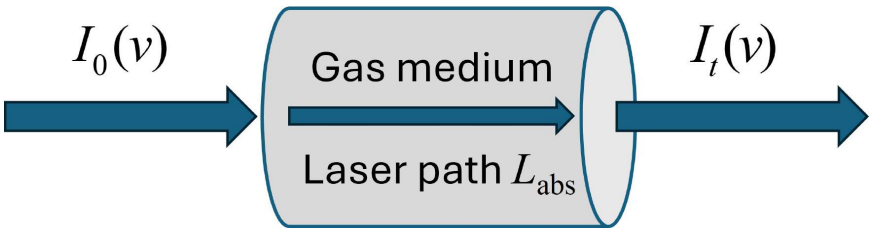

Figure 2.1: Schematic of LAS measurement

Gaussian Lineshape Function

The thermal motion of molecules in the absorbing state leads to the Doppler broadening effect, resulting in Gaussian lineshape [34]. It often occurs when the molecules have the velocity component in the same/opposite direction of the laser photon propagation, with a Doppler-shifted frequency. Due to a large range of velocities of the molecules, Doppler broadening is regarded as non-uniform broadening. The distribution of molecular speeds follows the Maxwellian Velocity-Distribution Function (VDF) [35], which can be formulated as:

$$v = \left(\frac{2kT\ln 2}{m}\right)^{1/2} \tag{2.6}$$

where k [J/K] is the Boltzmann constant and m is the molecule's mass. Then, the FWHM Δv_D caused by the Doppler shifted frequency, also named Doppler width, can be calculated:

$$\Delta v_D = v_0\sqrt{\frac{8kT\ln 2}{Mc^2}} = 7.1623\times 10^{-7} v_0\sqrt{\frac{T}{M}} \tag{2.7}$$

where v_0 is the linecenter frequency. M is the molecule mass and c the light speed. Afterward, the Doppler/Gaussian lineshape, which is characterized by a classical Gaussian curve, is:

$$\phi_D(v) = \frac{2}{\Delta v_D}\sqrt{\frac{\ln 2}{\pi}}\exp\left(-4\ln 2\left(\frac{v-v_0}{\Delta v_D}\right)^2\right) \tag{2.8}$$

As indicated in Eq.(2.7), the Doppler FWHM is solely determined by the local temperature. It showcases that a higher temperature will cause a larger Doppler width and broader spectral transition line. Therefore, the Gaussian lineshape will dominate when the temperature varies at a low pressure.

Lorentzian Lineshape Function

In high-pressure environments, uniform broadening becomes more dominant than non-uniform broadening, leading to the Lorentzian Lineshape. This type of broadening is mainly affected by two mechanisms: natural broadening and collisional broadening [36]. Natural broadening originates from the uncertainty of the energy states of molecules in the absorption transitions with a finite lifetime. However, due to the long

lifetime of the energy states [31], the effect of natural broadening is not trivial and can be neglected in most situations. In terms of collisional broadening, it is caused by the collisions of the absorbing molecules with other molecules. Collisions can reduce the average lifetime of a molecule and result in a broader absorption lineshape. This lineshape function $\phi_c(v)$ is described in the form of Lorentzian profile:

$$\phi_c(v) = \frac{1}{2\pi} \frac{\Delta v_c}{(v - v_0)^2 + (\frac{\Delta v_c}{2})^2} \tag{2.9}$$

Here, Δv_c is the collisional FWHM, which can be further formulated as:

$$\Delta v_c = P \sum_j (X_j 2\gamma_j) \tag{2.10}$$

where there are in-total J species components and X_j is the mole fraction of the j^{th} component. γ_j [cm^{-2}atm^{-1}] is the broadening coefficient caused by j^{th} component's perturbation, which can be expressed as:

$$\gamma_j(T) = \gamma_j(T_0) \left(\frac{T_0}{T} \right)^{n_j} \tag{2.11}$$

where T_0 is the reference temperature 296 K and n_j is the coefficient of indicating temperature dependence. As shown in Eq.(2.10), the pressure is the critical on the lineshape broadening. Typically, the collisional broadening will be taken into consideration when the pressure is higher than 0.1 atm.

Voigt Lineshape Function

For *in situ* scenarios near atmosphere pressure, the lineshape function of the spectral transitions is usually formulated as a Voigt profile, containing both thermal and collisional broadening [15]. Specifically, the Voigt lineshape function can be obtained by the convolution of the Gaussian lineshape and the Lorentzian lineshape [37]:

$$\phi_v(v) = \int_{-\infty}^{+\infty} \phi_D(v) \phi_c(v - u) du \tag{2.12}$$

To illustrate the relationship between Doppler broadening and the collisional broadening, the parameter α is defined as:

$$\alpha = \frac{\sqrt{\ln 2} \Delta v_c}{\Delta v_D} \tag{2.13}$$

with the nondimensional line position parameter w as:

$$w = \frac{2\sqrt{\ln 2(v - v_0)}}{\Delta v_D} \tag{2.14}$$

and the integral variable y as:

$$y = \frac{2u\sqrt{\ln 2}}{\Delta v_D} \tag{2.15}$$

Finally, the Voigt lineshape function can be expressed as:

$$\phi_v(v) = \frac{2}{\Delta v_D}\sqrt{\frac{\ln 2}{\pi}}\frac{a}{\pi}\int_{-\infty}^{+\infty}\frac{\exp(-\mathrm{y}^2)}{a^2+(w-y)^2}dy = \phi_D(v_0)\frac{a}{\pi}\int_{-\infty}^{+\infty}\frac{\exp(-\mathrm{y}^2)}{a^2+(w-y)^2}dy \tag{2.16}$$

Particularly, the parameter α controls the correlation of the Voigt lineshape function with the Gaussian and Lorentzian lineshape. When the value of α is approaching 0, Gaussian lineshape will be the dominant of the Voigt lineshape function. In contrast, when α goes to infinity, Voigt lineshape will evolve to the Lorentzian lineshape.

Indicated by Eq.(2.12), the convolution operation is involved into the calculation of the Voigt lineshape function, which is not available for analytical solution. Olivero [38] and Mayinger [39] provided an empirical form on the estimation of the Voigt line width, including FWHM and the peak height. The FWHM of the Voigt lineshape can be estimated as:

$$\Delta v_v = 0.5346\Delta v_c + \sqrt{(0.2166{\Delta v_c}^2 + {\Delta v_D}^2)} \tag{2.17}$$

and the peak height of the Voigt lineshape center is:

$$\phi_v(v_0) = \left(\frac{\beta}{\Delta v_{\mathrm{ED}}\sqrt{\pi}}\right) + 2\left(\frac{1-\beta}{\pi\Delta v_c}\right) \tag{2.18}$$

where

$$\beta = \frac{\Delta v_{\mathrm{ED}}}{\Delta v_c/2 + \Delta v_{\mathrm{ED}}} \tag{2.19}$$

$$\Delta v_{\mathrm{ED}} = \frac{\Delta v_c}{2\sqrt{\ln 2}} \tag{2.20}$$

2.3 LoS-LAS Techniques

The LoS-LAS techniques provide quantitative analysis of the gas properties for uniform combustion. Based on the wavelength tuning schemes of the laser sources, they can be categorized as DAS and WMS. Due to high robustness and accuracy by minimizing the impact of laser wavelength drift on the measurements, scanned-wavelength approach is preferred for the implementation of LAS techniques than fixed-wavelength. More detailed introduction on scanned-wavelength DAS and WMS will be provided.

2.3.1 Direct Absorption Spectroscopy

DAS is widely employed into various fields because of its easy implementation, free of calibration and good temporal resolution [16]. The gas properties can be inferred by directly tuning the laser frequency over the selected absorption transition. A common experimental schematic of the DAS implementation is shown in Figure 2.2(a). Typically, TDL is driven and tuned by a ramp signal over the desired absorption features. The generated incident laser signal is then split into two paths: One passes through the gaseous medium and is detected by the receiver at the end of the optical path, while the other is directly through an interferometer to obtain the laser wavenumber-time relationship, noted as $v(t)$, as shown in Figure 2.2(b). Transforming the intensity signal from the time domain to the laser wavenumber domain is crucial for determining the gas properties. Commonly used interferometers for characterizing the laser wavenumber include ring resonator, Fabry-Pérot interferometer (etalon) [40] and Mach-Zehnder interferometer [17], each with a known Free Spectral Range (FSR). As indicated in Figure 2.2(c), these devices will intake the incident laser signal and perform multiple reflections between two reflecting surfaces, resulting in an oscillated output. The wavenumber difference between two adjacent peaks equals to an FSR, allowing $v(t)$ to be quantified for the exploration on the relationship between wavenumber and time.

Figure 2.2(c) demonstrates the signal processing of DAS, presenting the transmitted laser intensity and the corresponding absorbance. The incident laser intensity from TDL can be obtained by polynomial-fitting the non-absorbed region. Thus, the absorption feature will be extracted by directly subtracting the transmitted laser signal from the fitted non-absorbed baseline.

DAS technique offers several advantages:

(1) The measurement of non-absorbed signals is unnecessary, as the baseline can be obtained by polynomial fitting.

(2) Fast time response and simple implementation make DAS widely used in multiple industrial scenarios.

However, its disadvantages need to be taken into consideration:

(1) Applying DAS in high-pressure environments is challenging due to the broadened spectral lineshape. This broadening can cause the spectral lines to exceed the selected wavenumber range, leading to uncertainties in gas property extraction.

(2) In most harsh combustion applications, the detected signals can be disturbed by the high turbulence and dynamic thermal conditions, making it difficult to recover an accurate non-absorbed baseline.

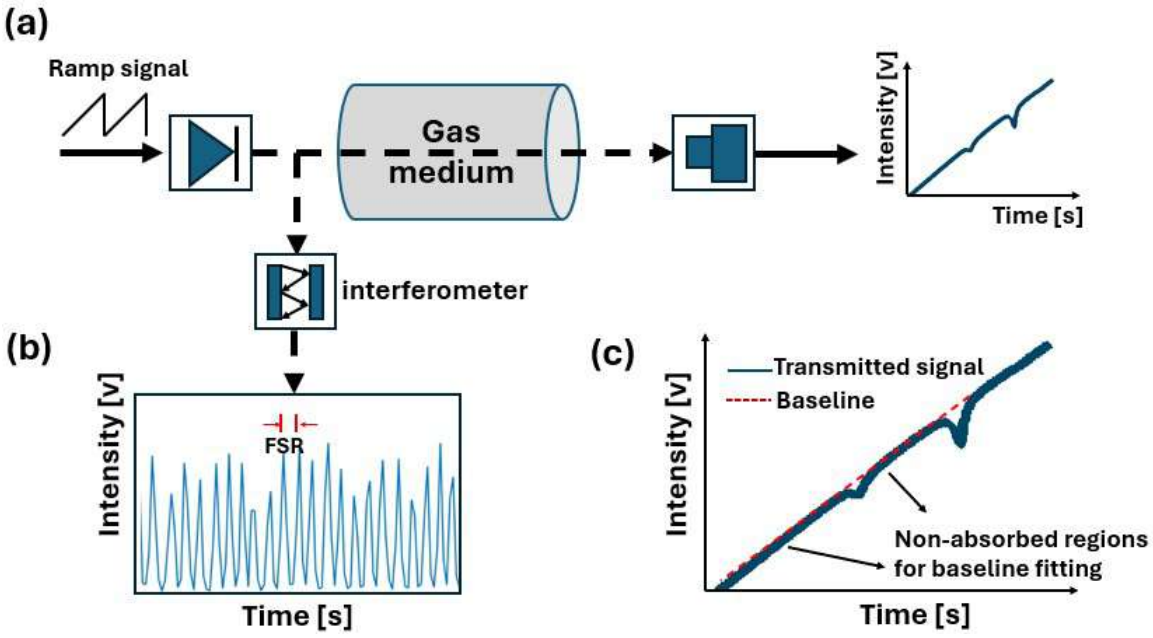

Figure 2.2: Implementation of DAS: (a) Schematic of DAS experimental setup. (b)Laser wavenumber vs. time. (c) DAS signal processing using baseline fitting.

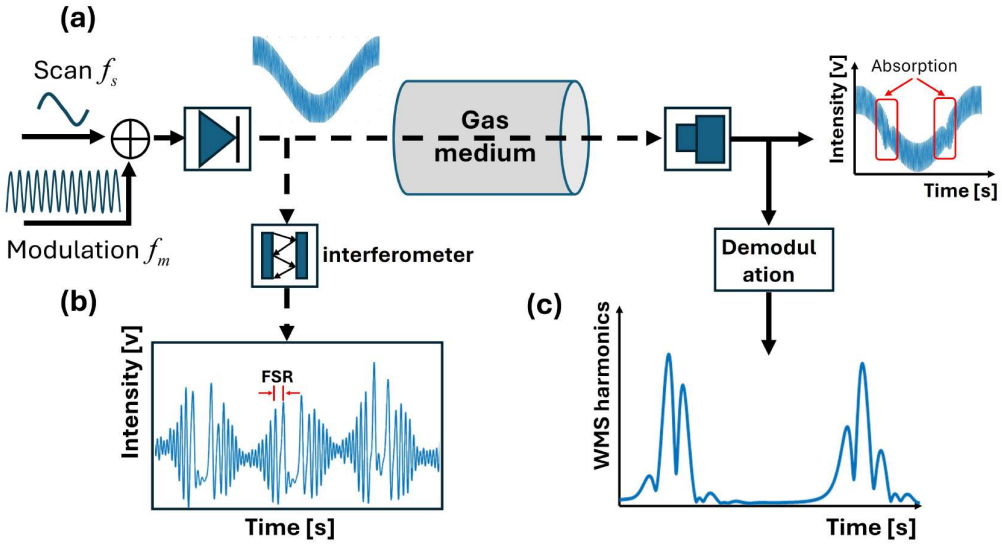

Figure 2.3: Implementation of WMS: (a) The schematic of WMS measurement. (b) The relationship between laser wavenumber and time. (c) The demodulated WMS harmonics.

2.3.2 Wavelength Modulation Spectroscopy

In harsh environments, high pressure, low absorption and unpredictable noise conditions will perturb the non-absorbed regions of the lineshape, making it difficult to obtain the baseline for DAS. In contrast, the WMS scheme is advantageous for high-accuracy and high noise-robustness measurements [41]. The driving signal of WMS is a low-frequency scene f_s [Hz] superimposed with by a relatively high-frequency scan f_m [Hz]. WMS analyses the harmonic components of the received signals to quantify the gas parameters instead of directly calculating the absorbance. Working on the higher-frequency domain significantly reduces the effect of low-frequency noise and obtains much higher measurement Signal-to-Noise Ratio (SNR).

Figure 2.3 showcases the implementation of WMS in the experiments. In (a), a low-frequency sinusoidal signal is superimposed on a high-frequency sinusoidal modulation to drive the TDL, thus generating a modulated laser intensity. Compared to the ramp signal used in DAS, the sinusoidal signal has a smooth transition, thereby improving the time response of the devices. The modulated incident signal can be

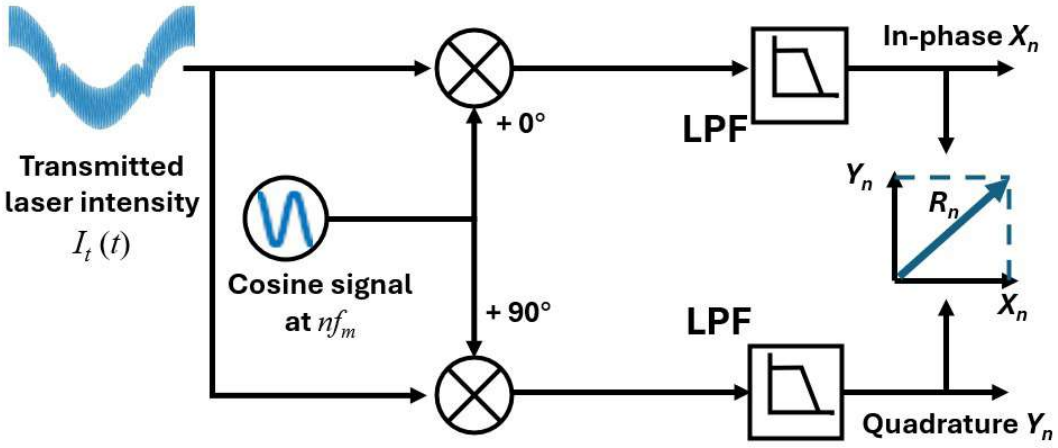

Figure 2.4: The schematic of Lock-in Amplifier and Low-Pass Filter for WMS demodulation.

formulated as:

$$v(t) = \bar{\nu}_0(t) + a_s \cos(2\pi f_s t) + a_m \cos(2\pi f_m t) = \bar{\nu}(t) + a_m \cos(2\pi f_m t) \tag{2.21}$$

where $\bar{\nu}_0(t)$ [cm^{-1}] is the central laser wavelength before modulation. a_s and a_m are the scan amplitude and modulation amplitude, respectively. The incident laser intensity $I_0(t)$ is modeled by:

$$I_0(t) = \bar{I}_0[1 + i_1 \cos(2\pi f_m t + \phi_1) + i_2 \cos(4\pi f_m t + \phi_2)], \tag{2.22}$$

where $\overline{I_0}$ is the average laser intensity when the wavelength is $\bar{\nu}$. i_1 is the amplitude of the linear Intensity Modulation (IM), ϕ_1 the phase shift between the IM and Frequency Modulation (FM), whereas i_2 the amplitude of non-linear IM with phase shift ϕ_2 [42]. Then, the modulated laser signal will be divided into two paths. Similar to DAS, one passes through the interferometer to obtain the wavenumber-time relationship (Figure 2.3(b)). The other penetrates the gaseous medium, which is later detected by the receiver and its harmonics will be extracted through demodulation. To accurately analyze the relationship between the absorbance and the harmonic components of

the received laser signal, the transmission coefficient $\tau(v)$ is leveraged:

$$\tau(v) = \frac{I_t}{I_0} = e^{-A\phi(v)} \tag{2.23}$$

After modulation, $\tau(v)$ now is an even function in $2\pi f_m t$, which can be expanded into Fourier cosine series:

$$\tau(\overline{v} + a\cos(2\pi f_m t + \phi) = \sum_{n=0}^{n=+\infty} H_n(\overline{v}, a)\cos(n2\pi f_m t) \tag{2.24}$$

where $H_n(\overline{v}, a)$ is the n^{th} order harmonic component of the transmission coefficient. It is given by:

$$H_0(\overline{v}, a_m) = \frac{1}{2\pi}\int_{-\infty}^{+\infty} \tau(\overline{v} + a_m\cos\theta)d\theta \tag{2.25}$$

and

$$H_n(\overline{v}, a_m) = \frac{1}{\pi}\int_{-\infty}^{+\infty} \tau(\overline{v} + a_m\cos\theta)\cos(n\theta)d\theta \tag{2.26}$$

In terms of signal demodulation, the digital Lock-in Amplifier and Low-Pass Filter (LPF) are utilized to extract the harmonic components from the transmitted signal. Figure 2.4 demonstrates the whole demodulation process of WMS. Generally, the transmitted signal $I_t(t)$ will multiply the cosine and sinusoidal reference signals to 'lock-in' the in-phase and quadrature components, respectively. Then, its in-phase and quadrature components noted as X_{nf} and Y_{nf} are obtained after filtering by an LPF with the frequency of $n \cdot f_m$. The usage of Lock-in Amplifier and LPF avoids the complex Fourier expansion of the scanned and the modulated laser intensity and wavelength [41]. As the magnitude of the harmonics will decrease with the increase of its order, only the first and second harmonic components will be leveraged in most situations.

To reduce the effect of noise caused by the background absorption and detection system, Calibration-Free WMS (CF-WMS) [43] was developed and has been widely applied to industrial experiments. In CF-WMS, the harmonics of the $2f$ signals will be normalized by the harmonics of the $1f$ signals, denoted as WMS-$2f/1f$:

$$\text{WMS-}2f/1f = \sqrt{\left[(\frac{X_{2f}}{R_{1f}})_{\text{raw}} - (\frac{X_{2f}}{R_{1f}})_{\text{bg}})\right]^2 + \left[(\frac{Y_{2f}}{R_{1f}})_{\text{raw}} - (\frac{Y_{2f}}{R_{1f}})_{\text{bg}})\right]^2} \tag{2.27}$$

and

$$R_{1f} = \sqrt{X_{1f}^2 + Y_{1f}^2} \tag{2.28}$$

where $(\cdot)_{\text{raw}}$ and $(\cdot)_{\text{bg}}$ indicate the absorbed and non-absorbed signals, respectively. X_{2f} and Y_{2f} are the in-phase and quadrature components of the $2f$ harmonics, whereas X_{1f} and Y_{1f} are the in-phase and quadrature components of the $1f$ harmonics. R_{1f} is the amplitude of the $1f$ harmonics.

2.4 LoS-LAS Measurement Configuration

A detailed illustration of LAS configuration to obtain accurate and robust gas properties is provided in this section, including the ratio thermometry and signal post-processing of CF-WMS. For simplicity, CF-WMS will be referred to as WMS throughout the remainder of the thesis.

2.4.1 Ratio thermometry

It can be seen from Eq.(2.4) that the integrated absorbance A is determined by the optical path length L_{abs}, the pressure P, gas species concentration X_{abs} and the temperature-dependent line strength $S(T)$. During the experiments, the path length can be easily measured and the pressure is typically considered to be atmospheric pressure for unconfined reactive flows. Therefore, there are two unknown parameters to be calculated: the species concentration X_{abs} and the temperature T. To simultaneously determine T and X_{abs}, multiple measurements with different transitions are required.

Ratio thermometry [44; 45], also known as two-color strategy, is widely adopted in WMS temperature measurement by leveraging two laser signals targeting the same gas samples with different absorption transitions. Specifically, after obtaining the integrated absorbance from two laser beams, noted as A_1 and A_2, the ratio of them can be formulated as:

$$R = \frac{A_2}{A_1} = \frac{S_2(T)}{S_1(T)} = \frac{S_2(T_0)}{S_1(T_0)} \exp\left(-\frac{hc}{k}\left(E_2'' - E_1''\left(\frac{1}{T} - \frac{1}{T_0}\right)\right)\right) \tag{2.29}$$

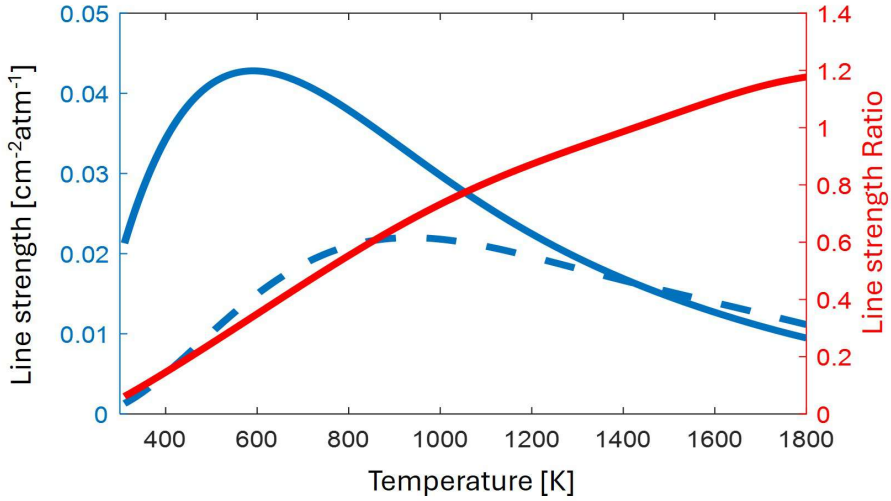

Figure 2.5: The line strength of two selected absorption transitions and their ratios when the temperature varies from 300 K to 1800 K.

where $S_n(T_0), n \in \{1,2\}$ is the known line strengths at the reference temperature T_0 = 296 K, provided by HITRAN spectrum database [46]. h [J · s] is Planck constant and c [cm/s] is the light speed. k [J/K] is Boltzmann's constant and $E''[\mathrm{cm}^{-1}]$ is the low-state energy of the transition.

As indicated in Eq.(2.29), the ratio R eliminates the effect of species concentration and is solely determined by the temperature. Thus, the temperature can be calculated:

$$T = \frac{\frac{hc}{k}(E_1'' - E_2'')}{\ln\frac{A_2}{A_1} + \ln\frac{S_1(T_0)}{S_2(T_0)} + \frac{hc}{k}\frac{E_1''-E_2''}{T_0}} \tag{2.30}$$

As shown in Figure 2.5, the line strengths of two absorption transitions for water vapor and their corresponding ratio exhibit a monotonic relationship as the temperature varies from 300 K to 1800 K. Thus, compared to the single line strength, this strategy showcases a promise on wider temperature-range absorption measurement [47].

Afterward, the gas species concentration of the targeted gas sample can be calculated via:

$$X_{\text{abs}} = \frac{A}{P \cdot L_{\text{abs}} \cdot S(T)} \tag{2.31}$$

2.4.2 LoS-LAS Signal Post-Processing

Exploring the effective post-processing techniques for LoS-LAS signals, particularly for retrieving the gas parameters, is important. Advanced algorithms allow accurate and rapid signal processing, thereby enhancing efficiency in industrial applications. In this section, both the conventional signal post-processing algorithms and the learning-based methods are reviewed and discussed.

Spectral fitting of WMS

Although the peak value of the WMS-$2f/1f$ signals can be chosen for calibration-free measurement of gas properties with high temporal response, it is not robust to handle uncertainties and signal contamination caused by the environment and other optical devices [16]. Instead, the spectral fitting method based on the scanned WMS technique can infer the gas parameters from least-squares fitting the simulated WMS-$2f/1f$ to the measured WMS-$2f/1f$ without the requirement of prior information of the transition linewidth [48; 49].

Figure 2.6 shows the flow chart of spectral fitting WMS-$2f/1f$ with procedures listed as follows:

(1) By assuming the initial value of the modulation linecenter frequency v_0, the Doppler and collision broadening Δv_D and Δv_c and the integrated absorbance A, the simulated wavelength-dependent absorbance ${}^s\alpha(v)$ can be calculated based on the HITRAN database.

(2) After processing the signals from the interferometer, the simulated time-dependent absorbance ${}^s\alpha(v(t))$ can be determined with the expression of the laser wavenumber versus time.

(3) Given the measured incident laser intensity ${}^M I_0(t)$, the simulated transmitted laser intensity ${}^s I_t(t)$ can be calculated with Beer-Lambert Law using Eq.(2.2).

(4) Both the measured transmitted laser intensity ${}^M I_t(t)$ and ${}^s I_t(t)$ will go through identical Lock-In Amplifier and LPF to obtain the corresponding WMS-$2f/1f$.

(5) The simulated WMS-$2f/1f$ will be fitted to the measured WMS-$2f/1f$ using a least-squared approach by adjusting the gas parameters mentioned above. Ultimately, this fitting method will output the spectral absorption parameters once it converges.

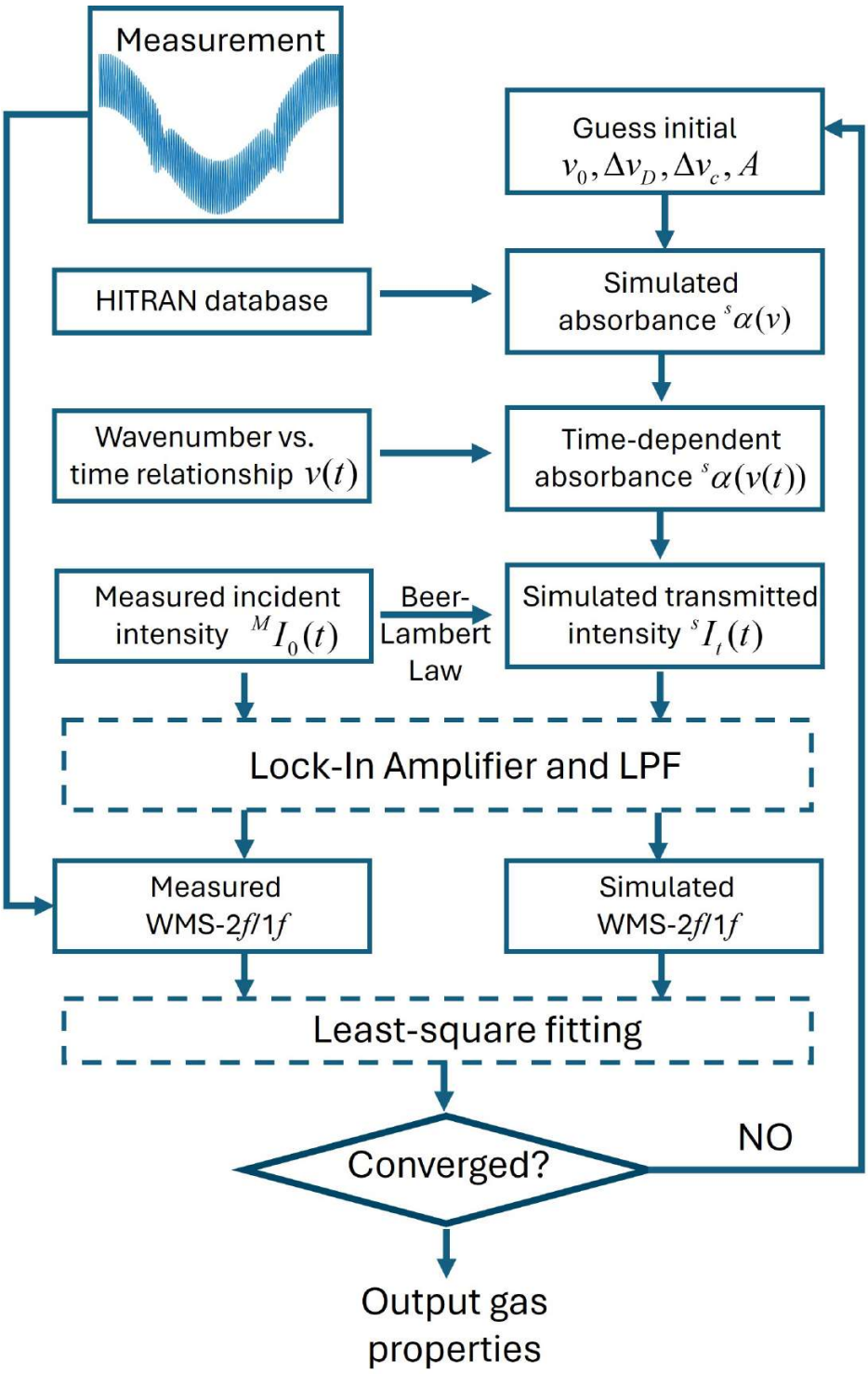

Figure 2.6: Flowchart of fitting WMS-$2f/1f$ method.

Specifically, the usage of ${}^{M}I_0(t)$ can effectively avoid the complicated modeling of laser intensity for the response of the scan and modulation, as well as the uncertainties caused by optical and electrical devices. Thus, this spectral fitting method for WMS shows high stability in various industrial situations with good accuracy and noise robustness. However, Figure 2.6 showcases the fitting process of the single WMS-$2f/1f$, whereas the temperature or gas species concentration retrieval requires at least two WMS-$2f/1f$ signals from different absorption transitions based on ratio thermometry mentioned in section 2.4.1. Therefore, to further improve the fitting efficiency, an updated version of the fitting method is shown in Figure 2.7. Compared to the single WMS fitting method, this method would have the initial guess on temperature and concentration instead of integrated absorbance or broadening. Considering two transitions simultaneously allows for end-to-end gas parameter reconstruction and eliminates errors in ratio thermometry that are caused by small turbulence affecting the denominator during the division operation.

However, the inherent iterative nature of both fitting methods results in low computation efficiency on gas properties reconstruction. Typically, it takes hundreds of milliseconds to fit a single WMS-$2f/1f$ signal, severely restricting its application where real-time diagnosis is required.

Data-driven Methods

Due to the exceeding computational efficiency, data-driven algorithms have become popular for accelerating the LAS signal post-processing. Generally, data-driven methods learn the underlying physical absorption information and the features of data distributions by mapping the LAS measurement signals to the desired gas properties through training.

Based on the difference in dataset construction, most data-driven methods can be classified into two categories. The models belonging to the first category are trained solely with simulated signals, which means each training sample is generated through simulation using the HITRAN database. It is easy to obtain up to thousands of signal samples with various temperatures and gas species concentrations. Meanwhile, it is flexible to add different types of noises to the signals to imitate the encountered noise in the real world, such as Gaussian noise and white noise. For example, Xu *et al.* [50] built a novel residual network filter based on a deep learning algorithm to improve the noise robustness of DAS. This residual network establishes a mapping between the input noisy spectra and the denoised spectra by training on a simulated dataset

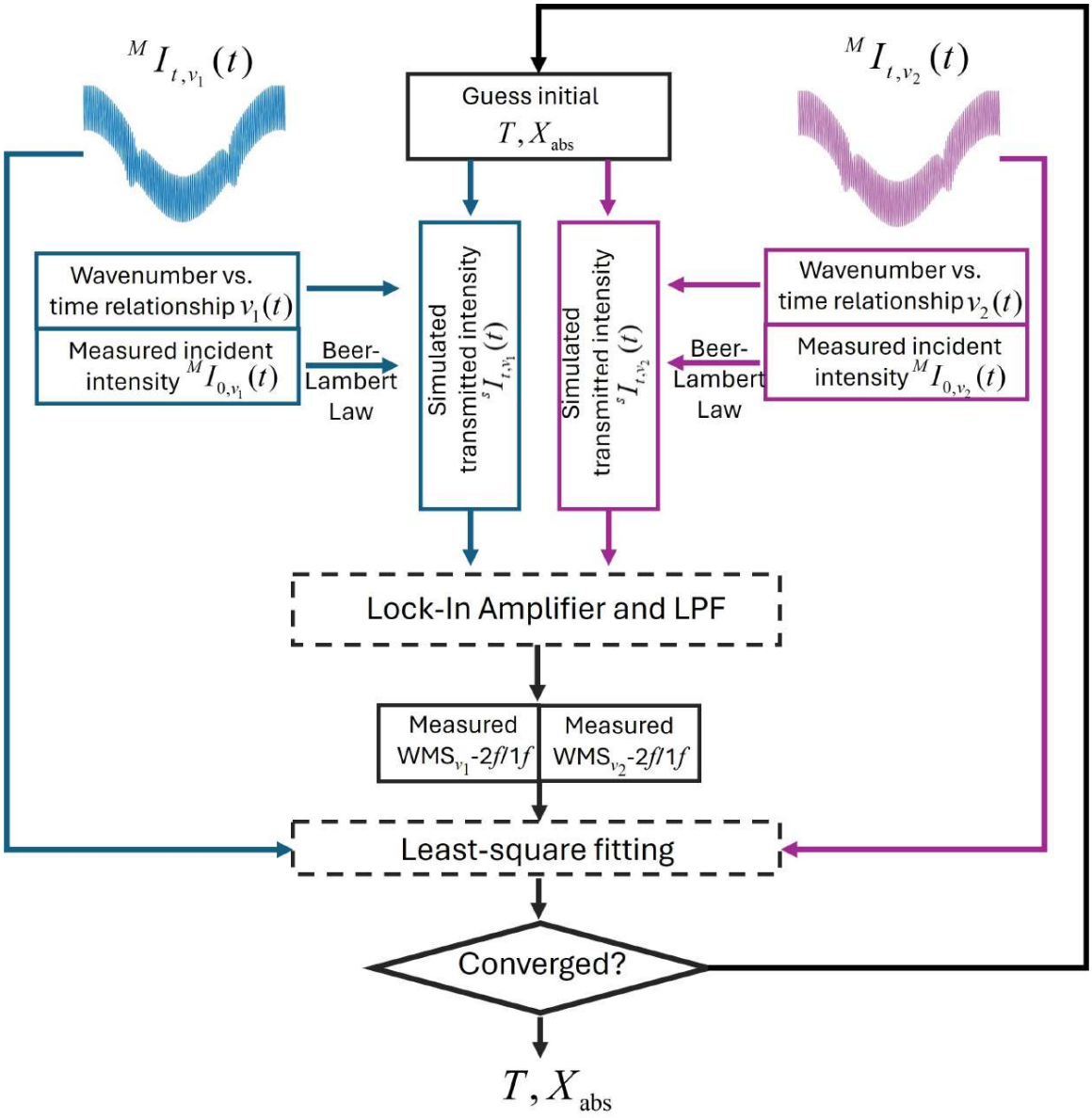

Figure 2.7: Flowchart of fitting two WMS-$2f/1f$ signals to determine the temperature and gas species concentration.

along with the artificially superimposed noise. In addition, Sun *et al.* [51] introduced a physical-motivated Recurrent Neural Network (RNN) by mimicking the fitting process of WMS, in which denoised spectra were incorporated into the training process for concentration reconstruction.

However, the simulated signals are not representative and consistent with the real-world signals. Therefore, the second category modifies the strategy of dataset construction by hybridizing the simulated data and the experimental data. For instance, Tian *et al.* [52] pre-trained a One-Dimensional Convolutional Neural Network (1D-CNN) and deep Multi-Layer Perceptron (MLP) for gas concentration reconstruction using the simulated dataset, followed by the transfer learning on the experimental data. Similarly, Sun *et al.* [53] fed a large amount of both simulated and experimental training samples to solve the problem of spectral overlapping cross-interference. These models showcase improved noise robustness with higher accuracy in certain experiment situations when compared to the models in the first category. However, some challenges can not be neglected: (1) The collected experimental data is not sufficient to cover various situations, thereby heavily restricting the model's generalizability; (2) Sole reliance on the dataset, without assistance from the physical absorption model, limits the accuracy and the robustness of the results.

2.5 LAS Tomography

The aforementioned LoS-LAS technique is developed to retrieve the path-averaged gas properties along the optical path. With the increasing demand for detecting the internal reaction of the flow field, LAS tomography can provide a comprehensive 2D spatial distribution of the flow field. LAS tomography is an imaging technique combined LAS with classical hard-field tomography [54], to retrieve the gas properties from multiple LoS-LAS measurements from different projection angles.

2.5.1 Fundamentals of LAS Tomography

The typical approach to modeling LAS tomography is the uniform discretization of the sensing region, as shown in Figure 2.8. The laser sensing area covers the entire optical path of each emitter-receiver pair, which is called the Region of Sensing (RoS). It can be further divided into two parts: the Region of Interest (RoI), where it is the central square area and the targeted objective is located, and the out-of-RoI region, including the background.

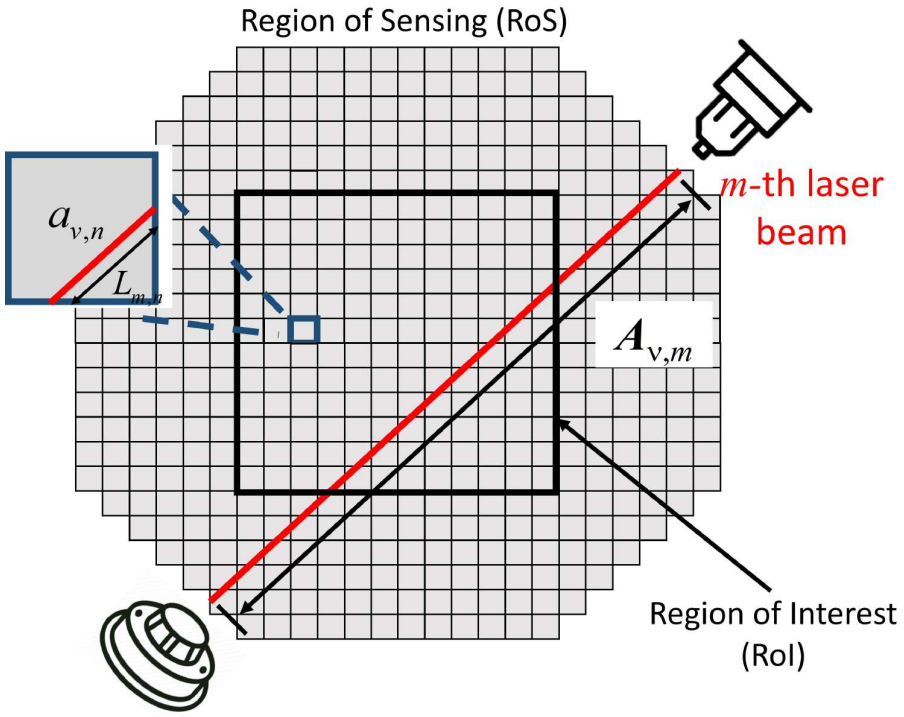

Figure 2.8: The formulation of LAS tomography with the demonstration of LoS-LAS measurement.

As shown in Figure 2.8, this is a M-beam LAS tomography sensor and the RoS is uniformly discretized into N pixels. The targeted gas species concentration, temperature, and other parameters are assumed to be consistent within the pixel. Consequently, the measured integrated absorbance of m-th laser at the absorption transition v, $A_{v,m}$ can be formulated as:

$$A_{v,m} = \sum_{n=1}^{N} PX_n S(T_n) L_{m,n} \tag{2.32}$$

where P [atm] is the local pressure, X_n the mole fraction (concentration) of the absorbing species in the n-th pixel. $S(T_n)$ [cm^{-2}atm^{-1}] is the line strength when the temperature is T_n [K]. Here, the absorption coefficient a_n of n-th pixel is defined as

$$a_n = PX_n S(T_n) \tag{2.33}$$

Therefore, the Eq.(2.32) can be expressed as:

$$A_n = \sum_{n=1}^{N} a_n L_{m,n} \tag{2.34}$$

$$\mathbf{A} = \mathbf{La} \tag{2.35}$$

where $\mathbf{A} \in \mathbb{R}^{M\times 1}$ is the vector of measured integrated absorbance from M-beam LAS tomography system. $\mathbf{L} \in \mathbb{R}^{M\times N}$ is the sensitivity matrix to describe the path length of the laser beam in each pixel. $\mathbf{a} \in \mathbb{R}^{N\times 1}$ is the absorbance density vector, consisting of the pixel-wised absorption coefficients.

2.5.2 Ill-posed Inverse Problem in LAS Tomography

The objective of LAS tomography is to reconstruct the pixel-wised absorbance coefficients from multiple LoS-LAS measurements. However, this task is complicated by several factors. Firstly, the physical environment imposes constraints on the placement and alignment of optical and electrical devices, limiting the available optical access. Secondly, the targeted flow field is large, necessitating a high volume of pixels to maintain a reasonable spatial resolution in the reconstructed images. Consequently, only a limited number of laser beams can be employed for detection, which is much fewer than the number of pixel-wise unknowns that need to be determined. This discrepancy results in a severe ill-posed problem, also known as rank deficiency, where the equation formed by the measurements Eq.(2.35) is underdetermined [55].

One typical way to visualize the rank-deficient nature is to carry out a Singular Value Decomposition (SVD) of the sensitivity matrix $\mathbf{L}$ [56]. SVD is an approach to determine the rank and the nullspace of the matrix, thus testing its stability with noise $\mathbf{L}$ can be decomposed as:

$$\mathbf{L} = \mathbf{USV^T} \tag{2.36}$$

Here, $\mathbf{U} \in \mathbb{R}^{M\times M}$ and $\mathbf{V} \in \mathbb{R}^{N\times N}$ are the orthonormal matrices. $\mathbf{S} \in \mathbb{R}^{M\times N}$ is a diagonal non-negative matrix with a descending order. The values of $\mathbf{S}$ matrix are called the singular value of the matrix $\mathbf{L}$. Assuming there is a full-rank problem, i.e. Rank [$\mathbf{A}$] = M = N, the solution for the reconstruction can be expressed as:

$$\mathbf{a} = \sum_{n=1}^{N} \frac{\mathbf{u}_n^T \mathbf{A}}{\mathbf{s}_n} \mathbf{v}_n \tag{2.37}$$

where $\mathbf{u}_n$ and $\mathbf{v}_n$ are the n-th column vectors of $\mathbf{U}$ and $\mathbf{V}$, respectively. Unfortunately for the rank-deficient problem, there are only M singular values existing in Eq.(2.37), presenting a null space in the reconstructions. Thus, the solution will be re-formulated as:

$$\mathbf{a} = \mathbf{a}^{LS} + \mathbf{a}^{n} = \sum_{i=1}^{M} \frac{\mathbf{u}_i^T \mathbf{A}}{\mathbf{s}_i} \mathbf{v}_i + \sum_{j=1+M}^{N} C_j \mathbf{v}_j \tag{2.38}$$

which contains the least-square component, $\mathbf{a}^{LS} = \arg\min||\mathbf{A} - \mathbf{L}\mathbf{a}||$, and the null-space component $\mathbf{a}^n$ with infinite solutions from the null space of $\mathbf{A}$. In Eq.(2.38), C_j is the j-th element of $\mathbf{C}$ a set of underdetermined scalars for $\mathbf{a}^n$. Therefore, more constraints need to be imposed to improve the stability and accuracy of the reconstructions when solving the inverse problem in LAS tomography.

2.6 Image Reconstruction Algorithms

In the field of LAS tomography, the inherent ill-posedness is raised by the imbalance between the limited number of measurements and the unknowns. Therefore, priors, which are informed assumptions and constraints derived from the physical model, are needed to achieve precise and reliable reconstructions of gas properties. These priors, also known as "*A Priori*" in the Bayesian concept [57; 58], play a crucial role in guiding the reconstruction process by providing additional and necessary information that compensates for the scarcity of measurements. To address this challenge, various reconstruction algorithms have been developed, each with its own set of advantages and disadvantages. A more detailed introduction to some representative algorithms is provided below.

2.6.1 Iterative Algorithms

As briefly mentioned in the previous section, the inverse problem of LAS tomography can be formulated as a least-square function:

$$\hat{\mathbf{a}} = \arg\min||\mathbf{A} - \mathbf{L}\mathbf{a}||_{\mathbf{2}}^{\mathbf{2}} \tag{2.39}$$

As the iteration progresses, the optimal solution for $\mathbf{a}$ will be obtained upon convergence. Two widely used iterative algorithms for LAS tomography are the Algebraic Reconstruction Technique (ART) and the modified Landweber algorithm.

Algebraic Reconstruction Technique

The ART algorithm is well-adopted to address the ill-posedness of tomographic reconstruction. During its iterative process, the required absorbance coefficient $\mathbf{a}$ is updated until they converge to the stable values [59]. The mathematical solution can be expressed as:

$$\mathbf{a}_{i+1} = \mathbf{a}_i + \omega \frac{\mathbf{A}_m - \mathbf{a}_i \mathbf{L}_z}{\mathbf{L}_z^2} \cdot \mathbf{L}_z \tag{2.40}$$

$$\mathbf{L}_z^2 \neq 0 \tag{2.41}$$

where $\mathbf{a}_i$ is the estimated absorbance vector at i-th iteration. ω is a scalar relation parameter. $\mathbf{L}_z$ is the z-th row of the sensitivity matrix $\mathbf{L}$.

ART iteratively refines the absorption coefficients, leading to more accurate reconstructions. Meanwhile, it can handle incomplete and noisy data effectively, making it suitable for real-world scenarios. Furthermore, it can be adapted to various tomographic configurations and can incorporate different types of prior information to improve reconstruction quality.

Modified Landweber algorithm

The Landweber iteration method was originally developed for solving the classical inverse problem existing in x-ray absorption tomography [60] and then further improved and adapted into the field of LAS tomography [61]. In Landweber, an initial guess of $\mathbf{a}_0$ is obtained via linear back-projection, i.e., $\mathbf{a}_0 = \mathbf{L}^{-1}\mathbf{A}$. As the sensitivity matrix $\mathbf{L}$ is rank-deficient, the transpose of the $\mathbf{L}$, $\mathbf{L}^T$, is leveraged to estimate $\mathbf{L}^{-1}$. Afterward, the desired absorbance coefficients can be calculated by taking the gradient of the least-square function Eq.(2.39) with respect to $\mathbf{a}$,

$$\mathbf{a}^{i+1} = \mathbf{a}^i + \lambda_i \mathbf{L}^T (\mathbf{A} - \mathbf{L}\mathbf{a}^i) \tag{2.42}$$

where λ_i is the relaxation parameter which is important for obtaining the accurate and stable solution. The iteration of Eq.(2.42) will coverage if and only if

$$0 < \lambda_i < 2(||\mathbf{L}^T\mathbf{L}||^2)^{-1} \tag{2.43}$$

As mentioned at the beginning of this section, the prior information is necessary to reduce the artifacts induced by the ill-posedness. In general, the smoothness of the temperature/concentration distributions, and the non-negativity can be the strong prior for the sparse measurements in image reconstruction tasks [22]. It can work as the regularization for the inverse problem. The common regularization approach, called Tikhonov regularization, fills the null space of $\mathbf{A}$ with a smoothing matrix $\mathbf{S}$. It is defined as

$$\mathbf{S}_{x,y} = \begin{cases} 1 & \text{if } x = y \\ -1/p & \text{if } x \text{ neighbors } y \\ 0 & \text{otherwise} \end{cases} \tag{2.44}$$

Then, the inverse problem of (2.39) can be updated to:

$$\mathbf{a} = \arg\min \left\| \begin{bmatrix} \mathbf{L} \\ \lambda \mathbf{S} \end{bmatrix} \mathbf{a} - \begin{bmatrix} \mathbf{A} \\ 0 \end{bmatrix} \right\|, \quad \text{s.t.} \mathbf{a} \geq 0, \tag{2.45}$$

Here, λ weights the smoothness and p determines the dimension of the smoothness effect, usually set to be 3.

The modified Landweber algorithm integrates Tikhonov regularization, combining the iterative refinement of the Landweber algorithm with the stability of regularization. This integration enhances robustness, ensuring that reconstructed images are reliable and physically plausible, adhering to the expected smoothness and non-negativity constraints.

2.6.2 Data-Driven Algorithms

The last decade has witnessed the rapid development of deep-learning techniques. Driven by a large amount of data, these algorithms aim to capture the features of the data distribution as strong prior information and build the map between the inputs and the desired outputs.

For the reconstruction task in LAS tomography, some data-driven algorithms have been developed and have shown exciting results. Huang *et al.* [62] firstly put forward the application of deep learning in LAS tomography by utilizing a typical CNN for temperature image reconstruction. As shown in Figure 2.9, this network architecture takes the laser measurements as the input and outputs temperature images, which

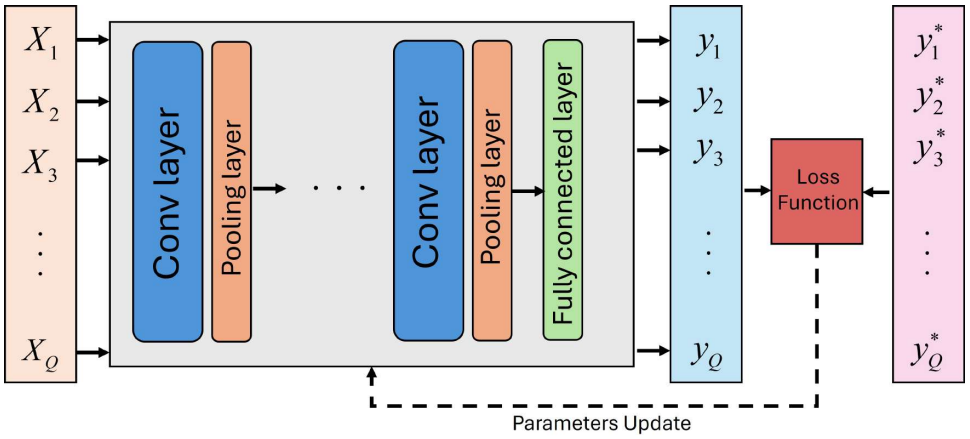

Figure 2.9: The architecture of CNN algorithm

consists of the convolutional layer, the pooling layer followed by the activation function. Before outputting the estimated y_q, the fully connected layer reshapes the latent representation to match the dimension of the reconstructed image. Then, the predicted y_q will be compared to the ground-truth y_q^* $(q \in \{1,2,3,...,Q\})$ to update the trainable parameters. The experimental results shown in this paper demonstrate the capability of deep learning techniques in achieving enhanced noise robustness and superior accuracy compared to traditional iteration-based methods.

In addition, Jiang *et al.* [63] built a novel dual-branch autoencoder, while mapping the laser measurements to the gas properties images. This work proposes the cross-talk mechanism between the temperature branch and the concentration branch to realize simultaneous dual-image reconstructions. Similarly, Wang *et al.* [64] established a Y-shape CNN-based algorithm, trying to obtain the temperature and concentration images from a series of WMS-$2f/1f$ signals directly. As CNN is capable of detecting and learning the spatial hierarchies of features, the aforementioned algorithms have excellent performance on gas properties reconstruction. Besides CNN, Si *et al.* [65] introduces a temperature imaging network based on the Swin Transformer.

Compared to CNN, Swin Transformer can effectively capture long-range contextual features through Multi-headed Self-Attention in both regular and shifted windows. This advancement enhances the precision of temperature imaging in combustion diagnostics.

However, the above algorithms used Gaussian-distributed images as training samples. These samples fail to capture the complexity of gas properties distributions and the turbulence encountered in real-world scenarios. To address this issue, researchers have started to use online reactive flow simulators to mimic practical combustion situations, aiming to construct datasets that are more reliable and realistic.

For example, Si *et al.* [66] developed a data-driven algorithm using simulated FDS data for dataset construction. This method leverages multi-scale imaging to enhance the quality and accuracy of temperature and species concentration imaging. By integrating these advanced simulation techniques, researchers can significantly improve the performance of LAS tomography algorithms, making them more applicable to real-world combustion analysis and diagnostics. This progressive shift towards more sophisticated dataset construction methods marks a critical advancement in the field, ensuring that algorithms are trained on data that closely mirrors actual combustion environments.

However, data-driven methods are often trained on specific datasets that may not cover the full range of variations found in actual combustion environments. For instance, a model trained on data from a laboratory setup may struggle to accurately reconstruct temperature and species concentration distributions in an industrial furnace where conditions differ significantly. Additionally, LAS tomography often involves noisy measurement data, and data-driven methods can be highly sensitive to this noise. In industrial environments where measurement data are contaminated by noise, the performance of these models can degrade significantly, leading to inaccuracies in reconstruction and poor diagnostic outcomes.

Compared to supervised data-driven methods that heavily rely on extensive and high-quality datasets for training, Joseph *et al.* [67] introduced a Physics-Informed Neural Network (PINN) to regularize the inverse problem of LAS tomography. In traditional supervised methods, the model's performance is directly tied to the representativeness and comprehensiveness of the training data. This dependence can be problematic, especially when the available datasets fail to capture the full complexity and variability of real-world combustion environments. For instance, a model trained solely on laboratory-generated data may not perform well when applied to industrial settings

where conditions are vastly different. In this study, Joseph *et al.* utilized a semi-supervised approach by incorporating physical laws directly into the neural network's training process. The PINN framework integrates the Navier-Stokes equations [68], which govern fluid motion, as part of the network's loss function. This integration ensures that the model adheres to fundamental physical principles, thereby reducing its reliance on large datasets and improving its generalizability to different scenarios. Consequently, the PINN framework offers a significant advantage over purely data-driven methods by leveraging both data and physical laws to achieve more reliable and generalizable results in LAS tomography applications.

Despite significant advancements in addressing the ill-posed problem of LAS tomography through deep learning algorithms, concerns remain regarding the reliability and generalizability of these methods when applied to real industrial scenarios. The complex and dynamic nature of combustion processes in industrial environments poses substantial challenges that current models often struggle to overcome. This highlights the necessity for ongoing research and development of more sophisticated algorithms. Enhancing the accuracy and robustness of gas-property reconstruction in such intricate settings is not only challenging but also highly meaningful. It offers the potential to greatly improve diagnostic capabilities and operational efficiency in industrial applications.

2.7 Summary

This chapter provides a detailed literature review on LAS, starting with an introduction to LAS fundamentals, which are essential for understanding light absorption by gas molecules. LoS-LAS techniques are discussed next, highlighting DAS for direct gas concentration measurements and WMS for enhanced sensitivity through laser wavelength modulation. This chapter then covers LoS-LAS measurement configuration, focusing on ratio thermometry and signal post-processing techniques.

In LAS tomography, the formulation of LAS tomography is explained through uniform discretization of the sensing region and integration of measurements along various projection angles. The section also introduces the ill-posed inverse problem existing in LAS tomography.

Finally, image reconstruction algorithms are reviewed, including iterative methods such as the ART and the modified Landweber algorithm. Additionally, data-driven approaches using deep learning, such as CNN, Swin Transformer, and PINN, are discussed for their potential to enhance reconstruction accuracy by integrating large datasets and physical absorption models.

Chapter 3

Hybrid Model-Driven Spectroscopic Network for Rapid Retrieval of Turbine Exhaust Temperature

3.1 Introduction

In Chapter 1, the importance of effective combustion diagnosis has been demonstrated. As an indicator of the thermal health condition of the GTE, Exhaust Gas Temperature (EGT) is critically important and must be monitored with good temporal resolution [69]. Although TCs have been employed for EGT monitoring, their slow response is inadequate for the assessment of the instantaneous energy conversion process, which strongly relates to the combustion characteristics and controls efficiency of the GTE. As mentioned in Chapter 2, LAS offers non-intrusiveness and much faster responses and thus facilitates timely engine fault diagnosis [70]. Among different LAS techniques, WMS is unique for robust, rapid, accurate and sensitive temperature measurement in harsh environments. Then combined with the excellent temporal response characteristics of photodetectors [71] and associated electronics [72], WMS can be carried out at kHz-level temporal resolution [73], and recently up to 1 MHz [74].

However, the iteration-based spectral fitting process limits the real-time response of WMS in industrial applications to the second or sub-second level, even using modern high-level processors. Therefore, accelerating the WMS signal processing stage is crucial to enable its application for rapid EGT retrieval. As mentioned in section 2.4.2, recent efforts have been made to combine deep learning techniques with WMS signal processing for effective LoS temperature reconstruction. These algorithms can effectively obtain features from experimental absorption spectra to

calculate gas parameters. However, the experimental data used in the datasets were sampled under well-controlled lab conditions, which is greatly different from industrial data.The key differences between lab-controlled experimental data and industrial data are the noise levels and the complexity of the environments in which the data is collected. In a lab-controlled setting, the experimental environment is well-controlled, often with known gas properties and minimal external interference. Consequently, the signals collected are much cleaner, with significantly less noise, making them easier to process and analyse. In contrast, industrial data is collected in a more complex and dynamic environment. Various factors such as fluctuating operational conditions, equipment vibrations, and environmental disturbances introduce substantial noise into the laser signals. This makes signal processing and imaging much more challenging, as the data is often severely contaminated by unpredictable noise sources. In harsh industrial environments, for example, the test cell of a GTE, these algorithms suffer from significant uncertainties in their performance against real-world measurement data, in which unpredictable noise arises from mechanical vibration and optical interference. Moreover, the industrial environment can also make the laser performance, e.g., linearity and wavelength stability, different than that in the lab, and thus make the lab-based neural network no longer effective.

This chapter aims to address the aforementioned limitations by proposing a new hybrid model-driven neural network, named Hybrid Model Driven-WMS (HMD-WMS). The proposed algorithm is evaluated against TC measurements in the retrieval of EGT behind an Auxiliary Power Unit (APU), a GTE that provides energy for purposes other than propulsion on large aircraft. The main novelties of this chapter are:

(1) A new HMD-WMS network is designed for real-time spectra recovery and EGT monitoring. It combines a transformer-based encoder and a CNN-structured decoder. Such an architecture efficiently captures temporal and shape information of the WMS harmonic spectra, de-noises spectral sequences and enables efficient neural network testing.

(2) The developed HMD-WMS, for the first time, integrates both the physical model of absorption spectroscopy and industrially-relevant experimental WMS data. The hybrid model enables strong noise resistance against real-world experimental data.

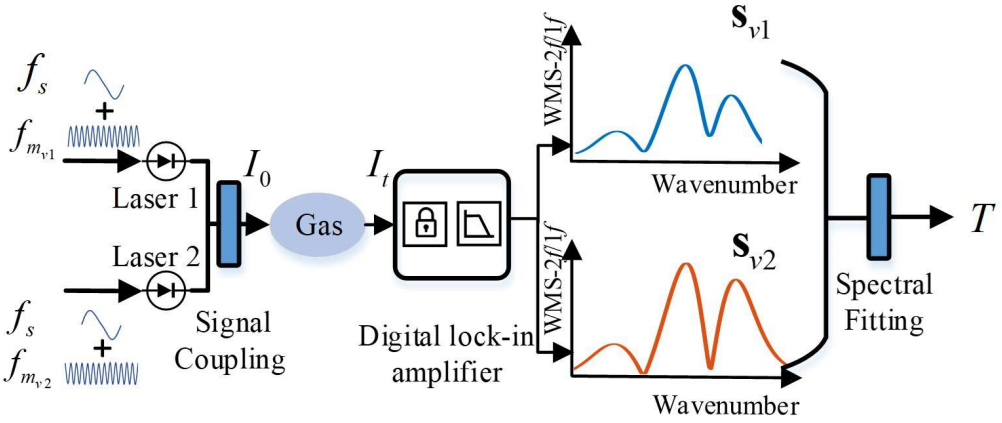

Figure 3.1: Flowchart of WMS measurement and the spectral fitting for temperature retrieval.

(3) An experiment is carried out on an APU under steady-state load to examine the performance of the developed HMD-WMS on retrieving both the spectra and the EGT at 250 Hz. The retrieved spectra fit well with the least-square metric, while the EGT agrees with the TC measurements in its temporal and spatial coverage.

3.2 Methods

3.2.1 Fundamentals

In our case, Frequency Division Multiplexing (FDM) is applied in WMS by simultaneously measuring two absorption transitions of the same chemical species to calculate EGT via ratio thermometry [44].

As shown in Figure 3.1, two lasers at the central wavenumbers of $\bar{\nu}_1$ [cm^{-1}] and $\bar{\nu}_2$ [cm^{-1}] are driven by sinusoidal signals at $f_{m_{v1}}$ [Hz] and $f_{m_{v2}}$ [Hz], respectively, superimposed on a low-frequency carrier at f_s [Hz]. In general, $f_{m_v} \geq 100 \times f_s$, where v is either v_1 or v_2. After penetrating the gaseous medium, the transmitted laser signal

I_t will be demodulated by a digital Lock-In Amplifier and LPF and obtain WMS-$2f/1f$, which has been detailedly described in section 2.3.3. The WMS-$2f/1f$ spectra of the two transitions are saved as two vectors, $\mathbf{s}_{v1} \in \mathbb{R}^{L\times 1}$ and $\mathbf{s}_{v2} \in \mathbb{R}^{L\times 1}$. L is the number of demodulated wavenumber samples of each transition.

Traditionally, T will be retrieved after least-square fitting $\mathbf{s}_{v1}$ and $\mathbf{s}_{v2}$ to the spectroscopic models generated by the HITRAN database. It generally takes a few hundred milliseconds to a few seconds for fitting a single transition even using modern processors, such as those with 2.5 GHz (or higher) base frequency and 8 MB cache. Such computational cost limits the real-time temporal resolution of WMS even if f_s is set at kHz or above. To solve this issue, HMD-WMS is designed in the next subsection to replace the least-square fitting by effectively and rapidly mapping both the temporal and shape features of $\mathbf{s}_{v1}$ and $\mathbf{s}_{v2}$ to T with high accuracy and generalizability.

3.2.2 HMD-WMS Architecture

The architecture of the HMD-WMS is shown in Figure 3.2. It contains four modules, i.e., a data pre-processing module, an encoder, a decoder, and a temperature predictor. Overall, the measured $\mathbf{s}_{v1}, \mathbf{s}_{v2}$ are concatenated as $\mathbf{s} \in \mathbb{R}^{2L\times 1}$, as the input of the data pre-processing module. Then, the pre-processed data go through a transformer-based encoder, followed by a CNN-structured decoder. These three modules aim to recover a de-noised WMS-$2f/1f$ spectral sequence $\mathbf{s}^{\text{rec}} \in \mathbb{R}^{2L\times 1}$, which is physically constrained by the lineshape function. Finally, the temperature predictor maps $\mathbf{s}^{\text{rec}}$ to T via fully-connected layers. The functionalities of these four modules are detailed below.

Data Pre-processing

This module aims to extract data features to maximize the efficiency of the subsequent encoder. Figure 3.3 shows a simulated WMS-$2f/1f$ spectral sequence s of water vapor (H_2O) absorption centred at $\overline{\nu}_1$ = 7185.6 [cm^{-1}] and $\overline{\nu}_2$ = 7444.4 [cm^{-1}]. The primary features of such spectral sequences are manifested as a) the potential temporal correlation between neighboring wavenumber samples arising from time-dependent wavelength scanning; b) the shape features of the whole WMS-$2f/1f$ spectra, such as the temperature-related absorption peaks, broadened lineshape and phase shift [36]. In this module, data embedding and positional encoding are introduced to pre-process $\mathbf{s}$ and then output $\mathbf{P} \in \mathbb{R}^{2L\times d_{\text{emb}}}$ which retains the temporal and shape features. d_{emb} is the embedding dimension.

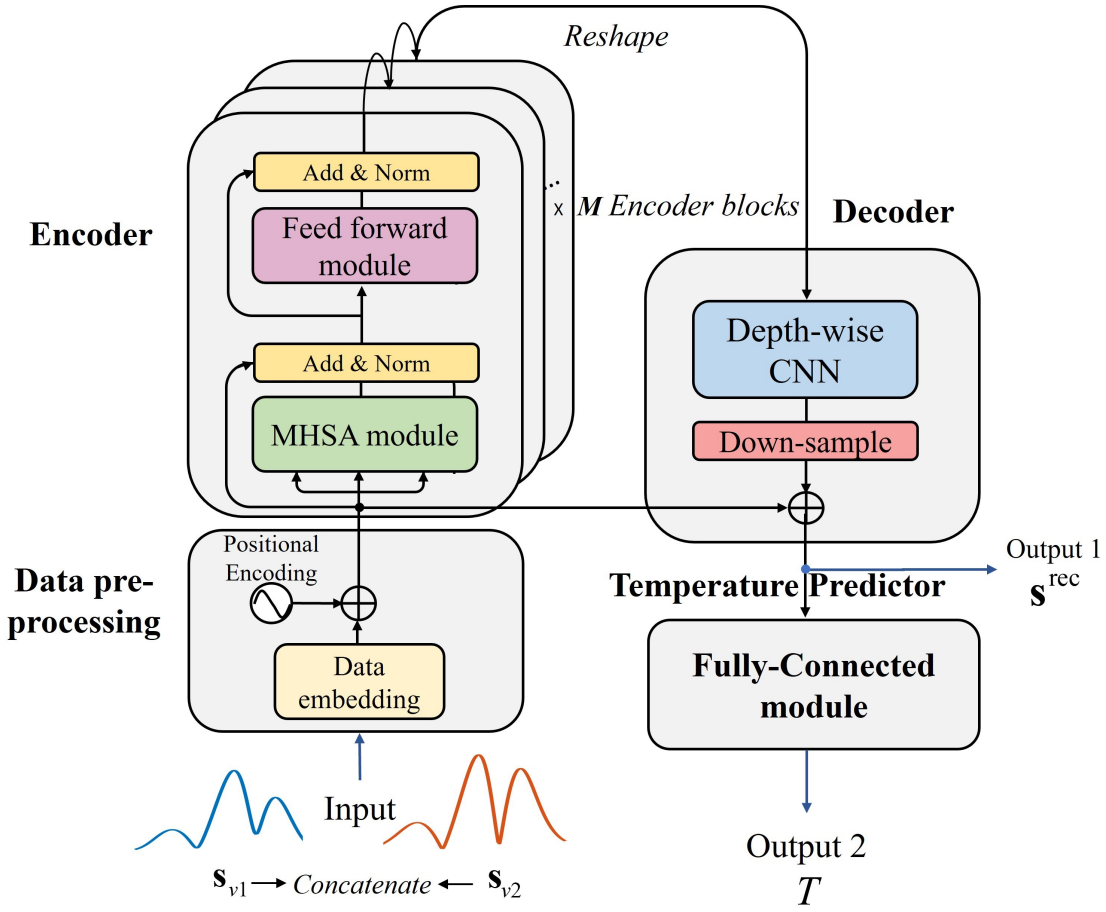

Figure 3.2: Architecture of the proposed HMD-WMS.

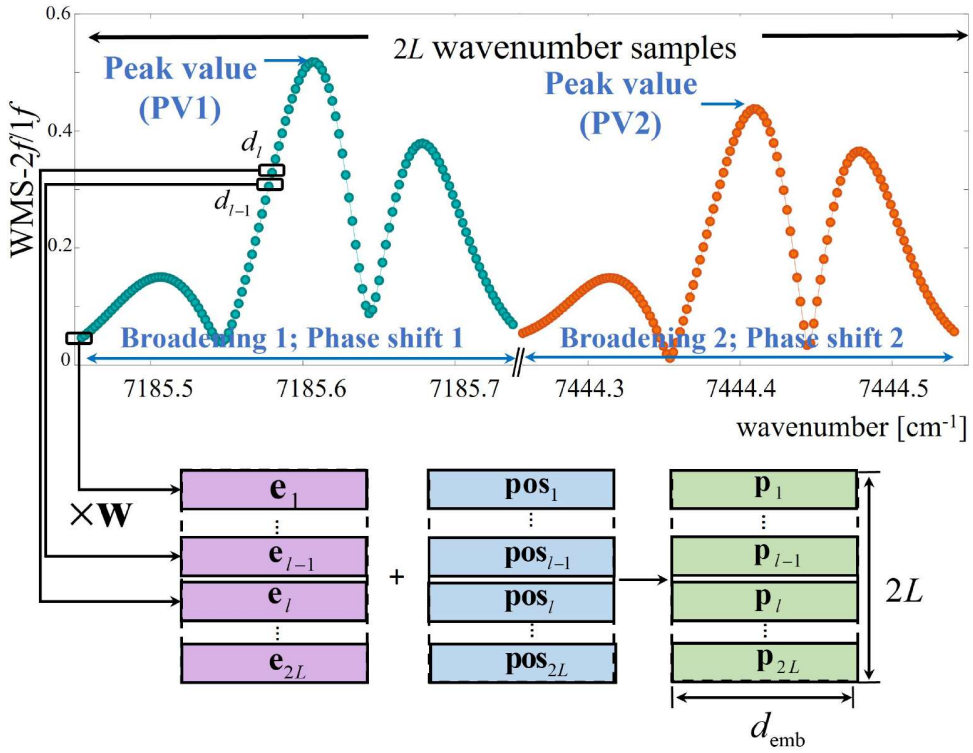

Figure 3.3: Pre-process of concatenated $\mathbf{s}_{v1}, \mathbf{s}_{v2}$ via data embedding and positional encoding.

Data embedding will convert $\mathbf{s}$ to a higher-dimensional matrix. Data embedding has been widely used in Natural Language Processing for converting the categorical variable to a vector of numerical values for semantic meaning representation [75]. In our case, data embedding is mainly used for maintaining the spectral information of each wavenumber sample $\mathbf{s}_l(l = 1,2,...,2L)$ by an embedded vector $\mathbf{e}_l \in \mathbb{R}^{1\times d_{\text{emb}}}$ for the following positional encoding, where $\mathbf{e}_l$ is the l-th row vector of an embedded matrix $\mathbf{E} \in \mathbb{R}^{2L\times d_{\text{emb}}}$. $\mathbf{E}$ is given by:

$$\mathbf{E} = \mathbf{s} \times \mathbf{w} \tag{3.1}$$

where $\mathbf{w} \in \mathbb{R}^{1\times d_{\text{emb}}}$

Positional encoding generates a unique code for the embedded matrix to preserve and enhance its position information [76]. The positional encoding matrix $\mathbf{Pos} \in \mathbb{R}^{2L\times d_{\text{emb}}}$ is obtained for $\mathbf{E}$. The element of the l-th row vector $\mathbf{pos}_l$ can be expressed as:

$$\text{pos}_{l,2j} = \sin \frac{l}{10000^{\frac{2j}{d_{\text{emb}}}}} \tag{3.2}$$

$$\text{pos}_{l,2j+1} = \cos \frac{l}{10000^{\frac{2j}{d_{\text{emb}}}}} \tag{3.3}$$

where $j = 1,2,\ldots,d_{\text{emb}}/2$. d_{emb} is an even number. The use of sinusoidal functions here is due to a) their nature of continuity and differentiability to benefit model training; and b) their reliability of frequency adjustment to generate unique position-involved vectors. Finally, the data pre-processing module will output $\mathbf{P} \in \mathbb{R}^{2L\times d_{\text{emb}}}$:

$$\mathbf{P} = \mathbf{E} + \mathbf{Pos} \tag{3.4}$$

Encoder

A transformer benefitting from its effectiveness on learning long-term dependencies via parallel computation [76], is used in HMD-WMS encoder to capture the temporal features of $\mathbf{P}$. Here, M series of encoder blocks are concatenated, as shown in Figure 3.2, to form an encoder. In each block, there are a Multi-Head Self-Attention (MHSA) sublayer and a feedforward sublayer. The principles of MHSA have been demonstrated in [76]. In our case, the structure of the encoder can be simplified as:

$$\mathbf{O}_{\text{sublayer1}} = \text{LayerNorm}(\mathbf{MHSA}(\mathbf{P}) + \mathbf{P} \tag{3.5}$$

$$\mathbf{O}_{\text{sublayer2}} = \text{LayerNorm}(\sigma(\mathbf{O}_{\text{sublayer2}}\mathbf{W_1} + \mathbf{b_1})\mathbf{W_2} + \mathbf{b_2} + \mathbf{P} \tag{3.6}$$

where $\mathbf{O}_{\text{sublayer1}} \in \mathbb{R}^{2L \times d_{\text{emb}}}$ and $\mathbf{O}_{\text{sublayer2}} \in \mathbb{R}^{2L \times d_{\text{emb}}}$ are the outputs of MHSA and the feedforward sublayer, respectively. $\mathbf{W}_1 \in \mathbb{R}^{d_{\text{emb}} \times d_{\text{ff}}}$ and $\mathbf{W}_2 \in \mathbb{R}^{d_{\text{ff}} \times d_{\text{emb}}}$ represent the trainable weights for the first and the second linear layers within the feedforward sublayer. $\mathbf{b}_1 \in \mathbb{R}^{1 \times d_{\text{ff}}}$ and $\mathbf{b}_2 \in \mathbb{R}^{1 \times d_{\text{emb}}}$ are bias vectors. σ is the ReLU activation function.

Decoder

The decoder consists of a Depth-Wise CNN (DW-CNN) and a residual submodule. It further learns and refines the shape of the WMS-$2f/1f$ spectra to recover the denoised spectra.

Depth-Wise Convolutional Neural Network CNNs are well-suited for discovering intricate shape features of matrices. Here, we choose DW-CNN to prevent crosstalk among different channels by setting the number of kernels as $2L$ to avoid distortion on the extracted temporal information from the sequence. In standard CNNs, each convolutional layer performs convolution across all input channels using a shared set of learnable kernels. In contrast, DW-CNN will employ an individual kernel set for each input channel, i.e., each wavenumber sample in the spectral sequence, thus preserving the existing temporal features among different channels. In our model, DW-CNN is composed of two depth-wise convolutional layers, i.e., Conv1 and Conv2, each followed by a batch normalization layer and an activation function. $\mathbf{O}_{\text{sublayer2}}$ is reshaped to $\mathbf{C} \in \mathbb{R}^{\sqrt{d_{\text{emb}}} \times \sqrt{d_{\text{emb}}} \times 2L}$ as the input. The forward propagation is expressed as:

$$\mathbf{O}_{\text{Conv1}} = \sigma\{\mathbf{BN}(\mathbf{W}_{\text{Conv1}} * \mathbf{C} + \mathbf{b}_{\text{Conv1}})\} \tag{3.7}$$

$$\mathbf{O}_{\text{Conv2}} = \sigma\{\mathbf{BN}(\mathbf{W}_{\text{Conv2}} * \mathbf{O}_{\text{Conv2}} + \mathbf{b}_{\text{Conv2}})\} \tag{3.8}$$

$$\mathbf{O}^{\text{dec}} = \sigma\{\mathbf{FC}(\mathbf{O}_{\text{Conv2}})\} \tag{3.9}$$

where the operator $*$ represents convolution, $\mathbf{BN}$ and $\mathbf{FC}$ the batch normalization and the fully-connected calculation, respectively. $\mathbf{O}_{\text{Conv1}} \in \mathbb{R}^{H_{O1} \times W_{O1} \times C_{O1}}$ ($\mathbf{O}_{\text{Conv2}} \in \mathbb{R}^{H_{O2} \times W_{O2} \times C_{O2}}$) , $\mathbf{W}_{\text{Conv1}} \in \mathbb{R}^{H_{W1} \times W_{W1} \times C_{W1}}$ ($\mathbf{W}_{\text{Conv2}} \in \mathbb{R}^{H_{W2} \times W_{W2} \times C_{W2}}$) and $\mathbf{b}_{\text{Conv1}} \in \mathbb{R}^{1 \times C_{O1}}$ ($\mathbf{b}_{\text{Conv2}} \in \mathbb{R}^{1 \times C_{O2}}$)) are the output maps, convolutional kernels and bias vectors of Conv1 (Conv2), respectively. H_{O1} (H_{O2}), W_{O1} (W_{O2}), are the height and width

of $\mathbf{O}_{\text{Conv1}}$ ($\mathbf{O}_{\text{Conv2}}$), respectively. C_{O1} (C_{O2}) is the number of channels. H_{W1} (H_{W2}), W_{W1} (W_{W2}), and C_{W1} (C_{W2}) are the kernel height, width, and the number of kernels of $\mathbf{W}_{\text{Conv1}}$ and $\mathbf{W}_{\text{Conv2}}$, respectively. $C_{O1} = C_{O2} = C_{W1} = C_{W2} = 2L$. $\mathbf{o}^{\text{dec}} \in \mathbb{R}^{2L\times 1}$ is the reconstructed feature vector from the DW-CNN module.

Residual Module This module tackles the issues of vanishing gradient and degradation in accuracy via short-cut connections when the depth of the neural network increases [77]. Here, the input $\mathbf{s}$ will shortcut to the output of DW-CNN, $\mathbf{o}^{\text{dec}}$, for residual mapping. The output of the residual module is defined as:

$$\mathbf{s}^{\text{rec}} = \sigma\{\mathbf{o}^{\text{dec}} + \mathbf{s}\} \tag{3.10}$$

where $\mathbf{s}^{\text{rec}} \in \mathbb{R}^{2L\times 1}$ is the reconstructed WMS-$2f/1f$ spectral sequence, '+' the operand of element-wise addition.

Temperature Predictor

The Temperature Predictor retrieves the mean path temperature T^{rec} based on $\mathbf{s}^{\text{rec}}$. The dependence of $\mathbf{s}^{\text{rec}}$ on T^{rec} can be represented by the following mapping:

$$\mathbf{s}^{\text{rec}} = g(\mathbf{T}^{\text{rec}}) \tag{3.11}$$

We construct three fully-connected layers TP1, TP2 and TP3 to train this mapping. Finally, T^{rec} can be expressed as:

$$T^{\text{rec}} = \tanh\{\mathbf{W}_{\text{TP3}}\{\sigma(\mathbf{W}_{\text{TP2}}\{\sigma(\mathbf{W}_{\text{TP1}}\mathbf{s}^{\text{rec}} + \mathbf{b}_{\text{TP1}})\} + \mathbf{b}_{\text{TP2}}\} + b_{\text{TP3}}\} \tag{3.12}$$

where $\mathbf{W}_{\text{TP1}} \in \mathbb{R}^{d_{\text{emb}}\times 2L}$, $\mathbf{W}_{\text{TP2}} \in \mathbb{R}^{d_{\text{TP2}}\times d_{\text{TP1}}}$ and $\mathbf{W}_{\text{TP3}} \in \mathbb{R}^{1\times d_{\text{TP2}}}$are the trainable weights for the first, second and third layers, respectively, $\mathbf{b}_{\text{TP1}} \in \mathbb{R}^{1\times d_{\text{TP1}}}$, $\mathbf{b}_{\text{TP2}} \in \mathbb{R}^{1\times d_{\text{TP2}}}$ and b_{TP3} are the bias of each layer, and 'tanh' is the activation function Tanh. Since $\mathbf{s}^{\text{rec}}$ is noise-free, T^{rec} retrieval using $\mathbf{s}^{\text{rec}}$ gives more stable results compared to those obtained from the noise-contaminated raw $\mathbf{s}$.

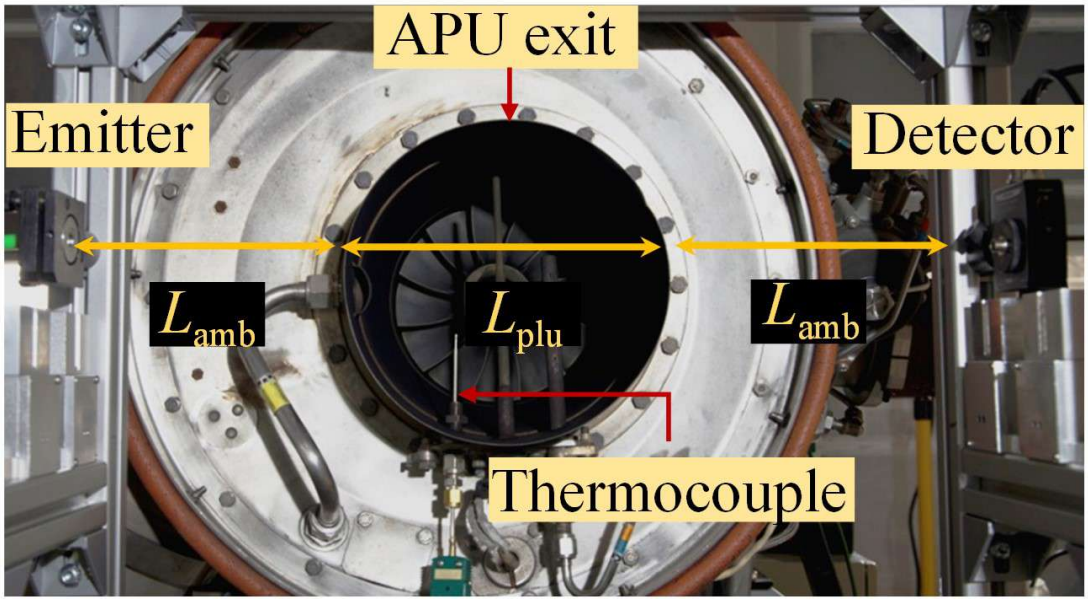

Figure 3.4: Auxiliary Power Unit and laser system setup.

3.3 Experiment and Results

3.3.1 Experiment Setup

To assess the performance of the proposed HMD-WMS method, an industrial-scale experiment was carried out by measuring the EGT of an aircraft APU (Honeywell, Model: GTCP85-129) mounted in a test cell at the University of Sheffield, UK. Figure 3.4 shows the APU exit, laser sensors and the layout of the optical path. In this experiment, we selected H_2O as the target gas species, as it is a common combustion product and has rich absorption spectra in the near-infrared. Here, H_2O transitions at $\bar{\nu}_1$ = 7185.6 [cm^{-1}] and $\bar{\nu}_2$ = 7444.4 [cm^{-1}] are used for ratio thermometry due to their good sensitivity in the target temperature range [78]. The two FDM laser diodes at $\bar{\nu}_1$ (NTT, NLK1E5GAAA) and $\bar{\nu}_2$ (NTT, NLK1B5EAAA) were both scanned at f_s =1 kHz, and modulated at $f_{m_{v1}}$ = 100 kHz and $f_{m_{v2}}$=130 kHz, respectively. The transmitted laser signal was received by a photodetector (Hamamatsu, G12182-110K) and then digitized by a customized Data Acquisition (DAQ) system [72] at f_{samp} = 15.625 Mega samples/second. The Digital Lock-In Amplifier and LPF are integrated into the DAQ system. It utilizes a Cascaded Integrator-Comb (CIC) filter [79; 80] to

down-sample the raw transmission signals with a decimator of c= 32. As a result, each of the $1f$ and $2f$ signals for each transition has N_{samp} = 488 wavenumber samples, where $N_{samp} = f_{samp}/(f_s \cdot c)$. Here, we use the central 120 wavenumber samples for each absorption transition, i.e., L = 120, that adequately cover all the features of the absorption spectra as the input to the HMD-WMS, i.e., $\mathbf{s}_{v1} \in \mathbb{R}^{120\times1}$, $\mathbf{s}_{v2} \in \mathbb{R}^{120\times1}$. The total laser path length Labs is 50 cm, whereas the estimated path length L_{plu} through the APU exhaust plume is 24 cm. To enable the operation of the optics under ambient conditions, both the laser emitter and detector are located at a distance along the radius of 13 cm (denoted L_{amb}) outside the edge of the APU exit (Figure 3.4). In the downstream direction, the laser beam path is positioned 3 cm from the APU exit. For line-of-sight WMS measurement, ratio thermometry retrieves mean path temperature $\overline{T} = f(A_{v1,\text{abs}}, A_{v2,\text{abs}})$, where $A_{v,\text{abs}} = P \cdot S_v(\overline{T}) \cdot \overline{X} \cdot L_{\text{abs}}$ is the integrated absorption from the transition v and $f(\cdot)$ represents the mapping between the integrated absorption of the two transitions and the temperature. Transmitted laser signals were also collected when the APU was not in operation in order to calculate the ambient temperature T_{amb} and H_2O concentration X_{amb} via the traditional fitting method. Then, the integrated absorption along the ambient path length Lamb is calculated as $A_{v,\text{amb}} = P \cdot S_v \cdot T_{\text{amb}} \cdot X_{\text{amb}} \cdot L_{\text{amb}}$, leaving that in the plume as $A_{v,\text{plu}} = A_{v,\text{abs}} - 2 \times A_{v,\text{amb}}$. Finally, the EGT is calculated by $T_{\text{plu}} = f(A_{v1,\text{plu}}, A_{v2,\text{plu}})$. As the standard instrument on the APU, a Class 2 K-type TC (IEC 60584-2, OMEGA Engineering Ltd, UK) was used to record T_{plu}. As demonstrated in [19], the plume temperature is nearly uniform and consistent with the TC measurement. Therefore, the TC-measured T_{plu} can be regarded as a reference for the mean path temperature measurement.

3.3.2 Dataset Construction

As shown in Figure 3.5, a hybrid dataset was built by combining both simulated data and a small portion of experimental data. Among different APU working conditions, the measured temperature range by TC was from 400 K to 880 K, whereas the mole fraction measured by a gas sampler was 0.00052 to 0.02. To improve the diversity of training samples, we generated a simulated training dataset utilizing the HITRAN database, allowing simulated average temperature and H_2O concentration to cover the above range with the step size of 4 K for temperature and 0.0002 for H_2O mole fraction. As a result, 14400 simulated WMS-$2f/1f$ spectral sequences $\mathbf{s}_m^{\text{sim}} = \{\mathbf{s}_{v1,m}^{\text{sim}}, \mathbf{s}_{v2,m}^{\text{sim}}\} \in \mathbb{R}^{240\times1} (m = 1, 2, \ldots, 14400)$, were generated. To further im-

prove noise robustness, 20 dB, 30 dB and 40 dB white noises (the reasonable noise levels in real experiments [17]) were added to $\mathbf{s}_m^{\text{sim}}$, resulting in 57600 noise-contaminated simulated spectra $\mathbf{s}_m^{\text{sim}}$. Each $\mathbf{s}_m^{\text{sim}}$ spectrum is associated with its corresponding reconstruction $\mathbf{s}_m^{\text{rec,sim}}$, i.e., the output of the decoder, and with the ground-truth temperature T_m^{sim}, to be a simulated training sample.

For the experimental training dataset, we randomly selected 100 measured spectra for each absorption feature when the APU was working at steady-state, noted as $\mathbf{s}_n^{\text{exp}} = \{\mathbf{s}_{v1,n}^{\text{exp}}, \mathbf{s}_{v2,n}^{\text{exp}}\} \in \mathbb{R}^{240\times 1}(m = 1, 2, \ldots, 100)$. The traditional least-squares fitting method is used to obtain a de-noised spectral sequence $\mathbf{s}_n^{\text{rec,exp}}$ and thus retrieve T_n^{exp}. The combination of $\mathbf{s}_n^{\text{exp}}$, $\mathbf{s}_n^{\text{rec,exp}}$ and T_n^{exp} are regarded as the experimental training samples. Therefore, there are $\mathscr{N}_{\text{train}}$ training samples in total, denoted as $((\mathbf{s}_n^{\text{sim}}, \mathbf{s}_n^{\text{exp}}), (\mathbf{s}_m^{\text{rec,sim}}, \mathbf{s}_n^{\text{rec,exp}}), (T_m^{\text{sim}}, T_n^{\text{exp}})), \mathscr{N}_{\text{train}} = 57700.$

This hybrid training set plays a crucial role on the robustness and accuracy of our model. Specifically, the simulated data provides a broad and comprehensive foundation by covering a wide range of gas conditions, including different temperatures and concentrations. This variety allows the neural networks to learn spectral features across diverse scenarios, enhancing their ability to generalize to new conditions. On the other hand, the experimental data contributes by introducing real-world complexities such as unpredicted noise, vibrations, and other environmental factors that are difficult to model in simulations. This real-world variability is essential for stabilizing the model's performance in practical applications, particularly in temperature prediction. The experimental data improves the model's noise robustness.

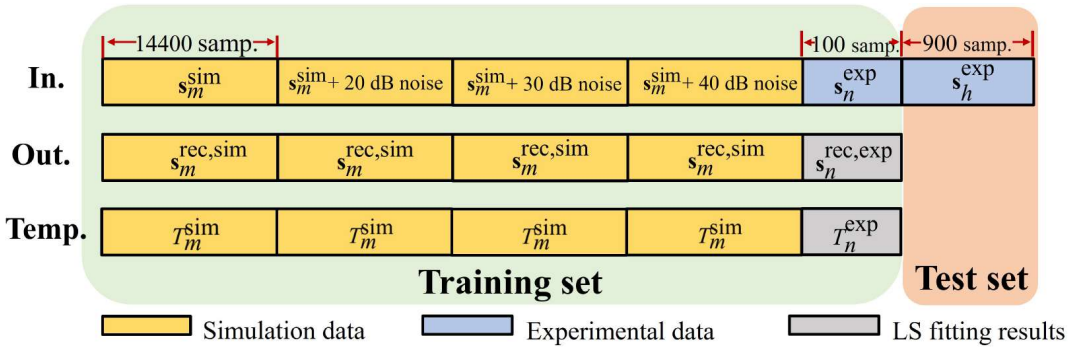

Figure 3.5: Construction of the training set and the test set.

Using the above training dataset, Empirical Risk Minimization (ERM) and Structural Risk Minimization (SRM) are deployed on the HMD-WMS for model training. Specifically, ERM is applied to minimize the weighted Mean Square Error (MSE) loss in terms of the reconstructed spectral sequence and temperature, whereas SRM is used to avoid overfitting. Given the training dataset with a batch size of B, the total loss function $L_{\text{tot\_loss}}$ is defined as:

$$L_{\text{tot\_loss}} = \varepsilon \times \frac{1}{B}\sum_{b=1}^{B}(\widehat{s_b^{\text{rec}}} - s_b^{\text{tru}})^2 + (1-\varepsilon) \times \frac{1}{B}\sum_{b=1}^{B}(\widehat{T_b^{\text{tru}}} - T_b^{\text{tru}})^2 + \lambda_B \|\psi\|_2^2 \quad (3.13)$$

where ε is the hyperparameter to trade off MSE loss between the b-th reconstructed spectral sequence $\widehat{\mathbf{s}_b^{\text{rec}}}$ and temperature $\widehat{T_b^{\text{rec}}}$, $\mathbf{s}_b^{\text{tru}} \in (\mathbf{s}_m^{\text{rec,sim}}, \mathbf{s}_n^{\text{rec,exp}})$ and $T_b^{\text{tru}} \in (T_m^{\text{sim}}, T_n^{\text{exp}})$ are the corresponding ground-truth values, λ_B is the penalty parameter for $L2$ regularization $||\cdot||_2^2$. ψ is the set of trainable weights. The other hyper-parameters in HMD-WMS are shown in Table 3.1.

Table 3.1: Hyper-parameters of HMD-WMS

Encoder		**Decoder**			
d_{emb}	64		Conv1	Conv2	FC
Θ	8	Input dim.	8 × 8 × 240	5× 5× 240	240× 4
M	4	Weight matrix size	4× 4	4×4	4×1
d_{ff}	128	Stride	(1,1)	(1,1)	-
d_Q, d_K, d_V	8	Output dim.	5× 5× 240	2× 2× 240	240× 1
Temperature Predictor					
		TP1	TP2	TP3	
Input dim.		240	128	32	
Weight matrix size		240× 128	128× 32	32× 1	
Output dim.		128	32	1	

The ablation study is carried out when designing the HMD-WMS to examine the robustness of the proposed network architecture. To further assess the HMD-WMS, the traditional fitting method and the TC measurement are regarded as benchmarks. The results obtained by the HMD-WMS are compared to the benchmarks, and to two other state-of-the-art data-driven methods that utilize the same dataset and are pre-processed in the same way. The details of the three alternative methods are given below:

- Traditional fitting method [48]: a least-squares fit to the measured WMS-$2f/1f$ spectra is carried out using gas parameters in the HITRAN database, i.e., Doppler/Collision broadening, line strength, etc. to calculate the integrated absorption for each transition. The mean path temperature is retrieved using ratio thermometry.
- Adaptively Optimized Gas Analysis Model (AOGAM) [51]: attention-aided long short-term memory (LSTM) algorithm is used as its framework to reconstruct gas parameters via absorption spectroscopy. Here, WMS-$2f/1f$ spectra are input to the AOGAM and flow through the same data pre-processing module, an attention-aided LSTM-structured encoder and decoder to retrieve the denoised spectral sequence and thus the temperature.
- Convolutional autoencoder (ConV-AE): this method is widely recognized in the field of absorption spectroscopy, i.e., Y-Net [64]. Another reason to use this framework for temperature retrieval is to compare the pure ConV-AE to the HMD-WMS. Here, the WMS-2f/1f spectra are fed into a DW-CNN for retrieval.

All the data-driven models were trained using PyTorch on a single GPU of NVIDIA A100-SXM4-40GB and deployed Adam [81] for optimization with a learning rate of 2×10^{-3}, ε = 0.5, B = 32, $\lambda_B = 2 \times 10^{-6}$. Epoch is 50.

3.4 Experimental Validation

When the APU worked at steady-state, 900 $\mathbf{s}_h^{\mathrm{exp}}(h = 1, 2, \ldots, 900)$ were measured for testing, i.e., $\mathscr{N}_{\mathrm{test}}$ = 900). To accelerate the convergence of the model, ($\mathbf{s}_n^{\mathrm{sim}}$, $\mathbf{s}_n^{\mathrm{exp}}$) and ($\mathbf{s}_m^{\mathrm{rec,sim}}$, $\mathbf{s}_m^{\mathrm{rec,exp}}$) are standardized, whereas the temperature is rescaled within the range of (0,1) using the low temperature T_{low} of 300 K and the high temperature T_{high} of 900 K. To examine the proposed HMD-WMS's learning trajectory and its adaptability, Figure 3.6 (a) shows both training loss and validation loss for temperature prediction and (b) for spectra retrieval in the training process. It can be seen that

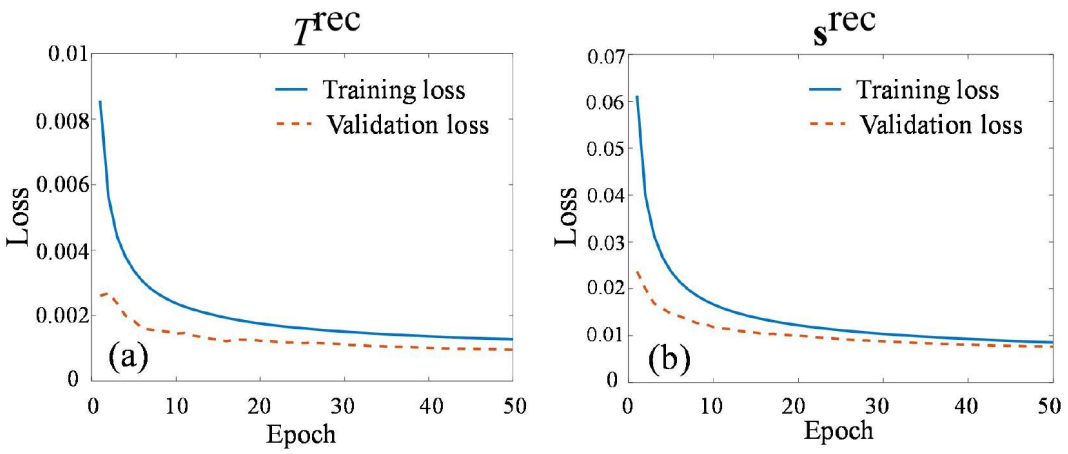

Figure 3.6: Training loss and validation loss for (a) temperature prediction and (b) WMS-$2f/1f$ spectra retrieval.

the optimization of the HMD-WMS in both cases converges rapidly and steadily. The three data-driven models HMD-WMS, AOGAM and ConV-AE are tested by comparing their outputs in terms of $\mathbf{s}^{\text{rec}}$ and $T_{\text{plu}}^{\text{rec}}$ against values obtained by the traditional least-squares fitting procedure and the TC data. $T_{\text{plu}}^{\text{rec}}$ represents the retrieved plume temperature.

Evaluation of $\mathbf{s}^{\text{rec}}$

Figure 3.7 shows one example of the reconstructed WMS-$2f/1f$ spectra (at $\bar{\nu}_1$ and $\bar{\nu}_2$) $\mathbf{s}_h^{\text{rec}}$ (h = 900) measured behind the APU, obtained by deploying the least-squares spectral fitting method, i.e. the benchmark method, and shown as the solid curve in each of Figure 3.7 (a), (b), (c); those obtained by the three different data-driven algorithms are given in Figure 3.7 (a), (b), and (c) and compared separately against the benchmark.

It can be seen that $\mathbf{s}_h^{\text{rec}}$ retrieved using the proposed HMD-WMS in Figure 3.7 (a) best fits the benchmark. $\mathbf{s}_h^{\text{rec}}$ retrieved by AOGAM in Figure 3.7 (b) is smooth but deviates significantly from the fitting result around the peak of the absorbance. The retrieval using ConV-AE in Figure 3.7 (c) is similarly close to the benchmark at the wavenumber around 7185.59 cm^{-1}, in comparison to that using the HMD-WMS. However, ConV-AE results in a much larger residual to the benchmark at the wavenumber around

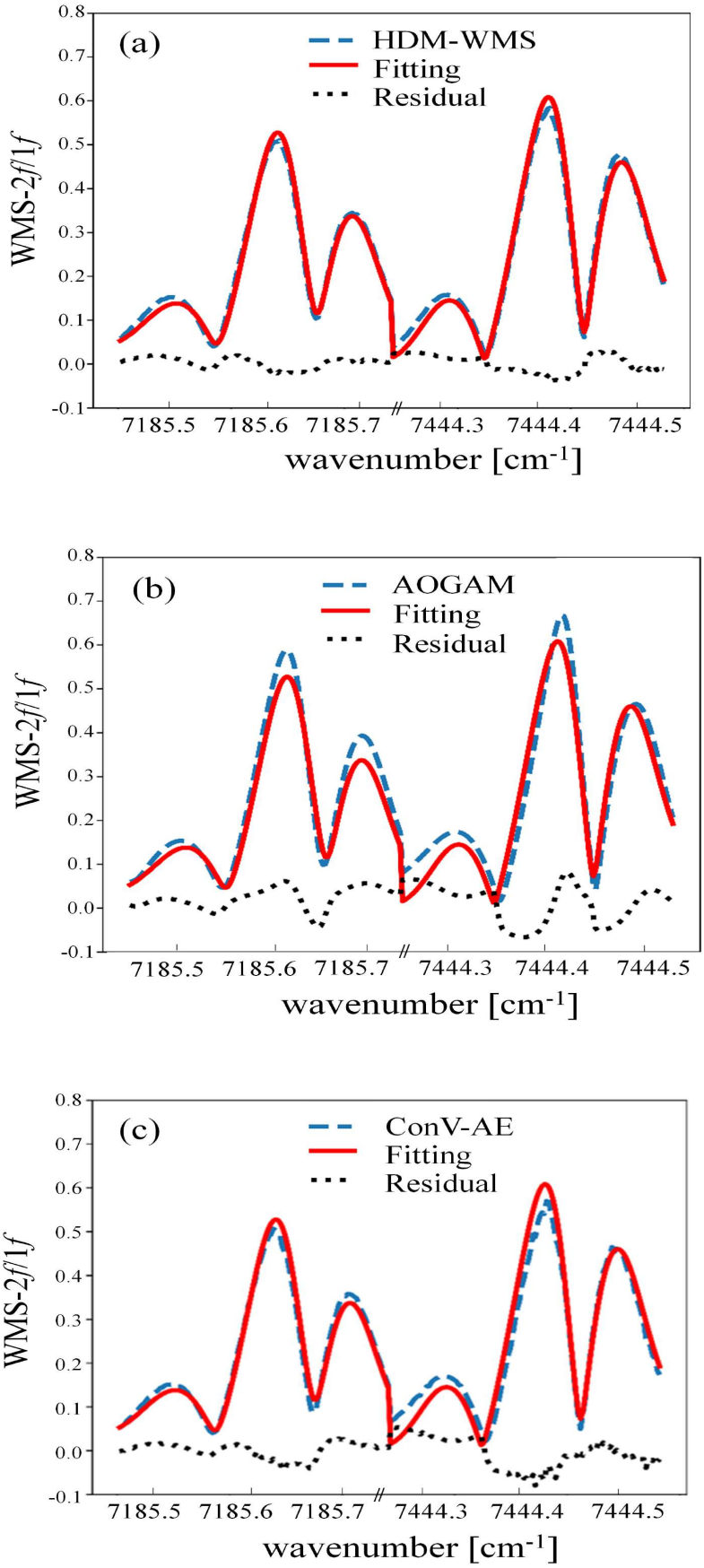

Figure 3.7: Comparison of the reconstructed WMS-$2f/1f$ spectra using (a) HMD-WMS (b) AOGAM and (c) ConV-AE to the benchmark obtained from the traditional least-squares spectral fitting method.

7444.3 cm^{-1}. Furthermore, the Euclidean norms of the residual for HMD-WMS, AOGAM and ConV-AE are 0.2647, 0.6211 and 0.4485, respectively. This confirms that HMD-WMS gives the best accuracy when compared to the other two deep learning models.

Furthermore, the performance on $\mathbf{s}_h^{\text{rec}}$ retrieval for the whole experimental test set (i.e., 900 pairs of spectra) is analyzed statistically. We used Curve Error (CE), Correlation Coefficient (CC) and Peak Values (PVs) as metrics to evaluate the models' performance. CE is defined as:

$$\text{CE} = \frac{1}{\mathscr{N}_{\text{test}}} \sum_{h=1}^{\mathscr{N}_{\text{test}}} \frac{\left\| \mathbf{s}_h^{\text{rec}} - \mathbf{s}_h^{\text{tru}} \right\|_2}{\left\| \mathbf{s}_h^{\text{tru}} \right\|_2} \tag{3.14}$$

where $\mathbf{s}_h^{\text{tru}}$ is the vector of WMS-$2f/1f$ spectra recovered using the spectral fitting method. As shown in Table 3.2, the CE of the HMD-WMS is 0.0464, approximately ¼ of AOGAM and ½ of ConV-AE. CC represents the similarity between $\mathbf{s}^{\text{rec}}$ retrieved using the deep learning models and the benchmark. Although CCs obtained from different models are all higher than 0.96, HMD-WMS gives the highest, at 0.9971. The 0.01-0.03 higher CC compared to the AOGAM and ConV-AE is reflected by the improved accuracy on the absorption peaks and the smoothness of the curve. PV mainly represents the local characteristics at the absorption peak of the two WMS-$2f/1f$ spectra. The two peak values around $\bar{v}_1$ and $\bar{v}_2$ on $\mathbf{s}^{\text{rec}}$ are named PV1 and PV2, respectively (shown in Figure 3.3). Both PV1 and PV2 obtained using HMD-WMS are closest to the result given by the benchmark. Therefore, it can be quantitatively and statistically concluded that HMD-WMS outperforms the other two state-of-the-art models for reconstructing the WMS-$2f/1f$ spectra with better accuracy.

Table 3.2: Performance of HMD-WMS, AOGAM and ConV-AE on WMS-$2f/1f$ retrieval and their comparisons to the spectral fitting method

Method \ Matrix		Fitting	HMD-WMS	AOGAM	ConV-AE
$\mathbf{s}^{\mathrm{rec}}$	CE	–	0.0464	0.1613	0.0968
	CC	–	0.9971	0.9685	0.9871
	PV1	0.608	0.582	0.6450	0.540
	PV2	0.528	0.507	0.589	0.504

3.4.1 Evaluation of $T_{\mathrm{plu}}^{\mathrm{rec}}$

Figure 3.8 shows the comparison of the reconstructed EGT in the plume $T_{\mathrm{plu}}^{\mathrm{rec}}$ during the 900 ms data collection period. The least-squares fitting method, HMD-WMS and ConV-AE show a similar extent of short-term temperature fluctuation, while AOGAM suffers from much stronger fluctuations. Regarding the TC measurement as the benchmark in this comparison, a moving average with a window length of 10 on 900 test samples is imposed on the raw $T_{\mathrm{plu}}^{\mathrm{rec}}$ to clearly visualize the offset between the reconstructed temperature and the TC measurement. It can be observed that HMD-WMS gives the smallest offset. To quantitatively evaluate the offset between the least-squares fitting method (the benchmark) and the deep learning algorithmms, the Bland-Altman plot is shown in Figure 3.9. $\mathrm{M_{HW}}$,$\mathrm{M_{CV}}$ and $\mathrm{M_{AG}}$ represent the means of temperature offsets for the 900 test samples between the traditional fitting method and HMD-WMS, ConV-AE and AOGAM, respectively. $\mathrm{SD_{HW}}$, $\mathrm{SD_{CV}}$ and $\mathrm{SD_{AG}}$ are the corresponding standard deviations of the offsets. As shown in Figure 3.9, MHW is 2.25 K, which is the smallest compared to those obtained using AOGAM (65.97 K) and ConV-AE (26.48 K). In addition, the results from the HMD-WMS exhibit the narrowest variation and are closest to zero, falling within the range of ±1.96 $\mathrm{SD_{HW}}$. Therefore, it can be concluded that HMD-WMS gives the best accuracy on EGT retrieval, among the three deep learning methods.

Table 3.3 shows a statistical comparison among the different methods using the same test set. Here, the mean value of the 900 measurements is used to assess the accuracy of each algorithm and the Standard Deviation (STD) allows examination of their robustness against measurement noise. The Standard Error (SE) of the mean value is used to compare accuracy among all the TDLAS algorithms. Although the APU was working at steady-state, a high-speed plume passing through the laser

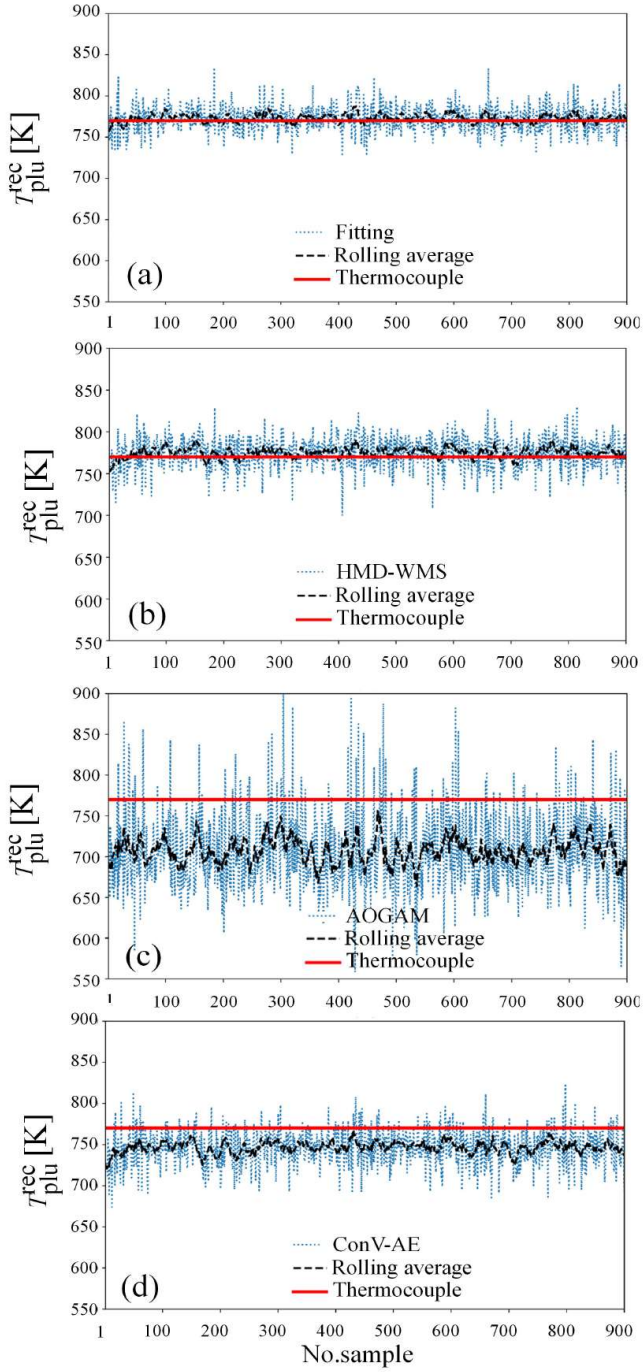

Figure 3.8: Performance of HMD-WMS, AOGAM and ConV-AE on WMS-$2f/1f$ retrieval and their comparisons to the spectral fitting method

beam can cause beam steering and thus distortion on the measurement, so there is likely to be some contribution to the STD from variability in the measured gas sample. In addition, the tolerance of the TC is 0.75%, resulting in ±5.8 K potential offset of the EGT, as measured by the TC, from the true value.

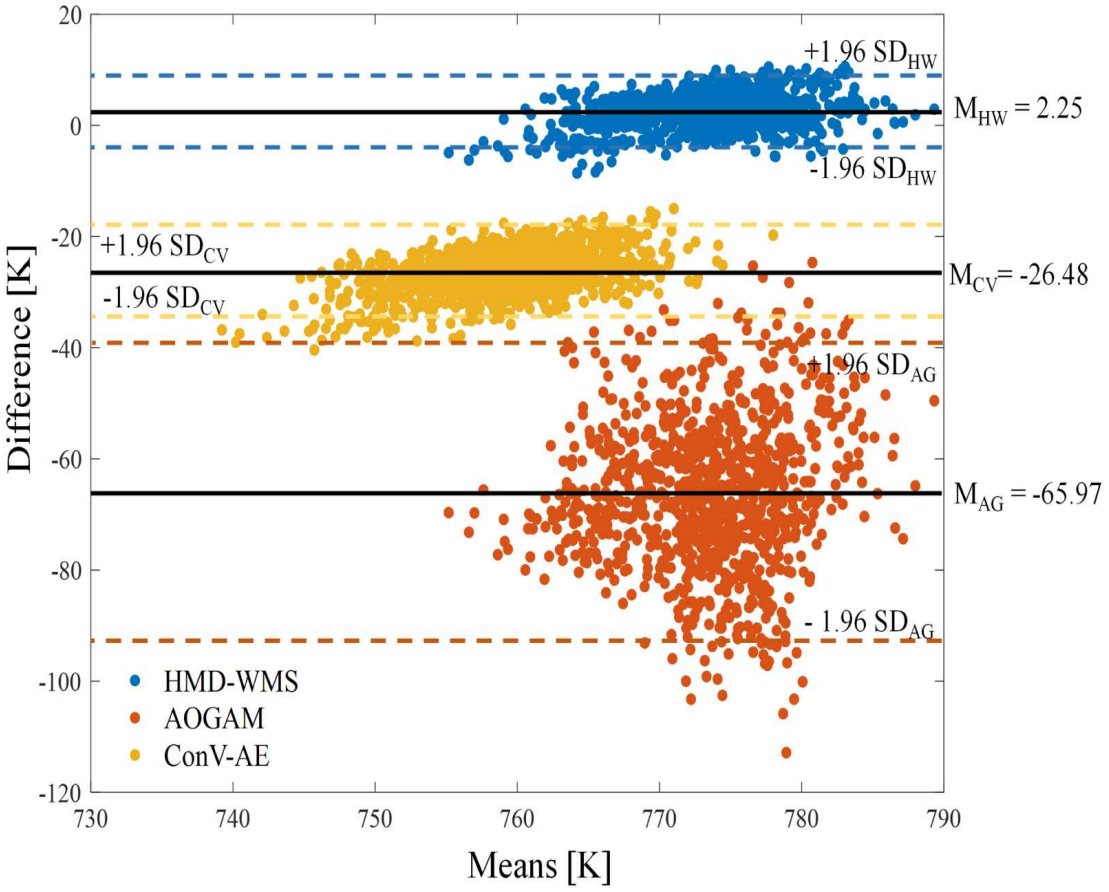

Figure 3.9: The Bland-Altman plot to evaluate $T_{\text{plu}}^{\text{rec}}$ from HMD-WMS, AOGAM and ConV-AE in comparison to the benchmark: least-squares fitting method.

Furthermore, Table 3.3 also shows that both the traditional fitting method and the proposed HMD-WMS algorithm recover values of EGT that are consistent with that measured by the TC, and they have very similar dispersion among their individual measured values, as indicated by their STD values, which are both small, yielding small SE. Adding the two SE values in quadrature indicates that the apparent discrepancy between the two mean values, 2.27 K, is not statistically significant, hence their relative performance in recovering EGT is indistinguishable. Both AOGAM and ConV-AE fail to yield EGT values that are consistent with the TC result or with the traditional fitting method, even after consideration of the larger dispersion that they both display in their individual measured values.

Table 3.3: Mean, STD and SE of retrieved EGT for the test set using the spectal fitting, HMD-WMS, AOGAM and ConV-AE, and their comparison to the TC measurement

Matrix / Method	TC	Performance			
		Fitting	HMD-WMS	AOGAM	ConV-AE
Mean (K)	775(±5.8)	772.32	774.59	706.36	745.82
STD (K)	–	15.5	18.45	48.39	22
SE (K)	–	0.52	0.62	1.61	0.73

3.4.2 Evaluation of computational cost

Table 3.4 shows the computational inference time for processing the 900 test samples, the number of trainable parameters and Giga Floating-Point Operations per Second (GFLOPs) of these different algorithms. Least-squares fitting takes around 4.23 s for each spectra, resulting in a total of 3807 s for the whole test set, on a computer with the processor Intel(R) Core (TM) i7-6700 CPU @ 3.40GHz. In contrast, all the deep learning algorithms take less than 0.25 s for processing 900 spectral pair samples, i.e., less than 0.3 ms per sample. Although HMD-WMS gives higher GFLOPs, its inference time is shorter than AOGAM. This is benefitted from parallel computation of transformer in HMD-WMS. Once the data-driven model is trained, such inference time enables real-time EGT measurement at kHz temporal resolution or better. Besides, HMD-WMS has comparable trainable parameters with AOGAM, whereas ConV-AE has nearly three times more. Although ConV-AE achieves the shortest processing time, it has the worst estimation accuracy. Therefore, HMD-WMS is the best performer among all four methods presented here.

Table 3.4: Comparison on the computational complexity for the test set using the spectral fitting, HMD-WMS, AOGAM and ConV-AE

Method	Fitting	HMD-WMS	AOGAM	ConV-AE
Time elapsed (second)	4.23×900	0.104	0.233	0.016
No. parameters	–	78,575	68,642	2,128,243
GFLOPs	–	1.77	0.04	0.7

3.5 Summary

In this chapter, a hybrid model-driven WMS, named HMD-WMS, is proposed to enable accurate and rapid monitoring of the EGT of gas turbines. The model is constructed by the combination of data pre-processing, encoder, decoder and temperature predictor. To improve the fidelity of temperature retrieval, the underlying physical absorption spectroscopic model is introduced into the deep learning model and a hybrid dataset is built by including data from both simulation and experiment.

The proposed HMD-WMS is experimentally assessed by retrieving the EGT of an aircraft APU working at steady-state load. In comparison to the other two state-of-the-art deep learning models considered here, i.e., AOGAM and ConV-AE, HMD-WMS improves the accuracy in the reconstructed spectral sequence by 25%-50% under practical noise levels ranging from 20 dB to 40 dB. The new HMD-WMS method yields EGT values that are consistent with TC measurements and with the traditional least-squares fitting method, whereas AOGAM and ConV-AE fail in terms of the error on EGT estimation. The inference time of HMD-WMS for testing 900 samples is 0.104 s, enabling EGT retrieval above the kHz rate, with the potential for real-time gas turbine diagnosis.

Based on the research of this chapter, one journal paper and one conference paper have been published:

- **Y. Fu**, R. Zhang, J. Xia, A. Gough, S. Clark, A. Upadhyay, G. Enemali, I. Armstrong, I. Ahmed, M. Pourkashanian, P. Wright, K. Ozanyan, M. Lengden, W. Johnstone, N. Polydorides, H. McCann, C. Liu, "Hybrid model-driven spectroscopic network for rapid retrieval of turbine exhaust temperature," *IEEE Transactions on Instrumentation and Measurement*, doi: 10.1109/TIM.2023.3328086.

- **Y. Fu**, C. Liu, R. Zhang, G. Enemali, J. Xia, H. McCann, A. Upadhyay, I. Armstrong, A. Gough, M. Lengden, and W. Johnsone, " Deep learning-aided wavelength modulation spectroscopy for rapid temperature measurement,"*7th Field Laser Applications in Industry and Research (FLAIR)*, Aix-les-Bains, France, 2022.

Chapter 4

Convolutional Neural Network Aided LAS Tomography for Dynamic Temperature Imaging

4.1 Introduction

By solving the inversion of the line-of-sight and sparsely-resolved LAS measurements, LAS tomography has been developed as a powerful tool to quantitatively image the 2D cross-sessional distributions of gas parameters, such as temperature [14], gas species concentrations [82], pressure [83] and velocity [84]. Concerning the influence of each parameter, effective inspection on the temperature is of significance as it strongly relates to the combustion process and directly determines gas composition within the combustion field. It will be helpful and meaningful in the aspect of improving combustion efficiency, energy conservation, and environmental protection [21]. Therefore, a growing number of researchers focus on exploring temperature imaging with high accuracy and reliability.

As mentioned in section 2.6.2, limited by the insufficient number of line-of-sight measurements, tomographic data inversion is inherently ill-posed and rank-deficient [55], which causes less accuracy and increased instability in the reconstructed images. Although various computational tomographic algorithms impose determined *a priori* for regularization [22; 85; 86], it is still challenging to eliminate the effects of artefacts. Instead of highly depending on the mathematical formulation, the deep learning technique provides an alternative approach to solving these ill-posed inverse problems. Regarding laser absorption information as the input and the corresponding

temperature imaging as the output, a deep learning-based model is trained to obtain the implicit functional relationship among input-output pairs [87]. By updating a large number of weights each iteration, better flexibility is introduced in the training process to suppress the effects caused by rank deficiency.

CNN, as one of the most powerful neural networks to detect the intricate property of images with high sensitivity, has been applied to LAS tomography for reactive field prediction [88; 89; 63; 62]. However, although these innovative algorithms have been confirmed by both numerical simulation and lab-scale experiments, most of them are only available to reconstruct static, separated simple temperature distributions. In supervised learning, the quality of the training set is crucial in determining model performance. In combustion fields, where complex heat transfer and reactions among various gas species occur, simple training samples are not capable of representing real-world scenarios. Consequently, the application of these algorithms on an industrial scale is significantly limited.

In this chapter, we present two simulation studies: (1) a multiple Gaussian distribution model simulating an annular combustor with ten injectors, and (2) a CFD model simulating a circular burner. These models can describe flames in complex geometries and incorporate a wide variety of physical phenomena [90] in the training set. The proposed neural network is trained to extract characteristics of dynamic temperature distributions and capture the end-to-end relationship between projected absorption and temperature imaging. Additionally, to obtain densely spatial samples, a tomographic sensor system with 128 laser beams from four equiangular views is constructed and used to build the forward absorption model.

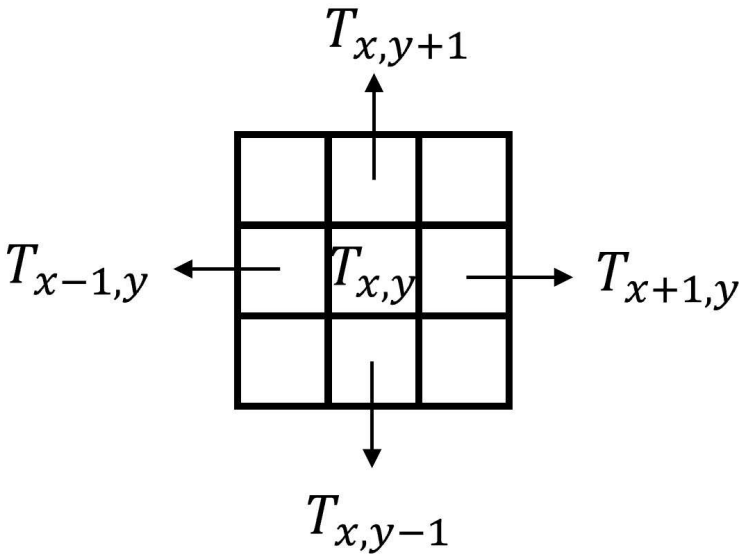

Figure 4.1: One unit extracted from the pixelized sensing region.

4.2 Methodology

The formulation of LAS tomography is described in section 2.5.1. Therefore, in this section, more attention is emphasized on *A Priori* information used for network training and the model architecture.

4.2.1 *A Priori* information

Instead of training the proposed neural network that only relies on the dataset, some *A Priori* information for the reconstruction of dynamic temperature is helpful to regularize and accelerate the process of model training.

In this work, two pieces of prior knowledge are imposed into the model to promote the learning ability of the CNN. First, the temperature is smoothly distributed. Regarding each local 9-pixel square in the sensing region as one unit, as shown in Figure, the temperature in the central pixel $T_{x,y}$ obeys:

$$\left| T_{x,y} - \frac{1}{4}\left(T_{x-1,y} + T_{x+1,y} + T_{x,y-1} + T_{x,y+1}\right) \right| < \Omega \tag{4.1}$$

where Ω is the threshold value.

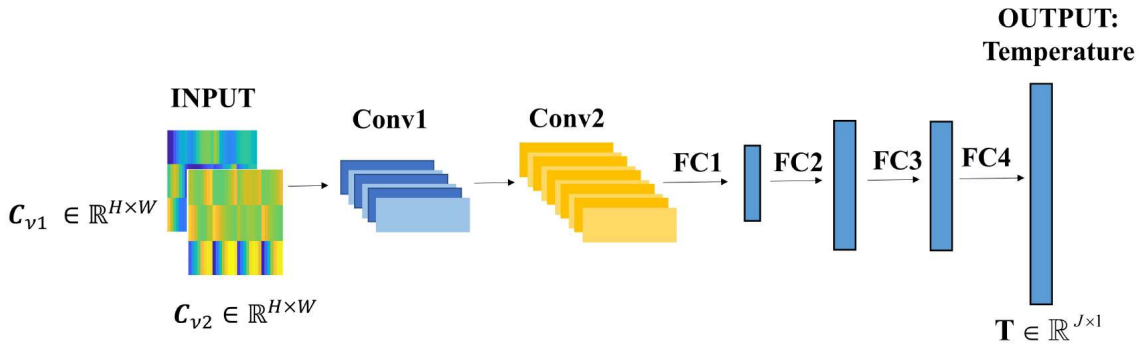

Figure 4.2: The architecture of the established model.

Second, as the optical paths of the lasers from the same angular view are similar, the theoretical measurements of adjacent laser beams will represent strong smoothness and correlation. As CNN is trained based on the receptive field filtered by a kernel, reshaping the correlated laser measurements to align with the size of the kernel facilitates the extraction of smoothness features from absorption spectroscopic imaging.

4.2.2 Model Architecture

As shown in Figure 4.2, the proposed CNN-aid model consists of two main parts: convolutional layers and fully-connected layers. By integrating the model with *A Priori* information from smoothness, which has been mentioned before, the measurements $\mathbf{A}_{v1} \in \mathbb{R}^{I\times 1}$ and $\mathbf{A}_{v2} \in \mathbb{R}^{I\times 1}$ from two absorption transitions are reshaped to generate the input feature maps $\mathbf{C}_{v1} \in \mathbb{R}^{H\times W}$ and $\mathbf{C}_{v2} \in \mathbb{R}^{H\times W}$, respectively. Then, the stacked $\{\mathbf{C}_{v1}, \mathbf{C}_{v2}\}$ is constructed to find the mapping relationship to the unknown temperature vector $\mathbf{T} \in \mathbb{R}^{J\times 1}$. This model contains two convolutional layers **Conv1** and **Conv2**, four fully-connected layers **FC1**, **FC2**, **FC3** and **FC4**. The involved mathematical operations will be detailed as follows:

Convolutional layers

The convolutional layers can be mathematically expressed as:

$$O_{\text{Conv}} = \eta(\mathbf{W}_{\text{Conv}} * \mathbf{I}_{\text{Conv}} + \mathbf{b}_{\text{Conv}}) \tag{4.2}$$

where $\mathbf{I}_{\text{Conv}} \in \mathbb{R}^{H_I \times W_I \times C_I}$ is the input or intermediate feature maps, $\mathbf{O}_{\text{Conv}} \in \mathbb{R}^{H_O \times W_O \times C_O}$ the output feature map, $\mathbf{W}_{\text{Conv}} \in \mathbb{R}^{H_W \times W_W \times C_W}$ the kernel matrix, $\mathbf{b}_{\text{Conv}} \in \mathbb{R}^{C_b \times 1}$ the bias vector. $*$ is the operand for 2D convolution, $\eta(\cdot)$ the activation function. Furthermore, H_I (H_O), W_I (W_O) and C_I (C_O) are the height, width and the number of channels of $\mathbf{I}(\mathbf{O})$. H_W, W_W and C_W are the filter height, filter width and the number of filters, respectively. C_b is the number of elements in b. The convolutional operation aims to extract the local connectivity of input feature maps so that the extracted characteristics can be further trained in the following fully-connected layers.

Fully-connected layers

The forward propagation within fully-connected layers can be described as:

$$\mathbf{O}_{\text{FC}} = \mathbf{g}(\mathbf{W}_{\text{FC}}\mathbf{I}_{\text{FC}} + \mathbf{b}_{\text{FC}}) \tag{4.3}$$

where $\mathbf{I}_{\text{FC}} \in \mathbb{R}^{N_I \times 1}$, $\mathbf{O}_{\text{FC}} \in \mathbb{R}^{N_O \times 1}$, $\mathbf{W}_{\text{FC}} \in \mathbb{R}^{N_O \times N_I}$ and $\mathbf{b}_{\text{FC}} \in \mathbb{R}^{N_O \times 1}$ are input vector, output vector, weight matrix and bias vector, respectively. $\mathbf{g}(\cdot)$ represents the activation function. The fully-connected layer provides a convenient way to learn the nonlinear combinations of extracted features and to change the flattened vector to the desired dimension.

4.3 Model Training and Testing

4.3.1 Simulation Setup

To test the designed algorithm, the optical layout with 128 laser beams is first developed in this section. As shown in Figure 4.3, 128 beams are divided into four groups and arranged in four equiangular projection angles at 0°, 45°, 90° and 135°, each angle with 32 equispaced parallel beams. The distance between the adjacent beams is 0.63 cm, which makes the octagonal sensing region with a side length of 48.7 cm. To achieve good spatial resolution of the reconstruction as well as considering the limited laser beams, this sensing region is determined to be uniformly discretized into 7,674 pixels. The central area with the densest beam arrangement, RoI, has 40 × 40 pixels with a side length of 20.2 cm. Water vapour (H_2O) is a significant product of combustion with strong near-infrared absorption spectra. Hence it is chosen as the desired target absorption species to evaluate the performance

of the proposed model. Two absorbing transitions at v_1 = 7185.6 cm^{-1} and v_2 = 7444.36 cm^{-1} are selected in consideration of their moderate line strengths and high-temperature sensitivities given the temperature range from 300 K to 1200 K [91]. Along with the projection data from the 128-beam tomographic sensor, the measurements $\mathbf{A}_{v_1} \in \mathbb{R}^{128\times1}$ and $\mathbf{A}_{v_2} \in \mathbb{R}^{128\times1}$ are obtained at v_1 and v_2 respectively. Table 4.1 shows the empirically determined hyper-parameters for model implementation.

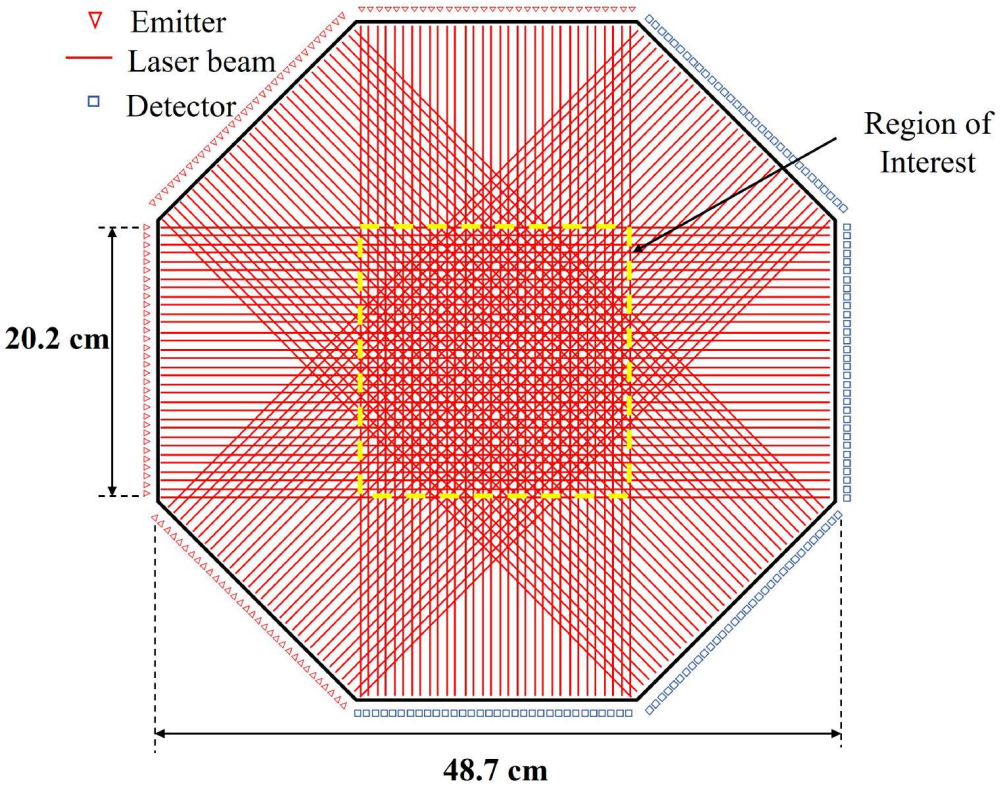

Figure 4.3: The proposed beam arrangement for LAS tomography image reconstruction.

4.3.2 Dataset Construction

An annular combustor with ten injectors simulation

Instead of simulating 2D distributions of temperature and species concentration using simple Gaussian profiles, we generate synthetic data for a ten-injector exhaust configuration by leveraging custom Gaussian functions and introducing random variations, which is based on the design of the gas turbine exhaust. This simulation involves calculating the angular positions and radii for the injectors and applying random variations to simulate realistic exhaust conditions. Specifically, each injector

Table 4.1: Empirical-determined hyper-parameters of the model

		Layers		
Name of the layer	Input dim.	Output dim.	Weight matrix	Stride
Conv1	$8 \times 16 \times 2$	$7 \times 8 \times 8$	2×2	(1,2)
Conv2	$7 \times 8 \times 8$	$6 \times 7 \times 32$	2×2	(1,1)
FC1	1344	2048	–	–
FC2	2048	4096	–	–
FC3	4096	4096	–	–
FC4	4096	7674	–	–

has a fixed radius of 8 cm. The computational domain is represented by a 96 × 96 Cartesian mesh, corresponding to a physical size of 48.7 cm × 48.7 cm. Within this domain, a RoI is defined with a size of 40 × 40 Cartesian mesh. To better mimic the combustion process, both symmetric and asymmetric configurations have been considered. Consequently, this approach results in a comprehensive training dataset comprising 19,200 samples and a test dataset comprising 4,800 samples, providing a robust basis for model training and evaluation.

FDS-based circular burner simulation

We use FDS, which is developed by the National Institute of Standards and Technology (NIST), to simulate heat transport of fire dynamics [92]. By solving a form of Navier-Stokes equations [68], FDS is capable of mimicking the temperature distributions within a dynamic field. Here, a circular burner is modeled. Similar to the ten-plume simulation, we established an open 3D space with a $96 \times 96 \times 96$ Cartesian mesh corresponding to 48.7 cm $\times$ 48.7 cm $\times$ 48.7 cm domain with open boundaries. The burner is located at the center of the lower boundary. Thus, a simple upwind boundary condition is built, which has little effect on the development of the burner within this computational domain. Propane is chosen as the fuel. To improve the generalization of the model, the training set is established by simulating and recording the whole burning process of an individual flame multiple times.

After visualizing the output of FDS, the cross-sectional images of temperature and gas concentration at 6 cm above the burner outlet are saved with an automatically adjusted time step, which obeys Courant-Friedrichs-Lewy condition [92]. The obtained dataset contains 11,714 samples from 10 different simulations by varying the mass fraction of the propane, flame duration and the spread rate of the flame. The sensit-

ivity matrix **L** has been determined by the optical layout of the tomography system. Therefore, after generating the phantoms of 2D distributions of temperature and gas concentration, the path-integrated absorbance for each transition $\mathbf{A}_{v1}$ and $\mathbf{A}_{v2}$ can be calculated. It is then randomly divided into a training set with 11,125 samples and a test set with 589 samples.

For both simulations, standardization can feature scaling to accelerate the convergence of the training process and improve the stability of the model. Thus, the simulated $\mathbf{A}_{v,i}$ is rescaled to $\mathbf{A}^S_{v,i}$ by:

$$\mathbf{A}^S_v = \frac{\mathbf{A}_{v,i} - \mu_{\mathbf{A}_{v,i}}}{\sigma_{\mathbf{A}_{v,i}}} \tag{4.4}$$

where $\mu_{\mathbf{A}_{v,i}}$ is the mean value of the path-integrated absorption for i-th laser beam in the training set, $\sigma_{\mathbf{A}_{v,i}}$ the standard deviation. To align the test data with the trained model, $\mathbf{A}_{v,i}$ within the test set will follow the same calculation for rescaling. Finally, the stacked $\{\mathbf{A}^S_{v_1}, A^S_{v_2}\}$ and corresponding temperature distribution $\mathbf{T} \in \mathbb{R}^{7674\times 1}$ will be deployed into the model for training and testing.

4.3.3 Loss Function

The proposed algorithm is trained by a customized loss function after considering the *A Priori* smoothness information, being demonstrated in section 4.2.1, as well as the importance of temperature reconstruction in the RoI and the background. The loss function can be expressed as

$$\begin{aligned} \text{Total Loss} = \lambda \times \frac{1}{B}\sum_{b=1}^{B}\left\| T_b^{\text{rec,RoI}} - T_b^{\text{tru,RoI}} \right\|_2^2 + \\ \frac{1}{B}\sum_{b=1}^{B}\left\| T_b^{\text{rec,BG}} - T_b^{\text{tru,BG}} \right\|_2^2 + \\ \frac{1}{B}\sum_{b=1}^{B}\left\| T_b^{\text{rec,RoI}(x,y)} - T_b^{\text{rec,smooth}} \right\|_2^2 \end{aligned} \tag{4.5}$$

where B represents the batch size, equalling 128. $T_b^{\text{rec,ROI}} \in \mathbb{R}^{1600\times 1}$ and $T_b^{\text{tru,ROI}} \in \mathbb{R}$ are the reconstructed and the true image vectors of b-th training sample within ROI, respectively. λ is a training-determined hyper-parameter, equalling 1.5. This term strengthens the reconstructed image error sourced from ROI. $T_b^{\text{rec,BG}} \in \mathbb{R}^{6074\times 1}$ and $T_b^{\text{tru,BG}} \in \mathbb{R}^{6074\times 1}$ are the reconstructed and the true image vectors of b-th training

sample in the background, respectively. $T_b^{\text{rec,smooth}}$ equals to

$$T_b^{\text{rec,smooth}} = \frac{1}{4}\left(T_b^{\text{rec,RoI}(x-1,y)} + T_b^{\text{rec,RoI}(x+1,y)} + T_b^{\text{rec,RoI}(x,y-1)} + T_b^{\text{rec,RoI}(x,y+1)}\right) \tag{4.6}$$

The third item of the loss function imposes smoothness regularization.

ReLU is chosen as the activation function. $L2$ regularization is deployed into the loss function to avoid overfitting with a penalty factor 2×10^{-6}. Adam optimizer is implemented with a learning rate of 2×10^{-4}. The number of epochs is 400 to allow the model to fully converge in an NVIDIA Tesla P100 GPU on Google Colab.

4.3.4 Test Results

Image Error (IE) evaluates the overall quality of the reconstructed image by considering each pixel's error, thus can represent the ability of the model on dynamic flow field retrieval. It is defined as

$$\text{IE} = \frac{1}{Q}\sum_{q=1}^{Q}\frac{\left\|\mathbf{T}_q^{\text{rec}} - \mathbf{T}_q^{\text{tru}}\right\|_2}{\left\|\mathbf{T}_q^{\text{tru}}\right\|_2} \tag{4.7}$$

where Q and q are the total numbers of test samples and the sample index, respectively. $\mathbf{T}_q^{\text{tru}}$ and $\mathbf{T}_q^{\text{rec}}$ denote the temperature vectors of the ground truth and the reconstruction for q-th test sample, respectively. $\|\cdot\|_2$ is a Euclidean norm of the vector.

Besides the original test set, which is split from the original simulation dataset without additional noise contamination, three more test sets are generated to validate the proposed model by adding different levels of white noise on path-integrated absorbance, following this formulation:

$$\mathbf{A}_{n,i} = \mathbf{A}_{v,i} + n_{\mathbf{A}_{v,i}}, \tag{10}$$

where $\mathbf{A}_{n,i}$ is the contaminated path-integrated absorbance of i-th beam and $n_{\mathbf{A}_{v,i}}$ is the white noise. Then, four test sets with no noise, 20 dB noise, 30 dB (the reasonable noise levels in real experiments) noise and 40 dB noise are fed into the well-trained model, respectively.

Ten-injector Annular Combustor Simulation

Figure 4.4 (a) shows the variable of IE across different noise levels. It can be seen that there is a large drop in IE when the noise level decrease from 20 dB to 30 dB, with a reduction of 0.006. Following this sharp decline, IE continues to decrease gradually from 30 dB towards the noise-free condition. The highest IE value is observed data an SNR of 20 dB, measuring at 0.0475, which remains relative low. This trend demonstrates the CNN effectiveness in reconstruction temperature fields and highlights it robustness to noise.

Figure 4.5 displays the reconstruction of the dynamic temperature images when the SNR is 30 dB. The images in the left column are the ground-truths, the middle column shows their reconstruction results as well as the right column showcasing their corresponding error images. It can be seen that the reconstructed images (b), (e), and (h) closely resemble the ground-truth images (a), (d), and (g), respectively. The temperature distributions and the general shape of the temperature plumes are well-preserved in the reconstructions, although there is a slight smoothing effect visible in the reconstructed images compared to the ground-truth images.

FDS-based Circular Burner Simulation

Similar to Figure 4.4 (a), Figure 4.4 (b) depicts the dependency of IEs on different noise levels for the optimally trained model. It can be seen obviously that IE decreases as SNR increases. More specifically, IEs remain the small values and increase only by 0.5% when SNR varies from 0 to 20 dB. It indicates the reliability and robustness of the proposed algorithm in terms of strong noise tolerance and good accuracy for dynamic flow field reconstruction, as well as effectiveness on the extraction of physical information from simulated combustion. Regarding the practical SNR of 30 dB in physical experimental situations, the reconstructed results of the three selected phantoms from the test set with 30 dB noise are visualized in Figure 4.6. In the first column, phantom (a), (d) and (g) are the original temperature distributions, whereas phantom (b), (e) and (h) in the second column are the corresponding reconstructions. As mentioned above, the dataset is established by recording each time step of the whole combustion process, from igniting to extinguishing, thus the profile of the flame will change dramatically. Although it introduces much more complexity to the training

model, the proposed network can indicate the edge of the heat zone and specify the correct position of the peak temperature. In addition, the proposed algorithm eliminates image artifacts effectively. As a result, the reconstructed temperature images have better spatial resolution and accuracy.

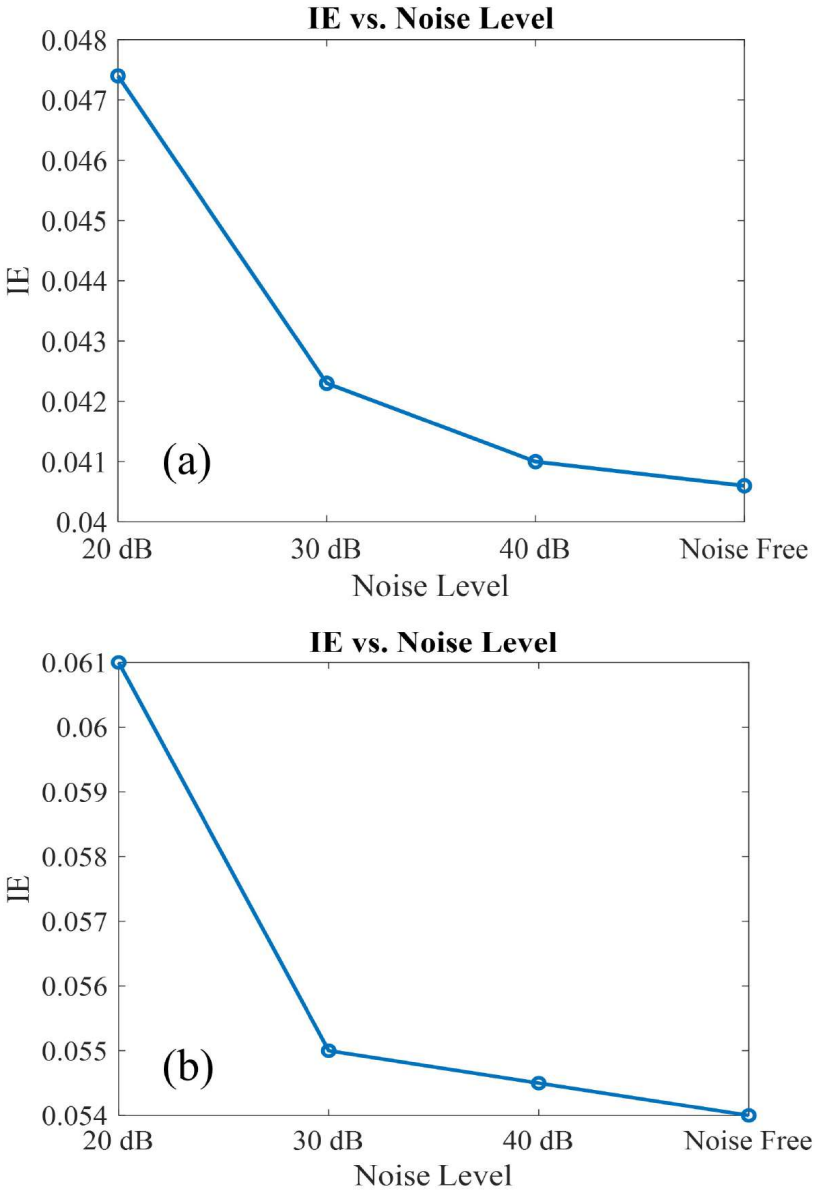

Figure 4.4: The change of IEs when reconstructing the dynamic gas temperature images with different SNRs on the simulation of (a) the annular combustor with ten injectors simulation; and (b) the circular burner using FDS

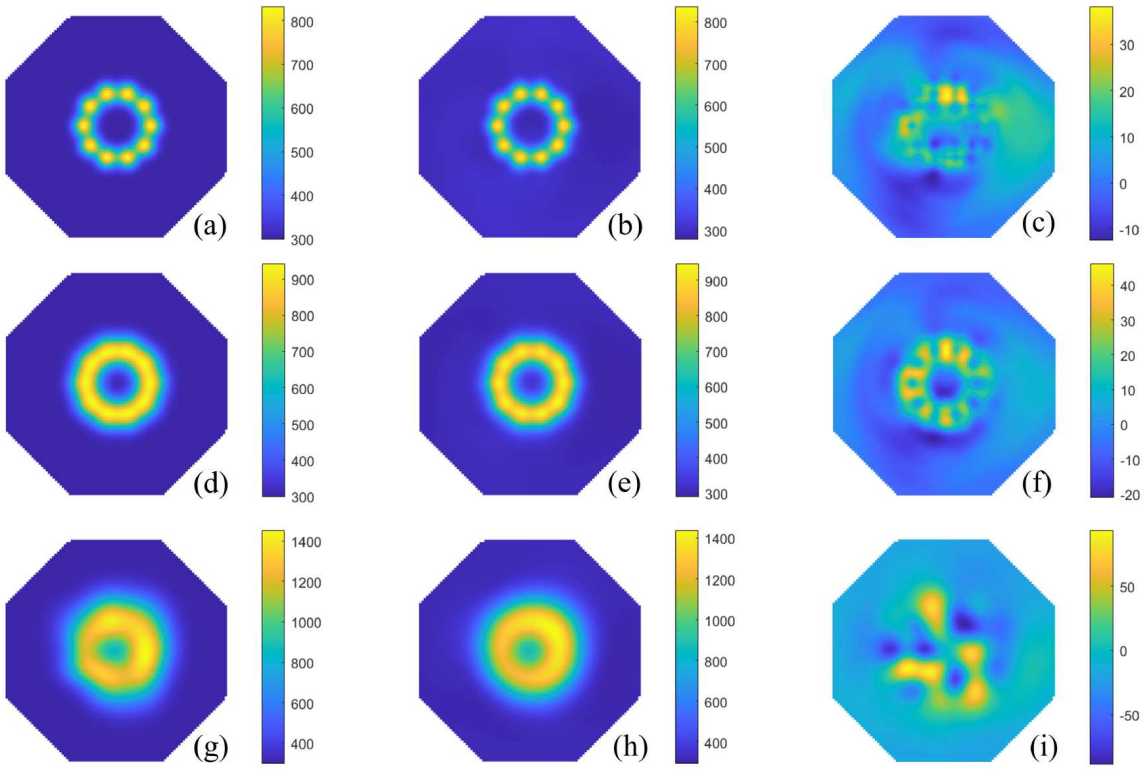

Figure 4.5: Reconstruction of temperature images for the simulated annular combustor when SNR is 30 dB. Phantom (a), (c) and (e) are the ground-truth images. (b),(d) and (f) are the corresponding reconstructed temperature images, respectively. (c), (f) and (i) are the error maps between the ground truths and the reconstructions.

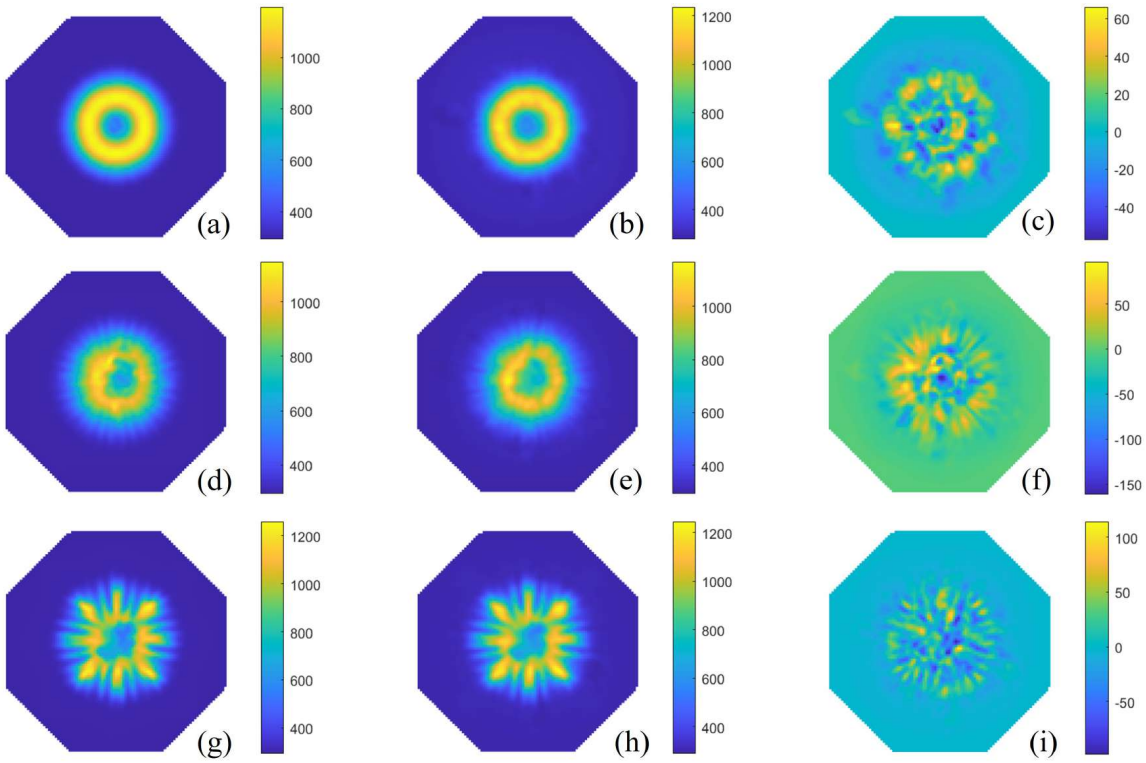

Figure 4.6: Reconstruction of dynamic temperature images for the simulated circular burner phantoms when SNR is 30 dB. Phantom (a), (d) and (g) are the ground-truth images from different time steps. (b),(e) and (h) show the corresponding reconstructed temperature images, respectively. (c), (f) and (i) are the error maps between the ground truths and the reconstructions.

4.4 Summary

In this chapter, a CNN-aided algorithm is proposed to achieve dynamic temperature imaging. Two simulated datasets are constructed to capture the reactive flow in different applications. The first dataset is built based on the structure of an annular combustor with ten injectors in a real gas turbine, and the other models a circular burner's combustion process, coupled with the application of a mid-fidelity tool for reactive flow simulation. This new development captures the dynamic features of the flame and builds an end-to-end mapping between the forward laser absorption and its temperature distribution. It reliably predicts the working state of the burner with fewer artifacts and higher image resolution, even under the condition of limited projection data.

The performance of the algorithm is evaluated using the simulated dataset from the two H_2O transitions for the proposed 128-way tomographic sensor. Different levels of white noise are added to the test set to examine its accuracy and noise tolerance. Simulation results show strong consistency between the original temperature images and the reconstructions. Further quantified by IE in a wide range of SNRs, this algorithm can effectively and stably capture the physical features from absorption data and have a strong tolerance with noise-contaminated data. In summary, this physics-involved CNN-aid model investigates the dynamic evolution of the flames and reconstructs temperature imaging with good accuracy and robustness.

The proposed CNN-aided algorithm successfully demonstrates its ability to dynamically capture and reconstruct temperature distributions in complex reactive flows. By utilizing both simulated datasets, it addresses the challenges posed by limited data projections and noise contamination, making it suitable for real-world applications in industrial combustion systems. The integration of physics-based modelling with deep learning not only improves image resolution and artifact reduction but also enhances the robustness of the predictions under noisy conditions. However, the model's heavy reliance on specific datasets limits its generalizability to different industrial setups and scenarios. Therefore, developing more robust and generalized algorithms is crucial for broader gas diagnosis in diverse industrial environments.

Based on the research of this chapter, one conference paper has been published:

- **Y. Fu**, R. Zhang, G. Enemali, A. Upadhyay, M. Lengden, C. Liu, "Convolutional neural network aided chemical species tomography for dynamic temperature imaging," *2022 IEEE International Instrumentation and Measurement Technology Conference (I2MTC)*, Ottawa, Canada, 2022.

Chapter 5

Model-informed double image prior for flow-field imaging using LAS tomography

5.1 Introduction

As introduced in Section 2.5, LAS tomography has been demonstrated as a robust and effective technique for imaging of reactive flow-field diagnosis. However, it is inherently ill-posed due to its limited availability to laser-beam measurements. As a result, LAS tomography reconstructions generally suffer from heavy artefacts, which hinder the interpretation of flow-file behaviors. To solve this issue, the regularization method, that adopt hand-crafted priors, i.e., smoothness and non-negativity, into the iterative method to mitigate the artefacts, such as the modified Landweber algorithm (shown in section 2.6.1). For example, Tikhonov regularization is effective to penalize reconstruction instability, however, at the cost of reconstruction accuracy [93; 94]. Other limitations of the regularization methods exist in terms of (a) the hand-crafted priors that are insufficient to indicate real flow-field features and (b) the complex decoupling of temperature and species concentration from the nonlinear LAS tomography inverse problem. Therefore, a LAS tomography imaging algorithm that is both artefact-rejective and computationally effective is highly demanded.

Most of deep learning algorithms require a large amount of training data to get the optimal model performance, including the ground-truth temperature and concentration distributions. Practically, it is hard to obtain the real temperature and concentration images due to the limitation of the measurement facilities and difficulty in operation. Besides, the underlying physical information derived from model formulation has been neglected and the generalization ability is questioned since the model performance

is highly relied on the dataset. These uncertainties and limitations are concerned when deployed into practical industrial use, e.g., the reactive flow reconstruction for gas turbine machine to monitor the combustion efficiency and ensure the safety of the machine operation. Therefore, the guaranteed accuracy prediction are extremely important.

To address the above challenges that encountered in regularization and deep learning-based algorithms, we propose an Untrained Neural Network (UNN)-based LAS tomography algorithm, named Model-Informed Double Image Prior (MI-DIP), for high-fidelity and effective reconstruction of temperature and species concentration. The developed algorithm is validated both numerically and experimentally. Our key contributions are:

(1) A dual-path UNN is introduced, for the first time, to reconstruct dual flow-field parameters, i.e., temperature and species concentration, using LAS tomography. Fully independent from training datasets, the developed algorithm eliminates any potential simulation-introduced errors, thus improving its generalizability in real scenarios.

(2) The proposed algorithm formulates the physical absorption model in the process of model optimization. Such development enables learning of real-world measurements, thus enhancing the fidelity of dual-image reconstruction.

(3) A differentiable soft-threshold scheme is designed to integrate the regularization scheme, such as Tikhonov regularization, into the UNN. This integration effectively stabilizes the LAS tomography reconstruction, and meanwhile, improves trustworthiness of the UNN by adding weights of measurement-inferred reconstruction.

5.2 Mathematical Background

5.2.1 Updated Mathematical Formulation of LAS Tomography

Based on the formulation in Eq.(2.35), the forward problem in LAS tomography can be simply depicted as:

$$\mathbf{A}_v = \mathbf{L}\mathbf{a}_v = \mathbf{L}[P \cdot S_v(\mathbf{T}) \cdot \mathbf{X}] = \mathbf{L}f_v(\mathbf{T}, \mathbf{X}) \tag{5.1}$$

and the corresponding vector of absorbance density can be updated to:

$$\mathbf{a}_v = P \cdot S_v(\mathbf{T}) \cdot \mathbf{X} = f_v(\mathbf{T}, \mathbf{X}) \tag{5.2}$$

where $\mathbf{T} \in \mathbb{R}^{N\times 1}$ is the temperature vector and $\mathbf{X} \in \mathbb{R}^{N\times 1}$ the concentration vector. $f_v(\cdot)$ represents the function that forward formulates LAS tomography.

When solving the inverse problem of LAS tomography, the vectors of path-integral absorbance at two absorption wavenumbers, i.e. v_1 and v_2, are required to reconstruct the 2D distributions of temperature and concentration [85]. Thus, optimization of the inverse problem can be simplified as:

$$\hat{\mathbf{T}}, \hat{\mathbf{X}} = \arg\min_{\mathbf{T},\mathbf{X}} \left\{ \|\mathbf{A}_{v1} - \mathbf{L} f_{v1}(\mathbf{T},\mathbf{X})\|_q + \|\mathbf{A}_{v2} - \mathbf{L} f_{v2}(\mathbf{T},\mathbf{X})\|_q \right\} \tag{5.3}$$

where $\hat{\mathbf{T}}$ and $\hat{\mathbf{X}}$ are the estimated vectors of temperature and concentration, respectively. $\|\cdot\|_q$ represents q-norm.

5.2.2 Tikhonv Regularization in LAS Tomography

Tikhonov regularization is used as a classic example of mathematical modeling in our MI-DIP framework to improve the trustworthiness of the framework by adding weights of measurement-inferred reconstruction. It has been introduced in the section 2.6. Its close-form solution is

$$\mathbf{a}_{\text{tik},v} = (\mathbf{L}^T\mathbf{L} + \lambda_{\text{tik}}\mathbf{S}^T\mathbf{S})^{-1}\mathbf{L}^T\mathbf{A}_v \tag{5.4}$$

Here, λ_{tik} is the regularization parameter to weight smoothness. $\mathbf{a}_{\text{tik},v1}$ and $\mathbf{a}_{\text{tik},v2}$ can be retrieved after solving the two inverse problems at v_1 and v_2, respectively. According to ratio thermometry, the ratio between $\mathbf{a}_{\text{tik},v2}$ and $\mathbf{a}_{\text{tik},v1}$, $\mathbf{r}$, is solely determined by $\mathbf{T}$, and can be expressed as:

$$\mathbf{r} = \frac{\mathbf{a}_{\text{tik},v2}}{\mathbf{a}_{\text{tik},v1}} = \frac{P \cdot S_{v2}(\mathbf{T}) \cdot \mathbf{X}}{P \cdot S_{v1}(\mathbf{T}) \cdot \mathbf{X}} = \frac{S_{v2}(\mathbf{T})}{S_{v1}(\mathbf{T})} \tag{5.5}$$

With $\mathbf{T}$ in hand, $\mathbf{X}$ can be obtained by using:

$$\mathbf{X} = \frac{\mathbf{a}_{\text{tik},v}}{P \cdot S_v(\mathbf{T}) \cdot \mathbf{X}} \tag{5.6}$$

Although artefacts may present in the reconstructions, Tikhonov regularization stabilizes the reconstruction during optimization of the MI-DIP model.

5.2.3 Deep Image Prior for Inverse Problem

Ulyanov et al. [95] firstly introduced the DIP-based algorithm for the inverse problem. It regards the Deep Neural Network (DNN) as a regularizer to the image restoration problem. Since the DIP-based algorithm leverages the powerful feature extraction ability of the DNN and eliminates the requirement of a large dataset, it attracts attentions from various fields, such as image denoising [96; 97], and image reconstruction [98].

Specifically, DIP represents the clear image $\mathbf{X}$ directly from the corrupted image, which can be formulated as:

$$\mathbf{X} = h_\gamma(\mathbf{Z}) \tag{5.7}$$

where h_γ represents the generator neural network with the initialized trainable weight γ. In our case, z is the random noisy absorbance as the input. Then, the corresponding reconstructed absorbance $\hat{\mathbf{X}}$ can be represented as $\hat{\mathbf{X}} = h_{\hat{\gamma}}(\mathbf{Z})$, where $\hat{\gamma}$ is the optimized weight. Fully independent from the dataset, DIP enables better generalization compared to the trained neural networks.

5.3 Proposed Method

In this section, we will first introduce the proposed MI-DIP, including its image representation, the integration of the physical absorption model with regularization, and the model optimization. Then, the neural network used in MI-DIP, i.e., Attentioned Dual-branch Convolutional Neural Network (AD-CNN), will be elaborated.

5.3.1 Dual-Image Reconstruction based on MI-DIP

Dual-Image Representation

According to the DIP image representation in 5.7, the 2D temperature $\mathbf{T}_{\text{rec}} \in \mathbb{R}^K$ and species concentration $\mathbf{X}_{\text{rec}} \in \mathbb{R}^K$ to be reconstructed can be represented as:

$$\mathbf{T}_{\text{rec}}, \mathbf{X}_{\text{rec}} = h_\gamma(\mathbf{Z}_T, \mathbf{Z}_X) \tag{5.8}$$

where $\mathbf{Z}_T \in \mathbb{R}^{K\times K}$ and $\mathbf{Z}_X \in \mathbb{R}^{K\times K}$ are the input noise images for the temperature and the species concentration, respectively. $K = \sqrt{N}$ is the size of the reconstructed image. This image representation scheme will allow the neural network (a) to learn the features of gas-parameter distributions without relying on the pre-labeled training data; and (b) to leverage neural network architecture as a regularizer and a denoiser to solve the inverse problem of LAS tomography.

Problem Formulation with Physical Absorption Model

To improve the generalization of the neural network against unknown measurement noise, the physical absorption model is infused by calculating the estimated vector of absorbance $\mathbf{a}_{\mathrm{rec},v}$ using $\mathbf{T}_{\mathrm{rec}}$ and $\mathbf{X}_{\mathrm{rec}}$:

$$\mathbf{a}_{\mathrm{rec},v} = P \cdot \mathbf{S}_v(\mathbf{T}_{\mathrm{rec}}) \cdot \mathbf{X}_{\mathrm{rec}} = f_v(\mathbf{T}_{\mathrm{rec}}, \mathbf{X}_{\mathrm{rec}}) = f_v(h_\gamma(\mathbf{Z}_T, \mathbf{Z}_X)) \tag{5.9}$$

Then, a differentiable soft-threshold scheme is built to further stabilize the model performance. It can be expressed as:

$$\mathrm{ST}(\mathbf{q}) = \begin{cases} 1, \text{if } q_n \geq \omega \\ 0, \text{if } q_n < \omega \end{cases} \tag{5.10}$$

where q_n is the n-th element of the vector q. ω is the threshold value. The soft-threshold of q, denoted as $\mathrm{ST}(\mathbf{q})$, equals either '0' or '1' depending on q_n. Based on this scheme, the vectors of soft-threshold absorbance $\mathbf{M}_v$ and $\mathbf{M}_{\mathrm{tik},v}$ can be obtained by applying Eq.(5.10) to $\mathbf{a}_{\mathrm{rec},v}$ calculated in Eq.(5.9) and $\mathbf{a}_{\mathrm{tik},v}$ in Eq. (5.4), respectively. This process can be formulated as:

$$\mathbf{q}_v = \mathbb{N}(\mathbf{a}_{\mathrm{rec,v}}), \quad \mathbf{q}_{\mathrm{tik},v} = \mathbb{N}(\mathbf{a}_{\mathrm{tik,v}}) \tag{5.11}$$

$$\mathbf{M}_v = \mathrm{ST}(\mathbf{q}_v) \cdot \mathbf{q}_v, \quad \mathbf{M}_{\mathrm{tik},v} = \mathrm{ST}(\mathbf{q}_{\mathrm{tik},v}) \cdot \mathbf{q}_{\mathrm{tik},v} \tag{5.12}$$

where $\mathbf{q}_v$ and $\mathbf{q}_{\mathrm{tik},v} \in (0,1)$ are the normalized $\mathbf{a}_{\mathrm{tik},v}$ and $\mathbf{a}_{\mathrm{rec},v}$, respectively. $\mathbb{N}(\cdot)$ represents the normalization operation. ω is set as 0.5 in this case.

By integrating the prior information of Tikhonov into model optimization, the error between $\mathbf{M}_v$ and $\mathbf{M}_{\mathrm{tik},v}$, noted as $R_{\mathrm{ST},v}\left(f_v(h_\gamma(\mathbf{Z}_T, \mathbf{Z}_X))\right)$ will be minimized as Eq.(5.13) to refine reconstructions.

$$R_{\mathrm{ST},v}(f_v(h_\gamma(\mathbf{Z}_T, \mathbf{Z}_X))) = \left\|\mathbf{M}_v - \mathbf{M}_{\mathrm{tik},v}\right\|_1 \tag{5.13}$$

Consequently, the dual-image reconstruction can be formulated as a penalized optimization problem:

$$\hat{\gamma} = \underset{\gamma}{\operatorname{argmin}} \left\{ \left\| \mathbf{A}_v - \mathbf{L} f_v(h_\gamma(\mathbf{Z}_T, \mathbf{Z}_X)) \right\|_1 + \eta \cdot R_{\mathrm{ST},v}(f_v(h_\gamma(\mathbf{Z}_T, \mathbf{Z}_X))) \right\} \tag{5.14}$$

where $\eta > 0$ weights the regularization item generated by $R_{\mathrm{ST},v}$. The final objective function of the proposed MI-DIP algorithm after integrating Eq.(5.3) into Eq.(5.14) can be expressed as:

$$\zeta = \arg\min_{\gamma} \left\{ \begin{array}{l} \|\mathbf{A}_{v1} - \mathbf{L} f_{v1}(\kappa)\|_1 + \|A_{v2} - \mathbf{L} f_{v2}(\kappa)\|_1 \\ +\eta \cdot (R_{\mathrm{ST},v1}(f_{v1}(\kappa)) + R_{\mathrm{ST},v2}(f_{v2}(\kappa))) \end{array} \right\} \tag{5.15}$$

where $\kappa = h_\gamma(\mathbf{Z}_T, \mathbf{Z}_X)$.

Opitimization

In the MI-DIP algorithm, we adopt a widely used optimizer, Adam, to solve Eq.(5.15). We suppose the current iteration as $\theta \in \{0, 1, 2, \ldots, \Theta\}$. Thus, the gradient of ζ with respect to the neural-network parameter γ_θ at θ-th iteration can be calculated as:

$$\frac{\partial \zeta}{\partial \gamma_\theta} = (\frac{\partial F}{\partial \kappa})^T \frac{\partial \kappa}{\partial \gamma_\theta} + \eta (\frac{R_{\mathrm{ST}}}{\partial \kappa})^T \frac{\partial \kappa}{\partial \gamma_\theta} \tag{5.16}$$

where $F = \|\mathbf{A}_v - \mathbf{L} f_v(\kappa)\|_1$. As each item in Eq(5.16) is differentiable and in-tensor, it can be implemented using the PyTorch built-in automatic backpropagation mechanism called $torch.autograd$. Afterward, the parameter γ_θ can be updated following the Adam optimization rule:

$$\hat{m}_\theta = \frac{\beta_1 m_{\theta-1} + (1-\beta_1)\frac{\partial \zeta}{\partial \gamma_\theta}}{1-\beta_1^\theta} \tag{5.17}$$

$$\hat{v}_\theta = \frac{\beta_2 v_{\theta-1} + (1-\beta_2)\left(\frac{\partial^2 \zeta}{\partial (\gamma_\theta)^2}\right)}{1-\beta_2^\theta} \tag{5.18}$$

$$\gamma_{\theta+1} = \gamma_\theta - \frac{\varepsilon}{\sqrt{\hat{v}_\theta}} \hat{m}_\theta \tag{5.19}$$

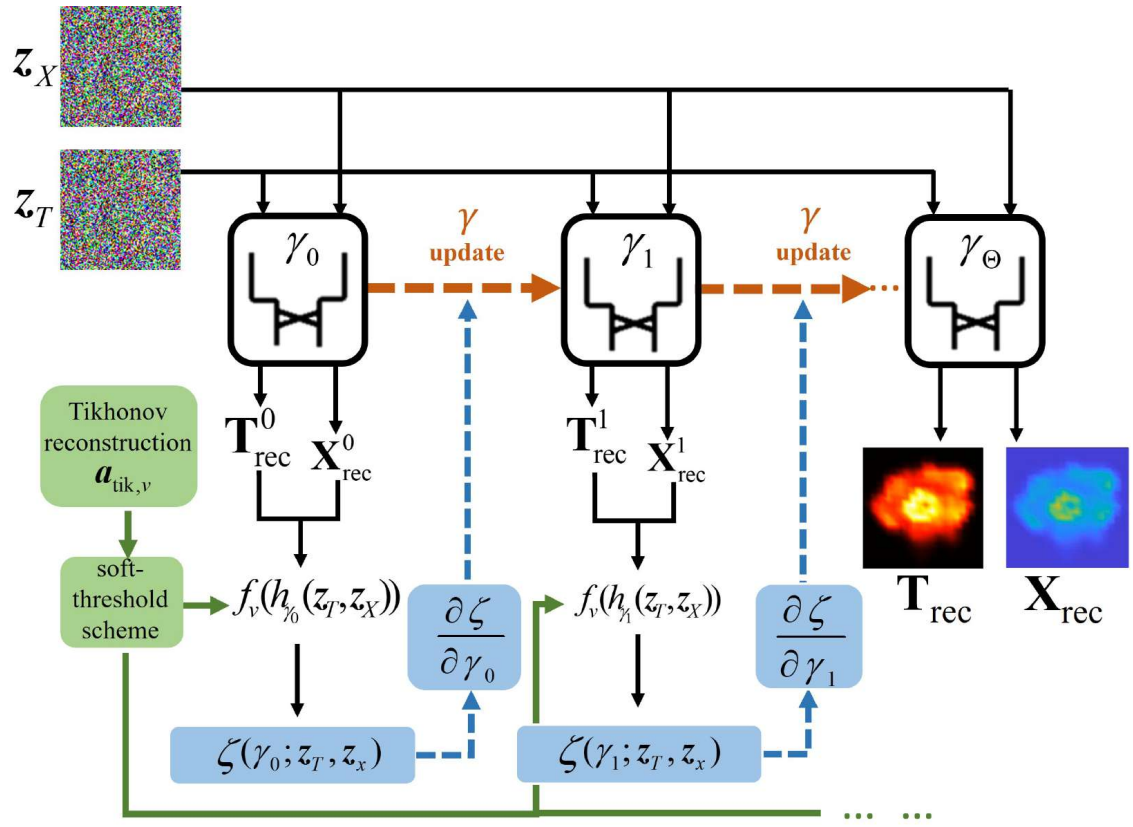

Figure 5.1: Flowchart of the proposed MI-DIP algorithm for reconstruction of temperature and gas concentration.

where β_1 and β_2 are exponential decay rates for the moment estimates (commonly 0.9 and 0.999). $\hat{m}_\theta$ and $\hat{v}_\theta$ are the bias correction for the first-moment estimate and the second-moment estimate [99]. The flowchart of the proposed MI-DIP is illustrated in Figure 5.1.

5.3.2 Attentioned Dual-branch Convolutional Neural Network

As shown in Figure 5.2, the AD-CNN, involved in the MI-DIP to calculate $\mathbf{T}_{\text{rec}}$ and $\mathbf{X}_{\text{rec}}$ from $\mathbf{Z}_T$ and $\mathbf{Z}_X$, mainly consists of a dual-branch CNN and the Spatial-Attentioned Mechanism (SAM) to crosstalk the two branches.

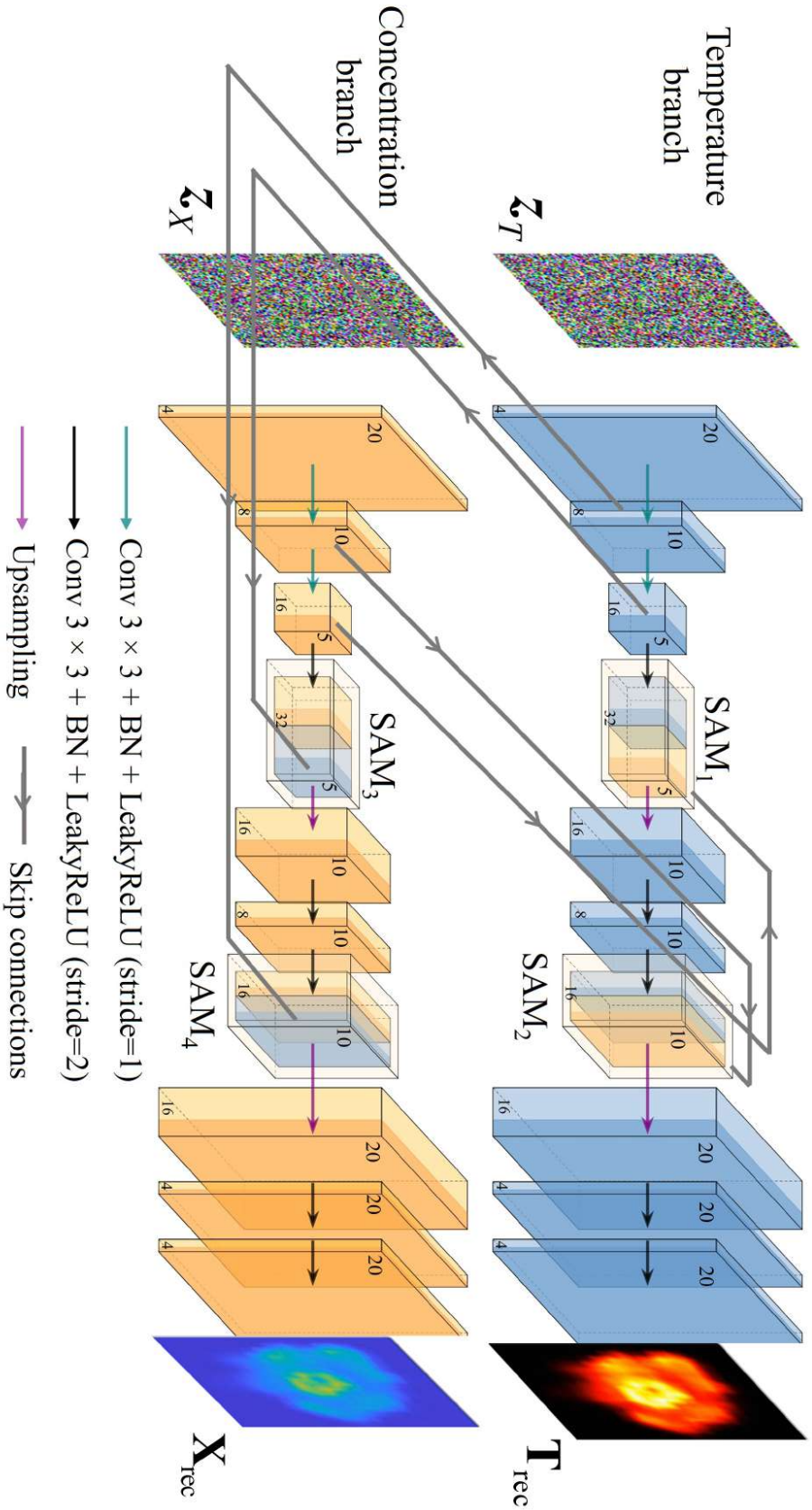

Figure 5.2: Architecture of the AD-CNN in the MI-DIP algorithm.

Dual-branch CNN

In many DIP-related neural networks [95; 100], a convolutional autoencoder is deployed with skip connections for different image-reconstruction tasks. The typical architecture is U-net [101]. Our AD-CNN consists of a temperature-retrieval branch and a concentration-retrieval branch. Each branch is a U-shaped convolutional autoencoder. It consists of the repeated deployment of three convolutional layers with 3×3 kernels (Conv 3×3), each followed by a Batch Normalization (BN) layer and a leaky rectified linear unit (LeakyReLU) with the stride of 1. The stride will change to 2 during down-sampling. The up-sampling is set as bi-linear operations. As shown in Figure 5.2, either down-sampling or up-sampling has two stages, represented by the green arrows and purple arrows, respectively. The parameters of the architecture, including the number of channels and the size of the feature maps, are also shown in Figure 5.2.

Spatial-Attentioned Mechanism (SAM)

In reactive flows, the correlation could exist between the distributions of temperature and some species concentration [63]. In the proposed MI-DIP, SAM is incorporated to build the external crosstalk to share the image features between these two branches. This mechanism is inspired by the attention gate model in Attention U-Net [102], which was initially deployed into biomedical image segmentation [103]. It highlights the salient features by scaling them with the computed attention coefficient $\alpha \in (0,1)$. Then, this attention coefficient multiplies the input feature maps, marked as $\mathbf{I}_1 \in \mathbb{R}^{D\times D}$ and $\mathbf{I}_2 \in \mathbb{R}^{D\times D}$, to obtain the output of the SAM, $\mathbf{O}_{\mathrm{SAM}} \in \mathbb{R}^{D\times D}$, as shown in Figure 5.3. This scheme can be formulated as follows:

$$\mathbf{I}_{\mathrm{int}} = \rho\{\mathrm{BN}(\mathbf{W}_1 * \mathbf{I}_1 + b_1) + \mathrm{BN}(\mathbf{W}_2 * \mathbf{I}_2 + b_2)\} \tag{5.20}$$

$$\alpha = \sigma\{\mathrm{BN}(\mathbf{W}_3 * \mathbf{I}_{\mathrm{int}} + b_3)\} \tag{5.21}$$

$$\mathbf{O}_{\mathrm{SAM}} = \alpha \cdot \mathbf{I}_2 \tag{5.22}$$

where the operator $*$ represents convolution, BN the batch normalization. $\mathbf{W}_1 \in \mathbb{R}^{D\times D}$ ($\mathbf{W}_2 \in \mathbb{R}^{D\times D}, \mathbf{W}_3 \in \mathbb{R}^{D\times D}$) and $b_1 \in \mathbb{R}^1 (b_2 \in \mathbb{R}^1, b_3 \in \mathbb{R}^1)$ are the convolutional kernels and bias, respectively. ρ and σ are the LeakyReLU and Sigmoid activation function, respectively. We added four SAMs in total, labeled as SAM1, SAM2, SAM3 and SAM4

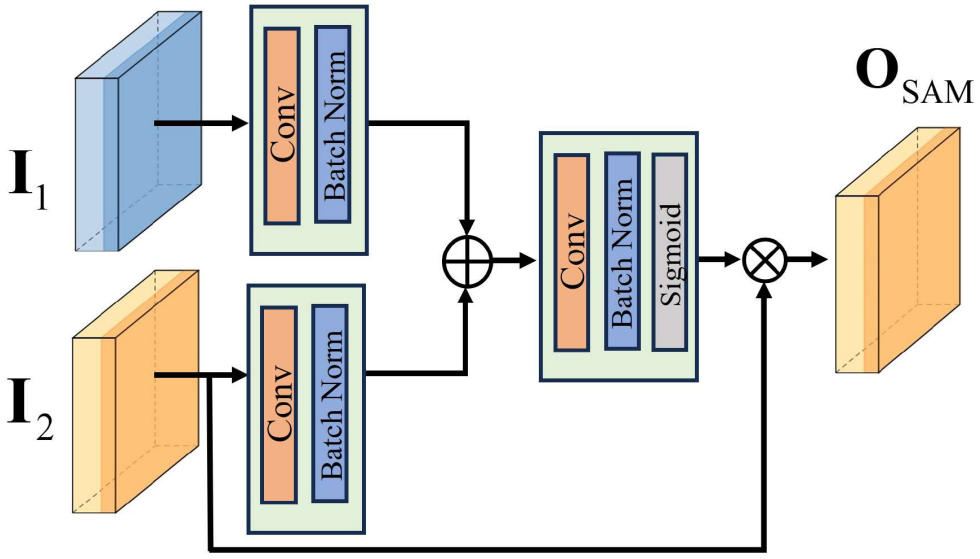

Figure 5.3: Architecture of the SAM in the MI-DIP algorithm.

in Figure 5.2, two SAMs for each branch. Adding SAMs from different steps of the dual pathways aims to integrate multi-scale features into the model. Such features could enable the reusability of inherent information between the temperature distribution and the concentration distribution during the model optimization.

5.4 Experiment Setup and Results

5.4.1 System Setup

The lab-scale experiment was carried out to validate the performance of the MI-DIP. We developed an octagon 32-beam LAS tomography system, i.e., M = 32. As shown in Figure 5.4, 32 beams are equally divided into four groups and arranged into four equiangular projection angles, i.e., 0, $45°$, $90°$ and $135°$. The central beam-dense square area is defined as the ROI, which will be the target imaging area. The beam spacing from the same projection angle, d, is 0.62 cm, leading to a 20 cm distance between an emitter and its corresponding detector L_{beam} and 7.5 cm side length of ROI. Here, ROI is uniformly discretized into 400 (K = 20) pixels, resulting in the sensitivity matrix $\mathbf{L} \in \mathbb{R}^{32\times400}$. As a common combustion product, water vapor (H_2O) is

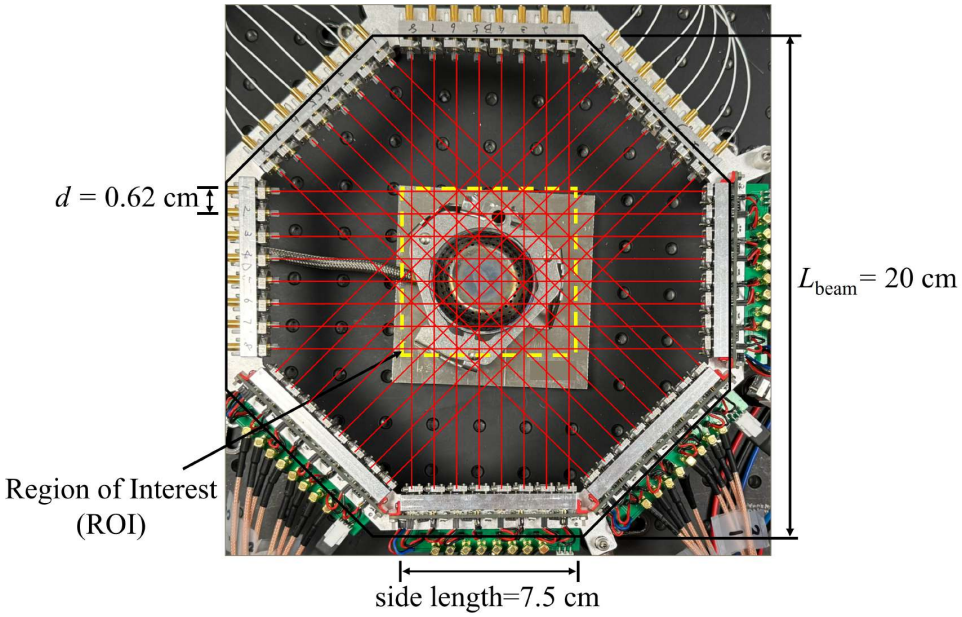

Figure 5.4: Optical layout of the 32-beam LAS tomography sensor.

selected as the targeted absorbing species. Two H_2O absorbing transitions v_1=7185.6 cm-1 and v_2=7444.36 cm-1 are used due to their good temperature sensitivity across the target temperature range. These two lasers are provided by two distributed feedback laser diodes NLK1E5GAAA and NLK1B5EAAA (NTT Electronics), respectively. These two laser diodes are fiber-coupled and split to emit the 32 laser beams in the tomographic system. Then, the emitted laser signal from each laser is detected by their corresponding InGaAs photodiode (G12182-010K, Hananatsu). Thus, the vectors of integrated absorption $\mathbf{A}_{v1} \in \mathbb{R}^{32\times1}$ and $\mathbf{A}_{v2} \in \mathbb{R}^{32\times1}$ can be calculated at $v1$ and $v2$, respectively. More details of the optics, i.e., electronics, and data acquisition system, are illustrated in paper [80].

As shown in Figure 5.5, two gas stoves were used in the experiment, where stove 1 has three circular fuel outlets with a diameter of 2.5 cm and stove 2 has an annular fuel outlet with a diameter of 4.6 cm. In the experiment, they were located within the ROI at distances of 5 mm (stove 1) and 8 mm (stove 2) below the tomographic plane, respectively. Specifically, stove 1 was fueled using propone with a mass flow rate of 1.0925 L/min and stove 2 with 0.8114 L/min when they were at a stable combustion status. Meanwhile, an S-type TC was used to record the point-wised temperature references in the ROI at the same height as the lasers.

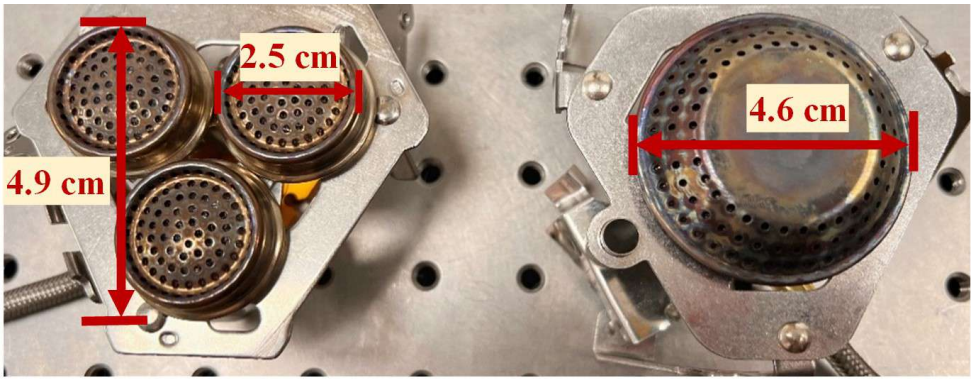

Figure 5.5: Combustion devices used in the experiment validation. (a) Stove 1 has three circular fuel outlets (b) Stove 2 has an annular fuel outlet.

5.4.2 Comparison Algorithms

The flame images reconstructed using the MI-DIP are compared to those obtained using the Tikhonov regularization and the traditional DIP algorithm. All three methods do not require a training dataset. More details for the implementation of each algorithm are shown below:

- Tikhonov regularization: It will get the reconstructed absorbance $\mathbf{a}_{\text{tik},v}$ for each absorption transition by solving Eq.(5.4). Empirically, we set the regularization parameter λ_{tik} to be 2.2 for the optimal reconstruction. Then the distributions of temperature and concentration can be calculated using Eq.(5.5, 5.6).
- DIP: It is a single-branch convolutional autoencoder. It has a similar architecture to MI-DIP, but without SAM and the attention schemes. We used DIP to retrieve the vectors of absorbance from two H_2O absorption transitions, which will be used to reconstruct the distributions of temperature and concentration by following Eq.(5.5, 5.6).

5.4.3 Implementation

The input temperature noise image $\mathbf{Z}_T \in \mathbb{R}^{20\times20}$ and species concentration image $\mathbf{Z}_X \in \mathbb{R}^{20\times20}$ were generated by the normalized distribution $\mathbf{Z}_T, \mathbf{Z}_X \sim (0, 0.1)$. To further stabilize the performance of the MI-DIP and eliminate the effect of systematic defect during model optimization, the outputs of the model, i.e., temperature and concentration, were scaled into [0,1] by using Min-Max normalization [18].

The MI-DIP, consisting of 17827 trainable parameters, was implemented in PyTorch framework. The computations were executed on a single GPU of NVIDIA A100-SXM4-40GB with the number of epochs varies from 1500 to 3000.

5.4.4 Experimental Results

Figure 5.6 shows the reconstructed 2D profiles of temperature and H_2O concentration in flames using Tikhonov regularization, DIP and MI-DIP under the stable combustion of two stoves. The TC measurement points are labeled and shown in the first row in Figure 5.6 alongside the photographs of the stoves. For the reconstructions from stove 1 (the left-half part in Figure 5.6, which includes both temperature and concentration reconstructions), all three methods can identify the high temperature/concentration zones, corresponding to the three fuel outlets on stove 1. However, the reconstructions from Tikhonov regularization have more artefacts than DIP, whereas MI-DIP eliminates most artefacts and shows smooth temperature and concentration distribution. Quantitatively, the retrieved temperature values from the MI-DIP at the center of the three hot spots are 1868.8 K (upper left), 1770.5 K (right) and 1726.6 K (lower left), with +91.8 K, +12.5 K and -21.4 K difference with those measured by the TC, compared to Tikhonov regularization with 1293.0 K (-484 K), 1404.4 K (-353.6 K) and 1158.4 K (-589.6 K) and DIP with 1711.0 K (-66 K), 1129.4 K (-628.6 K) and 1067.7 K (-680.3 K), respectively. The results indicate that the MI-DIP has the highest consistency and accuracy compared to the TC measurements.

For the reconstruction results from stove 2 (the right-half part in Figure 5.6), the retrieved high-intensity area from the MI-DIP demonstrates a good correlation with the actual flame's characteristics, where the edge areas of the flame have higher density than the center. Specifically, the retrieved temperature from the MI-DIP is approx. 1400 K at the flame edge of the flame lower temperature around 1170 K at

the flame center. In contrast, Tikhonov reconstruction shows 1046 K at the edge and 828 K at the center, whereas DIP shows 1630 K and 788 K correspondingly. It can be seen that the reconstructions from MI-DIP agree better with the TC measurements, which record a higher temperature of 1537 K at the edge and 1451 K at the center.

Overall, both visual and quantitative analysis demonstrate that the MI-DIP can reconstruct the high-temperature region accurately and exhibit a high sensitivity on distinguishing between the high and low-temperature regions. Since the TC provides references, rather than accurate values, slight discrepancies between the references and the LAS measurements are allowed. In total, the experimental results demonstrate the effectiveness of the MI-DIP on imaging temperature and $\mathrm{H_2O}$ concentration of combustion processes.

5.5 Statistical Analysis

To statistically examine the performance of the MI-DIP, we conducted a simulation with the available ground-truth gas images generated using FDS.

5.5.1 Simulation Setup

FDS with its embedded Large Eddy Simulation modeling was used to generate the distributions of temperature and H_2O concentration. Here, we established a 3D domain with a 48 $\times$ 48 $\times$ 96 Cartesian mesh, corresponding to a space of 200 mm $\times$ 200 mm $\times$ 400 mm. A circular burner with a radius of 60 mm was modelled and located at the center of the bottom boundary. Propone-methane mixture was chosen as the fuel with a mass fraction of 0.05 kg/m2/s and a spread rate of 2 m/s. The combustion process of the simulated circular burner was recorded over a period of 30 seconds, obtaining 50 frames of temperature and concentration images, each in size of 20 $\times$ 20. The path-integral absorbance $\mathbf{A}_{\mathrm{sim},v1} \in \mathbb{R}^{32\times 1}$ and $\mathbf{A}_{\mathrm{sim},v2} \in \mathbb{R}^{32\times 1}$ could be calculated by following Eq.(5.1) when using the same 32-beam LAS tomography setup as the experiment.

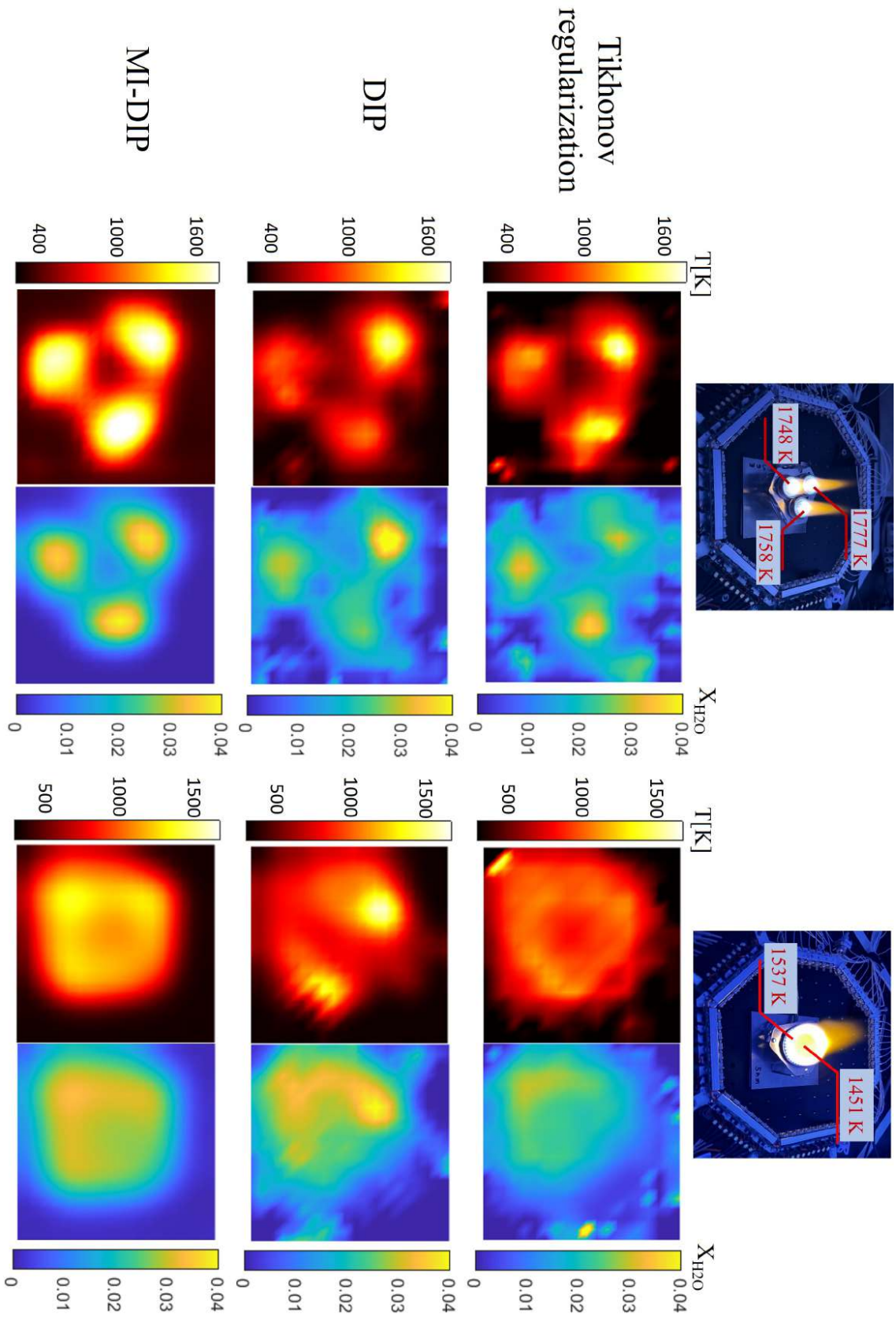

Figure 5.6: Combustion devices used in the experiment validation. (a) Stove 1 has three circular fuel outlets (b) Stove 2 has an annular fuel outlet.

5.5.2 Simulation Results

Qualitative Analysis

The video of the real-time H_2O concentration and temperature variation with the corresponding flame behavior can be found in Appendix A. This video shows the reconstruction of all 50 frames of temperature and H_2O concentration using the MI-DIP, Tikhonov regularization and DIP, respectively. Figure 5.7 shows two frames randomly selected from the video. For both frames, the reconstructions using Tikhonov regularization can characterize the high temperature/concentration region but introduce artefacts in the ambient region. In contrast, both DIP and MI-DIP can mitigate artifacts to some extent, indicating that the neural network's architecture itself has the effect of regularization on image reconstruction [95]. However, some artefacts still exist in both Tikhonov and DIP due to the propagation of the noise when following Eq.(5.5) and Eq.(5.6). In addition, they both excessively blur the high temperature/concentration regions, hindering the reveal of structural details of the dynamic flame. Compared to these two methods, the proposed MI-DIP can distinguish the boundary of the flame zone with a clearer transition from the high- to low-temperature/concentration regions. Facilitated by the SAM, reconstructions of the 2D temperature and H_2O concentration using the MI-DIP have stronger spatial correlation, which agrees with those shown in the phantoms.

Quantitative Analysis

Structural Similarity Index (SSIM) and Root Mean Squared Error (RMSE) were introduced to statistically evaluate the reconstruction results. As shown in Table 5.1, Tikhonov regularization, while providing reasonable results, has the lowest SSIM and highest RMSE, suggesting that the performance of this method is less accurate compared to DIP and MI-DIP. MI-DIP outperforms Tikhonov and DIP with the highest SSIM, improving by 9.9%-13.9% on temperature reconstruction and 39.1% - 40.3% on H_2O concentration reconstruction. It also gives the lowest RMSE, lowering than those using the Tikhonov and DIP by 17.7%-25.9% on temperature reconstruction and 5.8%-9.1% on H_2O concentration reconstruction. These results demonstrate that the MI-DIP contributes to more accurate interpretation of the combustion process. Although the DIP has the similar SSIM compared to the Tikhonov regularization, it shows lower RMSE evidenced by the less artefacts in the reconstructions. However, due to the lack of sufficient prior information, the DIP is not powerful enough to retrieve structural details of the flame.

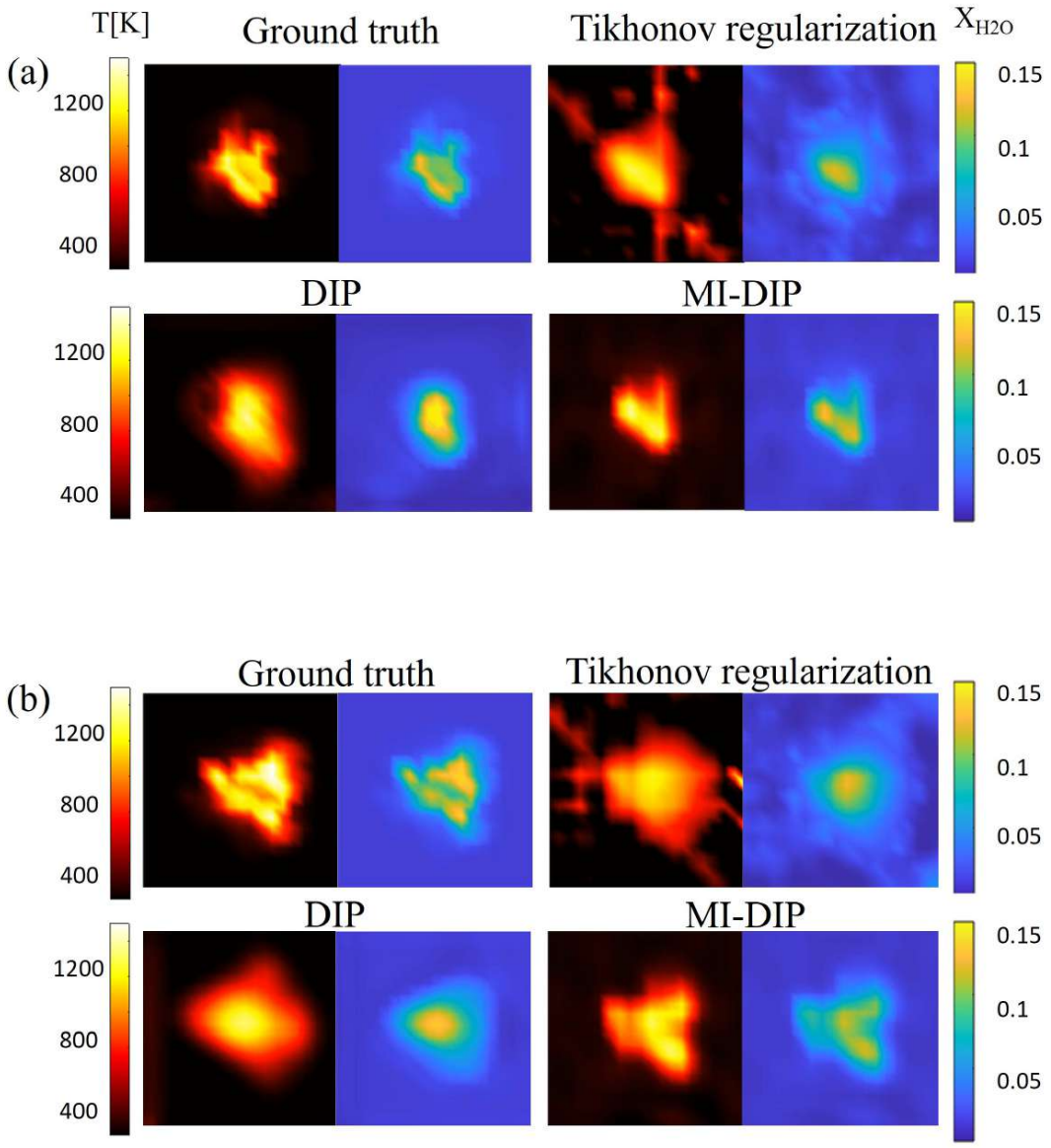

Figure 5.7: Comparison of the proposed MI-DIP to Tikhonov regularization and DIP on two randomly selected frames in the supplementary material, (a) frame 23 and (b) frame 31.

Table 5.1: SSIM and RMSE of reconstructed distributions of temperature and H_2O concentration using Tikhonov regularization, DIP and MI-DIP.

Method	SSIM		RMSE	
	$\mathbf{T}_{\text{rec}}$	$\mathbf{X}_{\text{rec}}$	$\mathbf{T}_{\text{rec}}$	$\mathbf{X}_{\text{rec}}$
Tikhonov	0.753	0.616	151.25	0.0143
DIP	0.781	0.611	136.23	0.0138
MI-DIP	0.858	0.857	112.13	0.013

5.6 Discussions

In this section, we discuss the robustness of the MI-DIP against measurement noise and the regularization parameter λ_{tik}. Then, the ablation study was conducted to evaluate the effects of the SAM and the soft-threshold scheme on the MI-DIP. Finally, we further discuss the potential influence on reconstruction results from the out-of-ROI region.

5.6.1 Robustness

Noise Robustness

To investigate the robustness of the algorithm at different noise levels, Gaussian noise is added to the LAS measurements $\mathbf{A}_{\text{sim},v1}$ and $\mathbf{A}_{\text{sim},v2}$, at SNRs of 25dB, 30dB, 35 dB and 40 dB, respectively. Figure 5.8 illustrates the visual comparison when $\mathbf{A}_{\text{sim},v1}$ and $\mathbf{A}_{\text{sim},v2}$ are contaminated with four different noise levels on two simulated phantoms. When the noise level varies from 25 dB to 30 dB, the reconstructed images are blurred with some artefacts generated in the ambient background. At such noise levels, the MI-DIP can reconstruct the approximate location and general shape of the flame. As SNR increases, the reconstructed images become more accurate. Furthermore, Figure 5.9 (a) and (b) show the variations of mean and standard deviation of SSIM and RMSE for imaging of temperature and H_2O concentration, respectively. The SSIM at 25 dB SNR decreases about 4.5% and 5% for the temperature and H_2O concentration retrieval compared to those at the noise-free condition, respectively. RMSE increases less than 20 K and 0.002 for the temperature and concentration retrieval, respectively. From both visual and statistical analysis, the proposed MI-DIP demonstrates convincing noise robustness and strong resistance to artefacts.

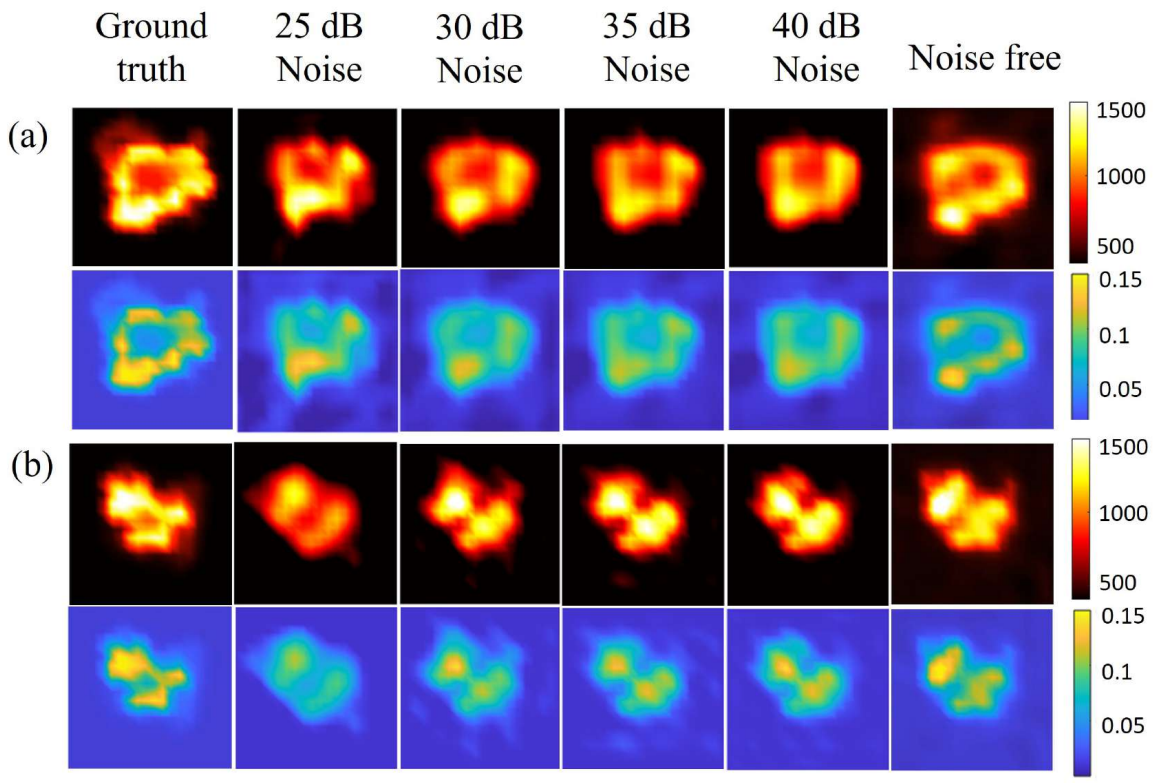

Figure 5.8: Reconstructions of 2D temperature and H_2O concentration on (a) frame 42 and (b) frame 31 using the proposed MI-DIP with measurement SNRs of 25dB, 30dB, 35 dB and 40 dB, respectively.

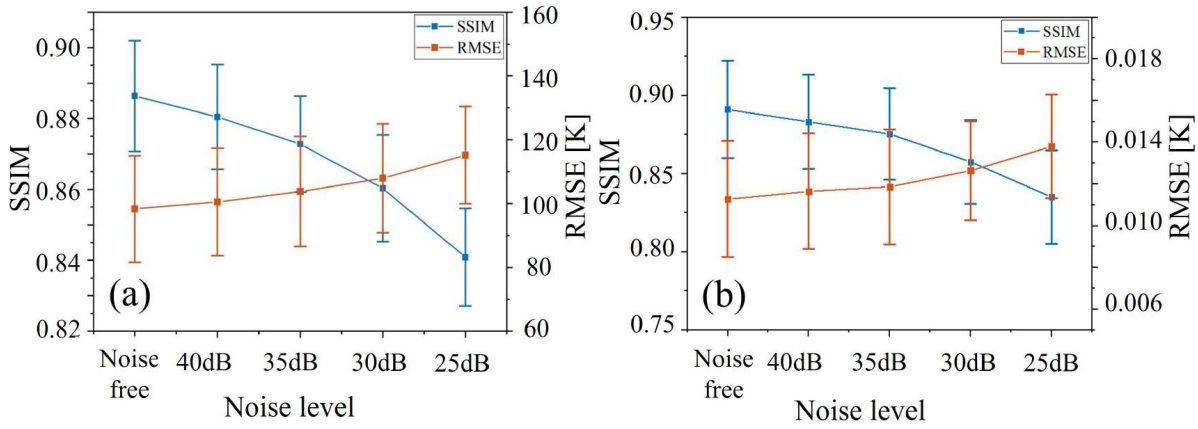

Figure 5.9: Variation of mean and standard deviation on SSIM and RMSE when varying noise levels for the reconstruction of (a) temperature and (b) H_2O concentration.

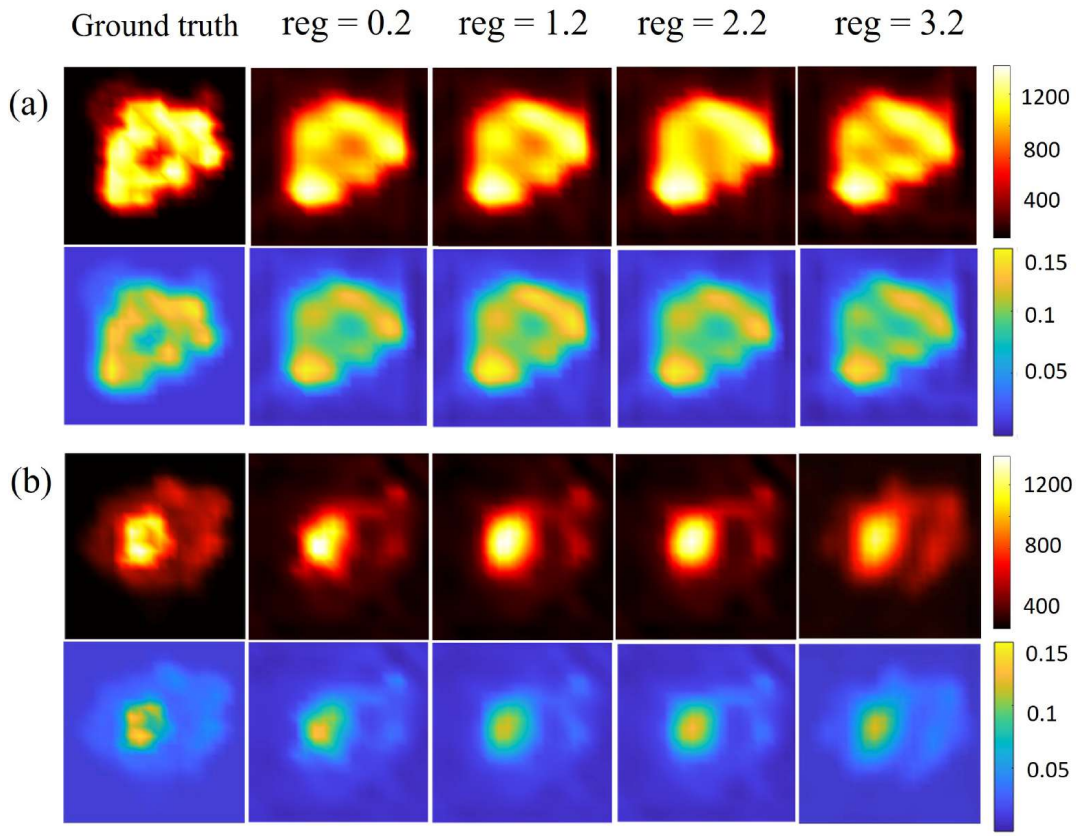

Figure 5.10: Reconstructions of 2D temperature and H_2O concentration on (a) frame 44 and (b) frame 15 using the proposed MI-DIP with different λ_{tik}.

Regularization Parameter λ_{tik}

It can be seen from Eq.(5.4) that the choice of λ_{tik} could influence the reconstruction using the Tikhonov regularization. Therefore, the magnitude of λ_{tik} may affect the performance of MI-DIP as well. In order to test the robustness of the MI-DIP, we further investigate the effect of λ_{tik} by conducting quantitative and qualitative analysis when λ_{tik} varies from 0.2 to 3.2.

Figure 5.10 depicts the reconstructed temperature and H_2O concentration of the simulated phantoms when λ_{tik} equals 0.2, 1.2, 2.2 and 3.2, respectively. From the visual perspective, the reconstructions with the four different λ_{tik} perform similarly, and can characterize the structural details of the phantoms. The λ_{tik}-dependent SSIM and RMSE are shown in Figure 12. Generally, the mean value of SSIMs and RMSEs for both temperature and concentration reconstructions are relatively stable against λ_{tik}, indicating the choice of λ_{tik} has small influence on the performance of the MI-DIP's reconstruction.

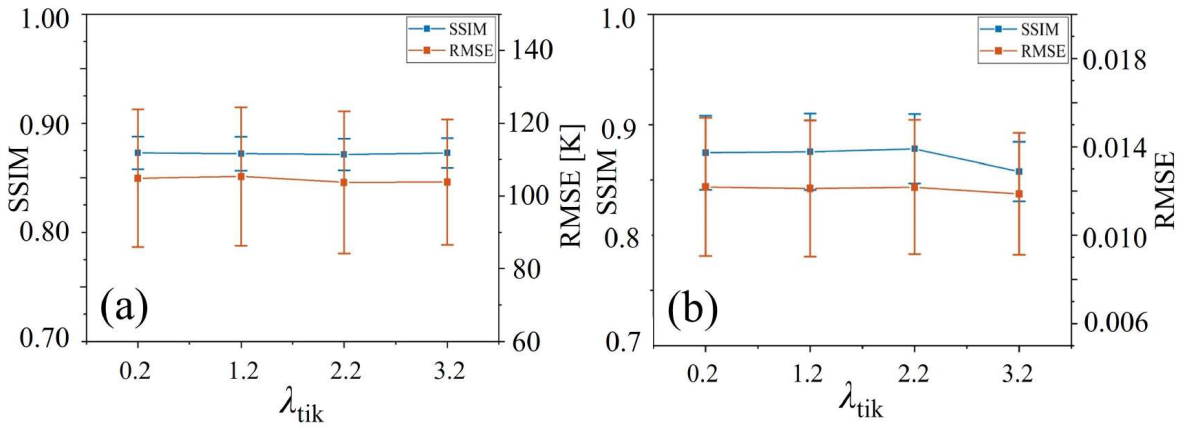

Figure 5.11: Variation of mean and standard deviation on SSIM and RMSE when varying λ_{tik} for the reconstruction of (a) temperature reconstruction and (b) H_2O concentration.

Table 5.2: SSIM and RMSE of reconstructed distributions of temperature and H_2O concentration using the MI-DIP, MI-DIP without soft-threshold scheme and MI-DIP without SAM module

Algorithms	SSIM		RMSE	
	$\mathbf{T}_{rec}$	$\mathbf{X}_{rec}$	$\mathbf{T}_{rec}$	$\mathbf{X}_{rec}$
MI-DIP	0.858	0.857	112.13	0.013
MI-DIP w/o soft-threshold scheme	0.806	0.78	128.42	0.0152
MI-DIP w/o SAM module	0.796	0.825	130.35	0.0136

5.6.2 Ablation Study on soft-threshold scheme and SAM

To further assess the necessity of the soft-threshold scheme and SAM, we delivered two modified models based on the MI-DIP, one keeping the MI-DIP architecture without the soft-threshold scheme, another without SAM modules between the two branches. Table II summarizes the performances of the three models by comparing SSIM and RMSE using the same simulation dataset. Omitting the soft-threshold scheme complicates the model's optimization, as this scheme enables regularizing the optimization pathway for reconstruction by incorporating physical information. It results in worse reconstructions evidenced by the lower SSIM and higher RMSE. Additionally, neglecting the SAM results in a more significant difference between the temperature and H_2O concentration retrievals. It can be observed from the numerical results that eliminating the crosstalk between the two feedforward branches hinders learning of implicit relationship between the two flow parameters during the model training.

Effect of out-of-ROI region

Although the out-of-ROI region is not the focus of the gas properties reconstructions, it can still influence the reconstruction results in several ways: 1) Measurement contamination: when the laser beam passes through regions outside of ROI, the laser intensity will be partially absorbed, where the area has different gas concentrations or temperatures. This can introduce uncertainty and inaccuracy of the reconstruction in the ROI. 2) Artefacts: The out-of-ROI region contribute to the absorption of the laser intensity may cause more artefacts at the edges in the reconstructed images. This is much more severe when there is a sharp transition between the ROI and the surrounding areas, leading to inaccurate and blurred reconstruction results. Therefore, with regard to these effects, we assumed that the temperature and gas concentration would remain stable under ambient conditions within these regions, and subtracted the corresponding absorption from the measurements.

5.7 Conclusion

A novel dataset-free and training-free image reconstruction algorithm MI-DIP is proposed, for the joint reconstruction of temperature and H_2O concentration using LAS tomography. To the best of our knowledge, this is the first dual-path UNN-based algorithm developed for hard-field tomography. To improve the imaging fidelity, the absorption physical model of LAS tomography and naturally true a priori is integrated into the algorithm.

The proposed MI-DIP is assessed by lab-scale experiments. Referring to the TC's measurements, the developed MI-DIP can accurately reconstruct the distributions of temperature and H_2O concentration, and exhibit high sensitivity on imaging dynamic combustion. Besides, a numerical simulation was conducted to statistically evaluate the MI-DIP. It outperforms other given approaches with 17.6%-25.8% lower RMSE and 9.9%-13.9% higher SSIM on temperature reconstruction and 5.8%-9.1% lower RMSE and 39.1%-40.3% higher SSIM on concentration reconstruction. Furthermore, we verified its robustness on various noise levels and regularization parameters.

Based on the research of this chapter, one journal paper has been submitted to IEEE Transactions on Neural Networks and Learning Systems:

- **Y. Fu**, Z. Liu, R. Zhang, J. Xia, X. Liu, and C. Liu, "Model-informed double image prior for flow-field imaging using chemical species tomography," (submitted to *IEEE Transactions on Neural Networks and Learning Systems*).

Chapter 6

Conclusion and Future Work

6.1 Conclusion

Effective diagnosis of reactive flow during the combustion process is important for monitoring the combustion efficiency and the potential emission of harmful gases. The LAS technique has demonstrated its advantages for the non-intrusive, fast-response, and accurate measurement of gas properties. However, the deployment of LAS technology in the industrial environment for rapid diagnosis still faces some challenges. In terms of the LoS-LAS, time-consuming spectral fitting algorithms hinder the timely feedback of the combustion process. For LAS tomography, the limited optical access results in insufficient measurement, thus introducing artefacts and leading to inaccurate reconstructions. To address the aforementioned issues, this thesis puts forward efficient algorithms to accelerate the signal post-processing and advanced methods for improving the reconstruction results for gas imaging. The main content and contributions of this thesis are summarised as follows:

The fundamentals of the LAS techniques are first introduced along with two common LoS-LAS implementations, which enhances the general understanding of the technical background of this thesis. Then the signal post-processing methods for LoS-LAS have been reviewed and discussed. This is followed by the theoretical introduction of LAS tomography with a review of popular image reconstruction algorithms.

Initially, targeting the improvement of the efficiency of signal post-processing algorithms for the LoS-LAS technique, we propose a model-driven spectroscopic network with strong generalizability to monitor the EGT rapidly and accurately. The proposed network relies on data obtained from a well-proven temperature measurement technique, i.e., WMS, with the novelty of introducing the underlying physical absorption model and building a hybrid dataset from simulation and experiment. This hybrid model-driven network enables strong noise resistance of the neural network

against real-world experimental data. The proposed network is assessed by *in situ* measurements of EGT on an aero-GTE (Honeywell, Model: GTCP85-129) mounted in a test cell at the University of Sheffield. In this study, water vapor is selected to be the targeted gas species, and two laser beams with wavenumbers of 7185.6 cm^{-1} and 7444.36 cm^{-1} are deployed for showcasing the absorption features. This model owns a millisecond-level temporal response. Experimental results indicate that the proposed network substantially outperforms the previous neural network methods in terms of accuracy and precision of the measured EGT when the GTE is steadily loaded.

Focusing on LAS tomography, deep learning algorithms have been deployed for effective gas-property retrieval. However, most previous approaches encountered issues when they constructed their training sets by modeling phantoms using simple two-dimensional Gaussian profiles. This limits their ability to reconstruct complex and dynamic temperature fields, often resulting in only static and simplistic temperature imaging. To overcome this limitation, we developed two simulation datasets: one using customized multiple Gaussian profiles to model an annular combustor with ten injectors, and the other utilizing the FDS to simulate dynamic, fire-driven reacting flows. With this enriched training data, we designed a CNN. In our study, a 128-beam tomography system was simulated and arranged into four equiangular projection angles. This novel method was validated through numerical simulations, demonstrating high accuracy and sensitivity in monitoring dynamic flames. The results indicate that this approach enhances the capability to capture and analyze transient temperature fields in real-time, marking a remarkable advancement in the field of thermal imaging and monitoring.

Although FDS can vividly simulate real reactive flow for constructing data-driven deep learning algorithms, data-driven methods often require extensive computational resources, complex dataset construction, and struggle with limited generalization and lack of interpretability. On the other hand, traditional regularization techniques, despite their inability to effectively reduce artifacts, have been successful in incorporating prior information such as smoothness and non-negativity to solve inverse problems. In this study, we propose a novel generator algorithm: a dual-path image prior network combined with laser tomography. This approach is driven by the underlying physical model and regularized by the traditional reconstruction technique, specifically Tikhonov regularization, to simultaneously retrieve images of temperatures and gas concentrations. Our method leverages the strengths of both the DIP approach and

laser tomography. Quantitative and qualitative analysis based on simulation and experimental results demonstrates that the proposed model offers superior performance in temperature and concentration reconstruction. It achieves higher accuracy, better noise robustness, improved spatial resolution, and fewer artifacts compared to traditional regularization methods. Additionally, it showcases better generalization ability and interpretability compared to other deep learning-based algorithms. This promising approach effectively combines the strengths of DIP and laser tomography, offering significant advancements in temperature and concentration imaging.

In conclusion, the algorithms and new methods proposed in this thesis strengthen the performance of LoS-LAS by accelerating the signal post-processing and improving the accuracy of temperature retrieval. In addition, the reliable dataset construction method makes it possible for data-driven temperature reconstruction methods to capture the dynamics of the combustion process, as well as the newly proposed untrained neural network for realizing simultaneous temperature and concentration reconstruction of LAS tomography. Based on the above work, there are further extension works can be done to facilitate the application of LAS techniques in industry.

6.2 Future Work

Although the advancements made in this thesis on gas-property retrieval for combustion diagnosis are significant, several avenues for future research remain open. The potential areas for exploration include:

While Chapter 3 illustrates HMD-WMS, a data-driven method integrated with the physical absorption model, to rapidly reconstruct the averaged temperature along the optical path, it still hasn't realized the real-time temperature retrieval. This limitation arises primarily from the computational complexity and the time required for data processing and training. In future work, we plan to adopt this algorithm into an embedded computing system with an efficient DAQ system and advanced signal preprocessing algorithms. The optimally trained model will be restored in the hardware and will process the signals immediately once the DAQ system acquires new data. This approach is expected to greatly enhance the efficiency and speed of temperature retrieval, enabling real-time monitoring. In addition, the embedded system should be incorporated parallel processing and hardware accelerations such as GPUs and FPGAs. These technologies can significantly reduce the computational cost and enable faster data throughput.

Furthermore, current deep learning algorithms for signal post-processing heavily rely on well-labelled datasets. To retain the advantages of well-developed parallel computation power inherent in deep learning techniques, it is imperative to develop effective unsupervised algorithms that are entirely independent of labelled datasets. The integration of unsupervised deep learning algorithms into signal post-processing frameworks will not only enhance the efficiency and accuracy of temperature and gas concentration retrieval but also expand the applicability of these systems to a wider array of industrial and environmental applications. This shift towards unsupervised learning represents a significant step forward in the development of autonomous, intelligent monitoring and diagnostic systems, capable of operating effectively in diverse and dynamic conditions.

Towards the potential improvement in the field of LAS tomography, addressing the inherent ill-posedness of the problem is crucial. This ill-posedness primarily arises from the requirement for good spatial resolution in mesh-based image reconstructions, leading to a large number of unknown parameters that must be determined. A promising approach to mitigate this issue is the use of meshless expressions, such as Gaussian distributions, to represent the temperature and concentration fields. For instance, employing a Gaussian Mixture Model (GMM) allows these distributions to be described using a set of means and covariances. This significantly reduces the number of required parameters, thereby decreasing the ill-posedness of the reconstruction problem. By utilizing Gaussian distributions, the complex temperature and gas concentration profiles can be efficiently represented with fewer parameters, which simplifies the computational process and enhances the stability of the solutions. This approach not only reduces the computational burden but also improves the accuracy and reliability of the reconstructions. It paves the way for more efficient, accurate, and real-time diagnostic capabilities in various industrial and environmental applications, thereby expanding the practical utility and effectiveness of LAS tomography.

In addition, to further capture the complete combustion behavior, three-dimensional (3D) reconstruction of gas properties can be realized by LAS sensors and available 3D imaging algorithms. This integration allows for a comprehensive spatial analysis of temperature and gas concentration distributions, providing a more detailed and accurate depiction of the combustion process.

Appendix A

Video of the Comparison of Different Methods for Reconstructing Temperature and Gas Species Concentration

This appendix contains a video demonstrating the reconstructions from various methods over 50 frames, as described in Section 5.5.2. The video highlights the performance differences among the methods in terms of reconstructing temperature and gas species concentration, providing a visual comparison to support the analysis and discussions presented in the main text.

The full video is available from:

https://drive.google.com/file/d/1MiWEMdZ4PgT7_eechPSOdG_FlZcQebq_/view?usp=drive_link

The snapshot is exhibited below.

A. Video of the Comparison of Different Methods for Reconstructing Temperature and Gas Spe

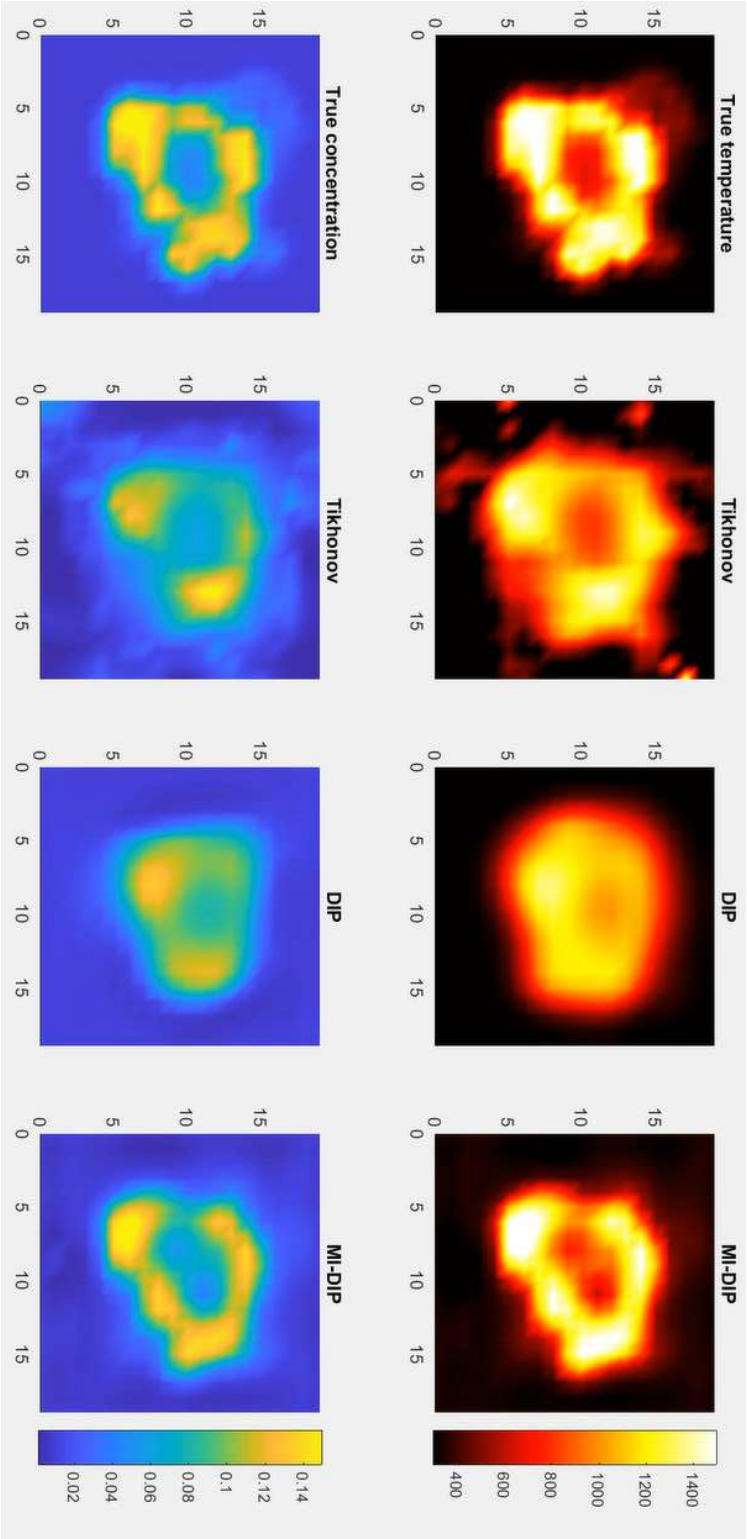

Figure A.1: The snapshot of the video.

Bibliography

[1] K. Kohse-Höinghaus, "Combustion in the future: The importance of chemistry," *Proceedings of the Combustion Institute*, vol. 38, no. 1, pp. 1–56, 2021.

[2] Y. Liu, X. Sun, V. Sethi, D. Nalianda, Y.-G. Li, and L. Wang, "Review of modern low emissions combustion technologies for aero gas turbine engines," *Progress in Aerospace Sciences*, vol. 94, pp. 12–45, 2017.

[3] B. Giechaskiel and M. Clairotte, "Fourier transform infrared (ftir) spectroscopy for measurements of vehicle exhaust emissions: A review," *Applied Sciences*, vol. 11, no. 16, p. 7416, 2021.

[4] A. Rafoth, S. Gabriel, F. Sacher, and H.-J. Brauch, "Analysis of isothiazolinones in environmental waters by gas chromatography–mass spectrometry," *Journal of Chromatography A*, vol. 1164, no. 1-2, pp. 74–81, 2007.

[5] N. Docquier and S. Candel, "Combustion control and sensors: a review," *Progress in energy and combustion science*, vol. 28, no. 2, pp. 107–150, 2002.

[6] E. P. Hassel and S. Linow, "Laser diagnostics for studies of turbulent combustion," *Measurement Science and Technology*, vol. 11, no. 2, p. R37, 2000.

[7] J. Meléndez, A. Foronda, J. Aranda, F. Lopez, and F. L. Del Cerro, "Infrared thermography of solid surfaces in a fire," *Measurement Science and Technology*, vol. 21, no. 10, p. 105504, 2010.

[8] S. Gao, X. Zhang, L. Chen, Y. Cui, J. Jiang, Z. Zhang, P. Yu, and C. Wang, "Radiation temperature measurement methods for engine turbine blades and environment influence," *Infrared Physics & Technology*, vol. 123, p. 104204, 2022.

[9] C. Schulz and V. Sick, "Tracer-lif diagnostics: quantitative measurement of fuel concentration, temperature and fuel/air ratio in practical combustion systems," *Progress in energy and combustion science*, vol. 31, no. 1, pp. 75–121, 2005.

[10] J. Seitzman and R. Hanson, "Planar fluorescence imaging: Basic concepts for scalar and velocity measurements," *Combustings flow diagnostics*, pp. 137–157, 1992.

[11] R. J. Hall and A. C. Eckbreth, “Combustion diagnosis by coherent anti-stokes raman spectroscopy (cars),” *Optical Engineering*, vol. 20, no. 4, pp. 494–500, 1981.

[12] S. Roy, J. R. Gord, and A. K. Patnaik, “Recent advances in coherent anti-stokes raman scattering spectroscopy: Fundamental developments and applications in reacting flows,” *Progress in Energy and Combustion Science*, vol. 36, no. 2, pp. 280–306, 2010.

[13] G. Magnotti, D. Geyer, and R. Barlow, “Interference free spontaneous raman spectroscopy for measurements in rich hydrocarbon flames,” *Proceedings of the Combustion Institute*, vol. 35, no. 3, pp. 3765–3772, 2015.

[14] C. S. Goldenstein, R. M. Spearrin, J. B. Jeffries, and R. K. Hanson, “Infrared laser-absorption sensing for combustion gases,” *Progress in Energy and Combustion Science*, vol. 60, pp. 132–176, 2017.

[15] M. G. Allen, “Diode laser absorption sensors for gas-dynamic and combustion flows,” *Measurement Science and technology*, vol. 9, no. 4, p. 545, 1998.

[16] C. Liu and L. Xu, “Laser absorption spectroscopy for combustion diagnosis in reactive flows: A review,” *Applied Spectroscopy Reviews*, vol. 54, no. 1, pp. 1–44, 2019.

[17] A. Upadhyay, M. Lengden, G. Enemali, G. Stewart, W. Johnstone, D. Wilson, G. Humphries, T. Benoy, J. Black, A. Chighine, *et al.*, “Tomographic imaging of carbon dioxide in the exhaust plume of large commercial aero-engines,” *Applied optics*, vol. 61, no. 28, pp. 8540–8552, 2022.

[18] Y. Fu, R. Zhang, J. Xia, A. Gough, S. Clark, A. Upadhyay, G. Enemali, I. Armstrong, I. Ahmed, M. Pourkashanian, *et al.*, “Hybrid model-driven spectroscopic network for rapid retrieval of turbine exhaust temperature,” *IEEE Transactions on Instrumentation and Measurement*, 2023.

[19] R. Zhang, J. Xia, I. Ahmed, A. Gough, I. Armstrong, A. Upadhyay, Y. Fu, G. Enemali, M. Lengden, W. Johnstone, *et al.*, “A fast sensor for non-intrusive measurement of concentration and temperature in turbine exhaust,” *Sensors and Actuators B: Chemical*, vol. 396, p. 134500, 2023.

[20] C. Liu, L. Xu, J. Chen, Z. Cao, Y. Lin, and W. Cai, “Development of a fan-beam tdlas-based tomographic sensor for rapid imaging of temperature and gas concentration,” *Optics express*, vol. 23, no. 17, pp. 22494–22511, 2015.

[21] H. Xia, R. Kan, Z. Xu, Y. He, J. Liu, B. Chen, C. Yang, L. Yao, M. Wei, and G. Zhang, "Two-step tomographic reconstructions of temperature and species concentration in a flame based on laser absorption measurements with a rotation platform," *Optics and Lasers in Engineering*, vol. 90, pp. 10–18, 2017.

[22] K. Daun, "Infrared species limited data tomography through tikhonov reconstruction," *Journal of Quantitative Spectroscopy and Radiative Transfer*, vol. 111, no. 1, pp. 105–115, 2010.

[23] N. Polydorides, A. Tsekenis, E. Fisher, A. Chighine, H. McCann, L. Dimiccoli, P. Wright, M. Lengden, T. Benoy, D. Wilson, *et al.*, "Constrained models for optical absorption tomography," *Applied optics*, vol. 57, no. 7, pp. B1–B9, 2018.

[24] G. Bebis and M. Georgiopoulos, "Feed-forward neural networks," *Ieee Potentials*, vol. 13, no. 4, pp. 27–31, 1994.

[25] J. Gu, Z. Wang, J. Kuen, L. Ma, A. Shahroudy, B. Shuai, T. Liu, X. Wang, G. Wang, J. Cai, *et al.*, "Recent advances in convolutional neural networks," *Pattern recognition*, vol. 77, pp. 354–377, 2018.

[26] L. R. Medsker, L. Jain, *et al.*, "Recurrent neural networks," *Design and Applications*, vol. 5, no. 64-67, p. 2, 2001.

[27] R. Hanson, P. Kuntz, and C. Kruger, "High-resolution spectroscopy of combustion gases using a tunable ir diode laser," *Applied Optics*, vol. 16, no. 8, pp. 2045–2048, 1977.

[28] M. Arroyo and R. Hanson, "Absorption measurements of water-vapor concentration, temperature, and line-shape parameters using a tunable ingaasp diode laser," *Applied optics*, vol. 32, no. 30, pp. 6104–6116, 1993.

[29] E. R. Furlong, D. S. Baer, and R. K. Hanson, "Real-time adaptive combustion control using diode-laser absorption sensors," in *Symposium (International) on Combustion*, vol. 27, pp. 103–111, Elsevier, 1998.

[30] V. Nagali and R. K. Hanson, "Design of a diode-laser sensor to monitor water vapor in high-pressure combustion gases," *Applied optics*, vol. 36, no. 36, pp. 9518–9527, 1997.

[31] X. Zhou, "Diode laser absorption sensors for combustion control," 2005.

[32] W. Cai and C. F. Kaminski, "Tomographic absorption spectroscopy for the study of gas dynamics and reactive flows," *Progress in energy and combustion science*, vol. 59, pp. 1–31, 2017.

[33] P. Sindhu, *Fundamentals of Molecular Spectroscopy.* New Age International, 2006.

[34] R. R. Gamache, R. Lynch, and S. P. Neshyba, "New developments in the theory of pressure-broadening and pressure-shifting of spectral lines of h2o: the complex robert-bonamy formalism," *Journal of Quantitative Spectroscopy and Radiative Transfer*, vol. 59, no. 3-5, pp. 319–335, 1998.

[35] R. Brun, *Introduction to reactive gas dynamics*. Oxford University Press, 2009.

[36] R. K. Hanson, R. M. Spearrin, and C. S. Goldenstein, *Spectroscopy and optical diagnostics for gases*, vol. 1. Springer, 2016.

[37] A. C. Mitchell and M. W. Zemansky, "Resonance radiation and excited atoms," *Resonance Radiation and Excited Atoms*, 2009.

[38] J. J. Olivero and R. Longbothum, "Empirical fits to the voigt line width: A brief review," *Journal of Quantitative Spectroscopy and Radiative Transfer*, vol. 17, no. 2, pp. 233–236, 1977.

[39] F. Mayinger, *Optical measurements: techniques and applications*. Springer Science & Business Media, 2013.

[40] T. Yoshino, K. Kurosawa, K. Itoh, and T. Ose, "Fiber-optic fabry-perot interferometer and its sensor applications," *IEEE Transactions on Microwave Theory and Techniques*, vol. 30, no. 10, pp. 1612–1621, 1982.

[41] K. Sun, X. Chao, R. Sur, C. Goldenstein, J. Jeffries, and R. Hanson, "Analysis of calibration-free wavelength-scanned wavelength modulation spectroscopy for practical gas sensing using tunable diode lasers," *Measurement Science and Technology*, vol. 24, no. 12, p. 125203, 2013.

[42] H. Li, G. B. Rieker, X. Liu, J. B. Jeffries, and R. K. Hanson, "Extension of wavelength-modulation spectroscopy to large modulation depth for diode laser absorption measurements in high-pressure gases," *Applied optics*, vol. 45, no. 5, pp. 1052–1061, 2006.

[43] G. B. Rieker, J. B. Jeffries, and R. K. Hanson, "Calibration-free wavelength-modulation spectroscopy for measurements of gas temperature and concentration in harsh environments," *Applied optics*, vol. 48, no. 29, pp. 5546–5560, 2009.

[44] C. S. Goldenstein, C. A. Almodóvar, J. B. Jeffries, R. K. Hanson, and C. M. Brophy, "High-bandwidth scanned-wavelength-modulation spectroscopy sensors for temperature and h2o in a rotating detonation engine," *Measurement Science and Technology*, vol. 25, no. 10, p. 105104, 2014.

[45] W. Wei, W. Y. Peng, Y. Wang, J. Shao, C. L. Strand, and R. K. Hanson, "Two-color frequency-multiplexed ims technique for gas thermometry at elevated pressures," *Applied Physics B*, vol. 126, no. 3, p. 51, 2020.

[46] I. E. Gordon, L. S. Rothman, R. Hargreaves, R. Hashemi, E. V. Karlovets, F. Skinner, E. K. Conway, C. Hill, R. V. Kochanov, Y. Tan, *et al.*, "The hitran2020 molecular spectroscopic database," *Journal of quantitative spectroscopy and radiative transfer*, vol. 277, p. 107949, 2022.

[47] C. S. Goldenstein, I. A. Schultz, J. B. Jeffries, and R. K. Hanson, "Two-color absorption spectroscopy strategy for measuring the column density and path average temperature of the absorbing species in nonuniform gases," *Applied optics*, vol. 52, no. 33, pp. 7950–7962, 2013.

[48] C. S. Goldenstein, C. L. Strand, I. A. Schultz, K. Sun, J. B. Jeffries, and R. K. Hanson, "Fitting of calibration-free scanned-wavelength-modulation spectroscopy spectra for determination of gas properties and absorption lineshapes," *Applied optics*, vol. 53, no. 3, pp. 356–367, 2014.

[49] Z. Qu, R. Ghorbani, D. Valiev, and F. M. Schmidt, "Calibration-free scanned wavelength modulation spectroscopy–application to h2o and temperature sensing in flames," *Optics express*, vol. 23, no. 12, pp. 16492–16499, 2015.

[50] R. Xu, L. Tian, J. Xia, F. Zhao, K. Guo, Z. Liang, and S. Zhang, "Leveraging deep learning for optimal methane gas detection: Residual network filter assisted direct absorption spectroscopy," *Sensors and Actuators A: Physical*, vol. 369, p. 115195, 2024.

[51] J. Sun, L. Tian, J. Chang, A. A. Kolomenskii, H. A. Schuessler, J. Xia, C. Feng, and S. Zhang, "Adaptively optimized gas analysis model with deep learning for near-infrared methane sensors," *Analytical Chemistry*, vol. 94, no. 4, pp. 2321–2332, 2022.

[52] L. Tian, J. Sun, J. Chang, J. Xia, Z. Zhang, A. A. Kolomenskii, H. A. Schuessler, and S. Zhang, "Retrieval of gas concentrations in optical spectroscopy with deep learning," *Measurement*, vol. 182, p. 109739, 2021.

[53] J. Sun, J. Chang, Y. Wei, Z. Zhang, S. Lin, F. Wang, and Q. Zhang, "Dual gas sensor with innovative signal analysis based on neural network," *Sensors and Actuators B: Chemical*, vol. 373, p. 132697, 2022.

[54] G. T. Herman, "Image reconstruction from projections," *The fundamentals of computerized tomography*, vol. 316, 1980.

[55] K. J. Daun, S. J. Grauer, and P. J. Hadwin, "Chemical species tomography of turbulent flows: Discrete ill-posed and rank deficient problems and the use of prior information," *Journal of Quantitative Spectroscopy and Radiative Transfer*, vol. 172, pp. 58–74, 2016.

[56] P. C. Hansen, *Rank-deficient and discrete ill-posed problems: numerical aspects of linear inversion*. SIAM, 1998.

[57] S. J. Grauer, P. J. Hadwin, and K. J. Daun, "Improving chemical species tomography of turbulent flows using covariance estimation," *Applied optics*, vol. 56, no. 13, pp. 3900–3912, 2017.

[58] S. J. Grauer, P. J. Hadwin, and K. J. Daun, "Bayesian approach to the design of chemical species tomography experiments," *Applied optics*, vol. 55, no. 21, pp. 5772–5782, 2016.

[59] M.-G. Jeon, Y. Deguchi, T. Kamimoto, D.-H. Doh, and G.-R. Cho, "Performances of new reconstruction algorithms for ct-tdlas (computer tomography-tunable diode laser absorption spectroscopy)," *Applied Thermal Engineering*, vol. 115, pp. 1148–1160, 2017.

[60] L. Landweber, "An iteration formula for fredholm integral equations of the first kind," *American journal of mathematics*, vol. 73, no. 3, pp. 615–624, 1951.

[61] L. Xu, C. Liu, W. Jing, Z. Cao, X. Xue, and Y. Lin, "Tunable diode laser absorption spectroscopy-based tomography system for on-line monitoring of two-dimensional distributions of temperature and h2o mole fraction," *Review of Scientific Instruments*, vol. 87, no. 1, 2016.

[62] J. Huang, H. Liu, J. Dai, and W. Cai, "Reconstruction for limited-data nonlinear tomographic absorption spectroscopy via deep learning," *Journal of Quantitative Spectroscopy and Radiative Transfer*, vol. 218, pp. 187–193, 2018.

[63] Y. Jiang, J. Si, R. Zhang, G. Enemali, B. Zhou, H. McCann, and C. Liu, "Cstnet: A dual-branch convolutional neural network for imaging of reactive flows using chemical species tomography," *IEEE Transactions on Neural Networks and Learning Systems*, 2022.

[64] Z. Wang, N. Zhu, W. Wang, and X. Chao, "Y-net: a dual-branch deep learning network for nonlinear absorption tomography with wavelength modulation spectroscopy," *Optics Express*, vol. 30, no. 2, pp. 2156–2172, 2022.

[65] J. Si, A. Wang, and Y. Cheng, "Temperature imaging network based on swin transformer for tdlas tomography," in *Fourteenth International Conference on Digital Image Processing (ICDIP 2022)*, vol. 12342, pp. 796–803, SPIE, 2022.

[66] J. Si, G. Fu, X. Liu, Y. Cheng, R. Zhang, J. Xia, Y. Fu, G. Enemali, and C. Liu, "A spatially progressive neural network for locally/globally prioritized tdlas tomography," *IEEE Transactions on Industrial Informatics*, 2023.

[67] J. P. Molnar and S. J. Grauer, "Flow field tomography with uncertainty quantification using a bayesian physics-informed neural network," *Measurement Science and Technology*, vol. 33, no. 6, p. 065305, 2022.

[68] S. Patankar, *Numerical heat transfer and fluid flow*. CRC press, 2018.

[69] A. J. Volponi, "Gas turbine engine health management: past, present, and future trends," *Journal of engineering for gas turbines and power*, vol. 136, no. 5, p. 051201, 2014.

[70] F. J. Dutz, S. Boje, U. Orth, A. W. Koch, and J. Roths, "High-temperature profile monitoring in gas turbine exhaust-gas diffusors with six-point fiber-optic sensor array," *International Journal of Turbomachinery, Propulsion and Power*, vol. 5, no. 4, p. 25, 2020.

[71] P. Wright, K. B. Ozanyan, S. J. Carey, and H. McCann, "Design of high-performance photodiode receivers for optical tomography," *IEEE sensors journal*, vol. 5, no. 2, pp. 281–288, 2005.

[72] G. Enemali, R. Zhang, H. McCann, and C. Liu, "Cost-effective quasi-parallel sensing instrumentation for industrial chemical species tomography," *IEEE Transactions on Industrial Electronics*, vol. 69, no. 2, pp. 2107–2116, 2021.

[73] S. J. Cassady, W. Y. Peng, C. L. Strand, D. F. Dausen, J. R. Codoni, C. M. Brophy, and R. K. Hanson, "Time-resolved, single-ended laser absorption thermometry and h2o, co2, and co speciation in a h2/c2h4-fueled rotating detonation engine," *Proceedings of the Combustion Institute*, vol. 38, no. 1, pp. 1719–1727, 2021.

[74] G. C. Mathews, M. G. Blaisdell, A. I. Lemcherfi, C. D. Slabaugh, and C. S. Goldenstein, "High-bandwidth absorption-spectroscopy measurements of temperature, pressure, co, and h 2 o in the annulus of a rotating detonation rocket engine," *Applied Physics B*, vol. 127, no. 12, p. 165, 2021.

[75] F. Almeida and G. Xexéo, "Word embeddings: A survey," *arXiv preprint arXiv:1901.09069*, 2019.

[76] A. Vaswani, N. Shazeer, N. Parmar, J. Uszkoreit, L. Jones, A. N. Gomez, Ł. Kaiser, and I. Polosukhin, "Attention is all you need," *Advances in neural information processing systems*, vol. 30, 2017.

[77] K. He, X. Zhang, S. Ren, and J. Sun, "Deep residual learning for image recognition," in *Proceedings of the IEEE conference on computer vision and pattern recognition*, pp. 770–778, 2016.

[78] A. Ehn, J. Zhu, X. Li, and J. Kiefer, "Advanced laser-based techniques for gas-phase diagnostics in combustion and aerospace engineering," *Applied spectroscopy*, vol. 71, no. 3, pp. 341–366, 2017.

[79] G. Li, E. Dong, and W.-h. Ji, "A near-infrared trace co2 detection system based on an 1,580 nm tunable diode laser using a cascaded integrator comb (cic) filter-assisted wavelength modulation technique and a digital lock-in amplifier," *Frontiers in Physics*, vol. 7, p. 199, 2019.

[80] J. Xia, G. Enemali, R. Zhang, Y. Fu, H. McCann, B. Zhou, and C. Liu, "Fpga-accelerated distributed sensing system for real-time industrial laser absorption spectroscopy tomography at kilo-hertz," *IEEE Transactions on Industrial Informatics*, 2023.

[81] D. P. Kingma and J. Ba, "Adam: A method for stochastic optimization," *arXiv preprint arXiv:1412.6980*, 2014.

[82] C. Liu, Z. Cao, Y. Lin, L. Xu, and H. McCann, "Online cross-sectional monitoring of a swirling flame using tdlas tomography," *IEEE Transactions on Instrumentation and Measurement*, vol. 67, no. 6, pp. 1338–1348, 2018.

[83] F. Wang, Q. Wu, Q. Huang, H. Zhang, J. Yan, and K. Cen, "Simultaneous measurement of 2-dimensional h2o concentration and temperature distribution in premixed methane/air flame using tdlas-based tomography technology," *Optics Communications*, vol. 346, pp. 53–63, 2015.

[84] Q. Qu, Z. Cao, L. Xu, C. Liu, L. Chang, and H. McCann, "Reconstruction of two-dimensional velocity distribution in scramjet by laser absorption spectroscopy tomography," *Applied optics*, vol. 58, no. 1, pp. 205–212, 2019.

[85] Y. Bao, R. Zhang, G. Enemali, Z. Cao, B. Zhou, H. McCann, and C. Liu, "Relative entropy regularized tdlas tomography for robust temperature imaging," *IEEE Transactions on Instrumentation and Measurement*, vol. 70, pp. 1–9, 2020.

[86] J. Dai, T. Yu, L. Xu, and W. Cai, "On the regularization for nonlinear tomographic absorption spectroscopy," *Journal of Quantitative Spectroscopy and Radiative Transfer*, vol. 206, pp. 233–241, 2018.

[87] C. Wei, K. K. Schwarm, D. I. Pineda, and R. M. Spearrin, "Physics-trained neural network for sparse-view volumetric laser absorption imaging of species and temperature in reacting flows," *Optics Express*, vol. 29, no. 14, pp. 22553–22566, 2021.

[88] C. Wei, K. K. Schwarm, D. I. Pineda, and R. M. Spearrin, "Deep neural network inversion for 3d laser absorption imaging of methane in reacting flows," *Optics letters*, vol. 45, no. 8, pp. 2447–2450, 2020.

[89] J. Huang, H. Liu, and W. Cai, "Online in situ prediction of 3-d flame evolution from its history 2-d projections via deep learning," *Journal of Fluid Mechanics*, vol. 875, p. R2, 2019.

[90] N. Gourdain, L. Gicquel, G. Staffelbach, O. Vermorel, F. Duchaine, J. Boussuge, and T. Poinsot, "High performance parallel computing of flows in complex geometries: Ii. applications," *Computational Science & Discovery*, vol. 2, no. 1, p. 015004, 2009.

[91] C. Liu, L. Xu, Z. Cao, and H. McCann, "Reconstruction of axisymmetric temperature and gas concentration distributions by combining fan-beam tdlas with onion-peeling deconvolution," *IEEE Transactions on Instrumentation and Measurement*, vol. 63, no. 12, pp. 3067–3075, 2014.

[92] K. B. McGrattan, H. R. Baum, R. G. Rehm, A. Hamins, G. P. Forney, J. Floyd, S. Hostikka, and K. Prasad, *Fire dynamics simulator–Technical reference guide*. National Institute of Standards and Technology, Building and Fire Research, 2000.

[93] C. Wei, K. K. Schwarm, D. I. Pineda, and R. M. Spearrin, "Volumetric laser absorption imaging of temperature, co and co2 in laminar flames using 3d masked tikhonov regularization," *Combustion and Flame*, vol. 224, pp. 239–247, 2021.

[94] X. Zhang, E. Y. Lam, E. X. Wu, and K. K. Wong, "Application of tikhonov regularization to super-resolution reconstruction of brain mri images," in *Medical Imaging and Informatics: 2nd International Conference, MIMI 2007, Beijing, China, August 14-16, 2007 Revised Selected Papers*, pp. 51–56, Springer, 2008.

[95] D. Ulyanov, A. Vedaldi, and V. Lempitsky, "Deep image prior," in *Proceedings of the IEEE conference on computer vision and pattern recognition*, pp. 9446–9454, 2018.

[96] T. Takagi, S. Ishizaki, and S.-i. Maeda, "Jpeg information regularized deep image prior for denoising," in *2023 IEEE International Conference on Image Processing (ICIP)*, pp. 380–384, IEEE, 2023.

[97] L. Zhuang and M. K. Ng, "Fasthymix: Fast and parameter-free hyperspectral image mixed noise removal," *IEEE Transactions on Neural Networks and Learning Systems*, vol. 34, no. 8, pp. 4702–4716, 2021.

[98] K. Gong, C. Catana, J. Qi, and Q. Li, "Pet image reconstruction using deep image prior," *IEEE transactions on medical imaging*, vol. 38, no. 7, pp. 1655–1665, 2018.

[99] D. Kinga, J. B. Adam, *et al.*, "A method for stochastic optimization," in *International conference on learning representations (ICLR)*, vol. 5, p. 6, San Diego, California, 2015.

[100] D. Huo, A. Masoumzadeh, R. Kushol, and Y.-H. Yang, "Blind image deconvolution using variational deep image prior," *IEEE Transactions on Pattern Analysis and Machine Intelligence*, vol. 45, no. 10, pp. 11472–11483, 2023.

[101] O. Ronneberger, P. Fischer, and T. Brox, "U-net: Convolutional networks for biomedical image segmentation," in *Medical image computing and computer-assisted intervention–MICCAI 2015: 18th international conference, Munich, Germany, October 5-9, 2015, proceedings, part III 18*, pp. 234–241, Springer, 2015.

[102] O. Oktay, J. Schlemper, L. L. Folgoc, M. Lee, M. Heinrich, K. Misawa, K. Mori, S. McDonagh, N. Y. Hammerla, B. Kainz, *et al.*, "Attention u-net: Learning where to look for the pancreas," *arXiv preprint arXiv:1804.03999*, 2018.

[103] A. El-Baz, X. Jiang, and J. S. Suri, "Biomedical image segmentation: advances and trends," 2016.